University of Arkansas, Fayetteville

ScholarWorks@UARK

Graduate Theses and Dissertations

8-2014

Nanofabrication of Metallic Nanostructures and Integration with Light Detection Devices

Liang Huang
University of Arkansas, Fayetteville

Follow this and additional works at: https://scholarworks.uark.edu/etd

Part of the Nanoscience and Nanotechnology Commons, and the Nanotechnology Fabrication Commons

Citation

Huang, L. (2014). Nanofabrication of Metallic Nanostructures and Integration with Light Detection Devices. *Graduate Theses and Dissertations* Retrieved from https://scholarworks.uark.edu/etd/2247

This Dissertation is brought to you for free and open access by ScholarWorks@UARK. It has been accepted for inclusion in Graduate Theses and Dissertations by an authorized administrator of ScholarWorks@UARK. For more information, please contact scholar@uark.edu.

Nanofabrication of Metallic Nanostructures and Integration with Light Detection Devices

Nanofabrication of Metallic Nanostructures and Integration with Light Detection Devices

A dissertation submitted in partial fulfillment
of the requirements for the degree of
Doctor of Philosophy in Microelectronics-Photonics

By

Liang Huang
Nanjing University of Aeronautics and Astronautics
Bachelor of Engineering in Mechanical Engineering and Automation, 2004
Nanjing University of Aeronautics and Astronautics
Master of Engineering in Mechanical Manufacturing and Automation, 2008

August 2014
University of Arkansas

This dissertation is approved for recommendation to the Graduate Council.

Dr. Shui-Qing Yu
Dissertation Director

Dr. Simon Ang
Committee Member

Dr. Hameed Naseem
Committee Member

Prof. Kenneth Vickers
Committee Member

Dr. Gregory Salamo
Ex-Officio Member

The following signatories attest that all software used in this dissertation was legally licensed for use by Liang Huang for research purposes and publication.

______________________________ ______________________________

Mr. Liang Huang, Student Dr. Shui-Qing Yu, Dissertation Director

This dissertation was submitted to http://www.turnitin.com for plagiarism review by the TurnItIn company's software. The signatories have examined the report on this dissertation that was returned by TurnItIn and attest that, in their opinion, the items highlighted by the software are incidental to common usage and are not plagiarized material.

______________________________ ______________________________

Prof. Ken Vickers, Program Director Dr. Shui-Qing Yu, Dissertation Director

Abstract

Metallic nanostructures have been investigated with various applications especially for integration with light detection devices. The incident light can be manipulated by those nanostructures to enhance light absorption therefor improve device performance. However, previous studies focused on optical design. The electrical properties of these integrated light detection devices have not been fully considered. The photon generated carriers transport and collection are critical for light detection devices as well. An optimized device platform considering from both the optical and electrical aspects to fully utilize these nanostructures is highly desired for future light detection devices.

This dissertation targeted on three objectives, beginning with the fabrication process development of various nanostructures on different substrates. High quality nanostructures were achieved with minimum 20nm gap and 45nm line width. The second objective was developing the metallic fishnet nanostructures integrated Schottky contact a-Si solar cell to improve both light absorption and photon generated carrier collection. The fishnet was designed as the light trapping structure and 2D connected top contact to collect carriers. The third objective was developing metallic nanostructures integrated GeSn photodetectors. The H shape nano antennas were integrated on GeSn photodetectors. Multiple resonant absorption peaks at infrared range were observed using spectroscopic ellipsometry. However, there was no obvious photoresponse value improvement of developed solar cells and H shape antennas integrated GeSn photodetectors. For further investigation, interdigitated electrodes integrated GeSn photodetectors were designed. With less carrier transit time, the responsivity value of the integrated $Ge_{0.991}Sn_{0.009}$ photodetector was 72 μA/W at 1.55 μm at room temperature which was 6 times higher comparing to device without integration. Meanwhile, with the increased carrier life

time by decreasing temperature, the responsivity value of integrated $Ge_{0.93}Sn_{0.07}$ detectors at 1.55 μm at 100K was 8.5mA/W which was 200 times higher than the value at 300K. These results suggest relative large surface recombination rate was the dominant loss mechanism in metallic nanostructures integrated light detection devices, as the ratio of carrier life time and transit time determines the gain of photodetector. The light detection devices integrated with metallic nanostructures can be developed to maximize device performance with light trapping effect and carrier collection efficiency.

Acknowledgements

I would like to thank my Ph.D advisor Prof. Shui-Qing (Fisher) Yu, for giving me this great opportunity to work on this project and his invaluable guidance for over five years. Without his endless support and encouragement, I would never get chance to work on this topic. I really appreciate his understanding, patience, knowledgeable, and professional attitudes for all the problems and issues I had in my research. My whole career will benefit a lot from the professional trainings I received from his group. I truly respect him as a great Ph.D advisor and rigorous researcher.

I am thankful to my committee members for their constant support and encouragement over the years. I would like to thank Prof. Ken Vickers for his encouragement and support throughout the Microelectronics-Photonics program; Prof. Hameed Naseem for sharing his expertise on semiconductor photovoltaic materials and devices at each group meeting; Prof. Greg Salamo for his valuable thoughts and serious attitude as a scientist; Prof. Simon Ang for sharing his knowledge on semiconductor device fabrication and packaging. It is my great honor to get chance work with Prof. Vasundara Varadan, whose passion and energy for this project never dwindled.

The work presented here was made possible because of numerous collaborations and helps. I have enjoyed the interaction with researchers who are experts in their fields. These interactions have played a crucial role in making my doctoral research work as the enjoyable experience. I would like to thank Mr. Errol Porter and Mr. Mike Steger for their kindly supports at High Density Electronics Center (HiDEC) cleanroom; Dr. Mourad Benamara for sharing his expertise on SEM and FIB; Mr. Yusuke Hirono for his expertise on AFM measurement.

I want to thank my colleagues at Applied Nano and Bio Photonics Group: I am very grateful to Ben Conley for his generous help in GeSn photodetectors characterization. Thanks to Dr. Wei Du for the help on device characterization. Thanks to Dr. Husam Abu-Safe for the help when I started my Ph.D work. Thanks to Thach Pham for working with me in clean room as a buddy system. Thanks to Seyed Amir Ghetmiri for sharing his knowledge on ellipsometry measurement. Thank you to all my friends and colleagues at University of Arkansas for having been supporting me all the time.

I would like to thank my wife Chunyan Wang for all her support and understanding during my Ph.D study. Whenever and wherever I was upset and frustrated, I can always get support from her helping me move forward. I would like to thank my parents for their endless love and support. Thank you for all the things you have done to make me grow up. Special thanks to my lovely daughter Claire, without whom I might go further. But I cannot image my life without her.

This program was financially supported by National Science Foundation under contract EPS-1003970, by Arkansas Biological Institute, and by Arkansas NASA EPSCoR RID. Any opinions, findings, and conclusions or recommendations expressed in this material are those of the author and do not necessarily reflect the views of the National Science Foundation. The equipment used for fabrication work was through the use of the High Density Electronics Center and Nanofabrication Lab and the Institute for Nanoscience and Engineering at the University of Arkansas, Fayetteville campus.

Dedication

This work is dedicated to my wife Chunyan, my daughter Claire and my parents Guojun and Xiuzhen for their endless love, support, patience and encouragement.

Table of Contents

Chapter 1: Introduction 1

1.1 Metallic Nanostructures Integrated Light Detection Devices 3

1.2 Overview of This Dissertation 6

Chapter 2 Fabrication and Process Development of Nanostructures Using EBL and FIB 8

2.1 Introduction 8

2.2 Electron Beam Lithography 9

2.3 Focused Ion Beam 21

2.4 Metallic Nanostructures Fabrication on c-Si and ITO Substrates 24

2.5 Metallic Nanostructures Fabrication on Glass Substrates 41

2.6 Nanostructures Patterning of c-Si by EBL and FIB 45

2.7 Process Integration Platform 54

Chapter 3: Fishnet Integrated Schottky Contact a-Si Solar Cell 58

3.1 Introduction 58

3.2 Theoretical Analysis 59

3.3 Device Fabrication 62

3.4 Results and Discussion 66

Chapter 4: Metallic Nanostructures Integrated GeSn Photodetectors 73

4.1 Introduction 73

4.2 Optical Characterization of metallic nanostructures 82

4.3 Device Fabrication ... 96

4.4 Device Measurement Setup ... 100

4.5 Results and Discussion ... 101

Chapter 5: Further Investigation ... 104

5.1 Introduction ... 104

5.2 Device Fabrication Results ... 104

5.3 Characterization Results and Discussions ... 105

Chapter 6: Conclusions and Future Work ... 115

References ... 118

Appendix A: Description of Research for Popular Publication ... 127

Appendix B: Executive Summary of Newly Created Intellectual Property ... 128

Appendix C: Potential Patent and Commercialization Aspects of listed Intellectual Property Items ... 129

C.1 Patentability of Intellectual Property ... 129

C.2 Commercialization prospects ... 129

C.3 Possible Prior Disclosure of IP ... 130

Appendix D: Broader Impacts of Research ... 131

Appendix E: Microsoft Project for Ph.D MicroEP Degree Plan ... 132

Appendix F: Identification of All Software Used in Research and Dissertation Generation ... 133

Appendix G: All Publications Published, Submitted and Planned ... 135

Appendix H: ANBP Group Fabrication Lot Number Definition.. 136

Appendix I: Processing Traveler of Metallic Nanostructures on Glass Substrates 137

Appendix J: Processing Traveler of Single Horizontal Si Nanowire Device 145

Appendix K: Processing Traveler of Metallic Fishnet Integrated a-Si Solar Cell...................... 151

Appendix L: Processing Traveler of Metallic Nanostructures Integrated GeSn Photodetector . 163

Appendix M: Permission to Reuse Copyrighted Materials 173

List of Figures

Fig. 2-1 Standard EBL processing flow of fabricating metallic nanostructures on c-Si is demonstrated with lift-off process. 9

Fig. 2-2 The interaction between electron beam and substrate is shown with exposure distribution by forward and back scatterings [37]. 12

Fig. 2-3 Monte Carlo simulation results of different acceleration voltages and resist thicknesses using CASINO. 14

Fig. 2-4 The forward and back scattering effect at 30 kV and 50 kV with the beam broadening radius changes using LMS-MS [40]. 15

Fig. 2-5 The Philips XL30 ESEM modified EBL writer is shown integrated with Nanometer Pattern Generation System (NPGS) [42]. 16

Fig. 2-6 The schematic NPGS system [41] operation process is shown in (a). The integrated CAD software is demonstrated in (b) with beam written strategy schedule interface (c) and EBL writing simulation interface with estimated time consumption (d). 18

Fig. 2-7 JEOL JBX-5500ZD EBL writer is located in High Density Electronics Center (HiDEC) at University of Arkansas, Fayetteville [43]. 20

Fig. 2-8 JEOL JBX-5500ZD system software and sub-functions interfaces are shown [44]. 21

Fig. 2-9 Gas-assisted electron beam deposition (a) and focused ion etching mechanisms (b) are shown [45]. 22

Fig. 2-10 The schematic drawing of FEI Nova Nanolab 200 Dual-beam workstation system configuration (a) is shown with control software interface (b) [46]. 24

Fig. 2-11 The thickness of 6% 950K PMMA at different spin coating on 1 cm × 1 cm samples is shown in (a). The thicknesses at 3000 RPM of PMMA with various concentrations are shown in (b). 26

Fig. 2-12 The comparison between successful and unsuccessful lift-off results is shown with metallic nanodisks arrays. 27

Fig. 2-13 The lift-off considerations in metallic nanostructures fabrication on c-Si substrates are shown with different fabrication results. 28

Fig. 2-14 Lift-off problem trouble shooting process is shown with results. Figure (a) shows the unsuccessful lift-off results of fabricated nanostructures. Figure (b) shows the lift-off result after double spinning of resist. The alternative metal Titanium instead of Gold was utilized for trouble shooting reason as shown in (c). Figure (d) presents the fabricated metallic nanostructures after process improvement. 30

Fig. 2-15 The SEM images show fabricated nanorods array by NPGS (a) and JEOL (b) systems, respectively. The magnified single nanowire is shown. The fabricated patterns array covered 1 mm × 1 mm area shown in bottom left inset of (b). Bottom right inset shows a magnified single nanowire. 32

Fig. 2-16 The left image presents the fabricated nano disks array by NPGS system with different pitch size (diameter: 800 nm, 10 nm Ti and 30 nm Au). The right image presents fabricated SRRs array by JEOL system (200nm line width, 5 μm pitch size, 10 nm Cr and 30 nm Au). The fabricated patterns array covered 1 mm × 1 mm area (bottom left inset). Bottom right inset shows two magnified SRRs. 33

Fig. 2-17 (a) is the fabricated 8 × 10 random SRRs arrays by NPGS system. The geometry parameters were 150nm line width and 2 μm pitch size deposited with 10 nm Cr and 30 nm Au.

Overall fabricated patterns array is shown in bottom left inset. Bottom right inset shows a magnified random SRR. Fig. 2-17 (b) shows the SEM image of fabricated SRR pairs array by JEOL system (40 nm gap, 1.5 μm pitch size, 10 nm Cr and 30 nm Au). 34

Fig. 2-18 The fishnet patterns with various sizes are fabricated on c-Si substrate. The geometry parameters of fabricated structures were: (a) 800 nm line width and 1.6 μm pitch size; (b)300 nm width and 1 μm pitch size; (c) 150 nm line width and 300 nm pitch size; (d) 100 nm width and 1 μm pitch size. 35

Fig. 2-19 The fabricated SRRs array were patterned on ITO covering a 600 μm × 600 μm area shown in (a). The nanorods were deposited on ITO of 100nm width and 1 μm length covering 500 μm × 500 μm area shown in (b).. 37

Fig. 2-20 The CAD design of SRR pairs array is shown. For each gap and L value variations, the 50 × 50 SRR pairs array locates with the period of 1.2 um by 0.8 um in horizontal and vertical directions between each pair. There are 8 arrays in horizontal and 4 arrays in vertical in total.. 38

Fig. 2-21 The SEM and AFM results of two gap values (20nm and 160 nm) of SRR pairs are presented. 39

Fig. 2-22 The schematic CAD design and SEM results of EBL minimum line width test are presented. The achieved metal line width was 45 nm (b), 65 nm (c) and 70 nm (d).................. 40

Fig. 2-23 The measured fabricated line width was larger with increased electron beam dose..... 41

Fig. 2-24 The schematic drawing shows the standard EBL processing flow to fabricate metallic nanostructures on SiO_2 or glass substrates.. 42

Fig. 2-25 The charging effect on glass substrate is shown in (a). The brief schematic drawing of ESEM machine with various vacuum levels is presented with colors in (b)............................... 44

Fig. 2-26 Various metallic nanostructures were patterned on glass substrates. Fig (a) shows the fabricated nanorings with 200nm inner diameter and 300nm outer diameter. Fig (b) presents the nanorods with 2 μm length and 4 μm pitch size. Fig. (c) is the fishnet structure of 120nm width and 1 μm pitch size. Fig. (d) captures the interdigitated electrodes of 200nm spacing and 4 μm finger width. 45

Fig. 2-27 EBL processing flow to fabricate nanostructures on c-Si substrates 46

Fig. 2-28 Nanostructures patterning results on c-Si substrates are presented with the RIE machine shown in (a) from ref. [48]. The tentative etching results are shown from (b) to (d). 47

Fig. 2-29 The FIB pattern design of 2 × 2 separate fishnet array is presented with maximum writing time. 49

Figure 2-30 The results of electron beam assisted deposition and FIB assisted etching are presented. 50

Fig. 2-31 Fabricated fishnet structures covered relative large area 100 μm × 100 μm within 30 minutes. The achieved line widths were 200nm (a) and 500 nm (b), respectively. The duty cycle was 1:1 ratio. 51

Fig. 2-32 The fabricated single nanowire device by FIB is presented with SEM images shown before and after etching. (a) and (b) show before etching condition of two positions on one nanowire device. (c) and (d) show the corresponded device positions after etching condition. The nanowire in yellow box was the target under test 52

Fig. 2-33 The experiment results of nanostructure patterning on thin film metals show strong interaction between the incoming gases and metal atoms. 53

Fig. 2-34 The mechanisms of EBL field stitching and exposure alignment are presented with evaluation results. 55

Fig. 2-35 The schematic drawing of horizontal nanowire device is presented. 56

Fig. 2-36 The brief fabrication results of single horizontal Si nanowire device are demonstrated with (a) global contacts fabrication, (b) align markers CAD design; (c) SEM image before alignment; (d) SEM image after alignment. 57

Fig. 2-36 The SEM images show two fabricated single horizontal Si nanowire devices with magnified image shows only the nanowire and local electrodes. 57

Fig. 3-1 The calculated model of the DOS distribution in a-Si is shown with marked exponential band tails and defect states. 60

Fig. 3-2 The normalized SRH saturation current densities of Schottky contact (black dashed line) and p-i-n structure (red solid line) a-Si solar cells are shown corresponding to different carrier lifetime [54]. © 2013 IEEE. 61

Fig. 3-3 The numeric simulation results are shown [54]. The schematic structure of the simulated solar cell is shown in (a). The typical electric field distributions of the solar cell at the wavelength of 632 nm are shown in (b). The reflection and absorption spectra of the solar cell are shown in (c). The photocurrent generation spectrum is calculated shown in (d). © 2013 IEEE 62

Fig. 3-4 The 3D processing flow shows the a-Si mesa patterning of metallic fishnet structure integrated Schottky contact a-Si solar cell. 63

Fig. 3-5 The global contacts and fishnet structures are integrated as fishnet integrated a-Si Schottky contact solar cells. 65

Fig. 3-6 The Al and a-Si ohmic contacts test structure is presented. 66

Fig. 3-7 The fabricated Al/a-Si ohmic contact structure is presented with I-V measurement results. 67

Fig. 3-8 The fishnet structure was integrated on 800 μm × 800 μm a-Si mesa forming Schottky contact a-Si solar cell. 68

Fig. 3-9 The presented J-V curves show the consistent conductivities on different mesa sizes... 69

Fig. 3-10 The temperature dependent current-voltage measurement was conducted from 270K to 340K... 70

Fig. 3-11 The comparison between cells with and without fishnet structures are shown. Fig. (a) shows the dark I-V curve and (b) shows the light measurement result. 71

Fig. 3-12 The photoresponse and quantum efficiency measurement results are shown. The devices integrated with fishnet Schottky contact and blanked metal Schottky contact were compared.. 72

Fig. 4-1 The schematic band structure shows the effect of Sn alloying on the band structure of Ge [58]... 75

Fig. 4-2 It shows the cross sectional TEM image of $Ge_{0.94}Sn_{0.06}$ grown by UHVCVD [73]. The top image shows the GeSn layer morphology. The middle one shows the uniformity of film. The bottom one shows the GeSn and Si interface with indicated misfit dislocations. 77

Fig. 4-3 The top image shows the cross-sectional schematic drawing of fabricated GeSn photodetector [84]. The 100 nm SiO_2 is applied as antireflection coating. The top contact is made by 10 nm Cr and 200 nm Au. The bottom image shows the optical image of devices with different lattice geometry sizes from 250 μm × 250 μm and 1 mm × 1mm................................ 78

Fig. 4-4 The VASE variable angle spectroscopic ellipsometry system is shown in operation mode (this picture is taken by author at Dr. Shui-Qing Yu's lab on March 10 2014)............................ 83

Fig. 4-5 A schematic drawing of ellipsometry experiment is shown with linearly polarized light [103]... 84

Fig. 4-6 The typical processing flow is shown for ellipsometry measurement. 85

Fig. 4-7 The system calibration windows of x-y and z directions are shown. (a) shows the x-y plane reflection monitoring window with crossing marks. (b) presents the z direction intensity monitoring window. 86

Fig. 4-8 Ellipsometry measurement configuration and results on standard oxidized silicon wafer are shown (the equipment setup picture is taken by author at Dr. Shui-Qing Yu's lab on March 10 2014). 87

Fig. 4-9 The data acquisition and generated models are shown. (This is a screen shot taken by author at Dr. Shui-Qing Yu's lab on March 10 2014) 89

Fig. 4-10 The proposed H-shape metallic nanostructures are shown in (a). The comparison of transmission measurement on different baselines is shown in (b). 90

Fig. 4-11 Transmission measurement results of H shape nano antennas with various bridge widths are shown with two different polarized directions. The results are stacked for easy reading. 92

Fig. 4-12 Stacked reflection measurement results of H shape nano antennas with various bridge widths are shown with two different polarized directions. 93

Fig. 4-13 Absorption measurement results of H shape nano antennas with various bridge widths are shown with two different polarized directions. The results are stacked for easy reading. ... 94

Fig. 4-14 Comparison of the maximum resonant wavelengths of s-polarized direction between measurement results and published data [104]. 96

Fig. 4-15 It shows the detailed heteroepitaxial grown structures of $Si/Ge/Ge_{1-x}Sn_x$ with two different Sn contents (327 nm for x=0.009 and 240 nm for x=0.07). 97

Fig. 4-16 This figure shows GeSn photodetector processing flow. The detailed process is: (a) Cleaning process of Si/Ge/GeSn substrate; (b) AZ4330 coating at 3000RPM and baking at 95 ℃; (c) Photolithography of AZ4330 and developing; (d) RIE of GeSn and Ge layers to form photodetector mesa; (e) AZ4330 removal by resist stripper; (f) AZ5214 coating at 3000RPM and baking at 95 ℃; (g) exposure, image reverse baking at 110 ℃ and developing; (h) metal deposition of 10 nm Cr and 200 nm Au; (i) lift-off process after metal deposition to removal resist. 98

Fig. 4-17 This schematic processing flow demonstrates the metallic nanostructures integrated GeSn photodetector fabrication. The detailed process include: (a) Cleaning process of GeSn photodetector; (b) PMMA coating at 3000RPM and baking at 180 ℃; (c) Electron beam exposure with certain structure patterns; (d) metal deposition of 10 nm Cr and 50 nm Au; (i) lift-off process after metal deposition to removal PMMA........ 100

Fig. 4-18 This shows the schematic drawing of FTIR based IR photoresponse measurement setup. The absolute responsivity at 1.55 μm is measured with laser through optical pass 1. The real device measurement is based on FTIR through optical pass 2 without flip mirror. 101

Fig. 4-19 The SEM images of fabricated H shape nano antennas integrated $Ge_{0.991}Sn_{0.009}$ photodetector. The figure (a) shows the overall image of detector on the mesa size of 500 μm × 500 μm. The figure (b) shows the magnified image of antennas. The bridge width shown in the inset is 50 nm and the spacing is 800 nm........ 102

Fig. 4-20 The photoresponse curves of fabricated H shape nano antennas integrated GeSn photodetectors is shown here. 103

Fig. 5-1 It presents the SEM images of fabricated interdigitated electrodes integrated $Ge_{0.93}Sn_{0.07}$ photodetector. The figure (a) shows the overall image of detector on 1 mm × 1 mm mesa. The

figure (b) shows the magnified image of electrodes. The width of electrode is 2 μm and the spacing between electrodes is 4 μm. 105

Fig. 5-2 The dark I-V measurement results show ohmic contact between metals and GeSn layer. 106

Fig. 5-3 The photoresponse comparison of fabricated $Ge_{1-x}Sn_x$ (x=0.009 and x=0.07) based photodetectors is shown here. The device performance with and without interdigitated electrodes is also presented. 107

Fig. 5-4 The comparison shows a slightly broader response of the detector without SiO_2 as passivation layer. 108

Fig. 5-5 The AC responsivity of $Ge_{0.991}Sn_{0.009}$ (a) and $Ge_{0.93}Sn_{0.07}$ (b) photodetectors with and without interdigitated electrodes are shown at 1.55 μm at room temperature. 109

Fig. 5-6 The specific detectivity of $Ge_{0.991}Sn_{0.009}$ (a) and $Ge_{0.93}Sn_{0.07}$ (b) photodetectors with and without interdigitated electrodes are shown at 1.55 μm at room temperature. 110

Fig. 5-7 The temperature dependent photoresponse of interdigitated electrodes integrated $Ge_{0.991}Sn_{0.009}$ (a) and $Ge_{0.93}Sn_{0.07}$ (b) photodetectors are shown. 111

Fig. 5-8 The temperature dependent AC responsivity of interdigitated electrodes integrated $Ge_{0.991}Sn_{0.009}$ (a) and $Ge_{0.93}Sn_{0.07}$ (b) photodetectors are shown at 1.55 μm. 112

Fig. 5-9 The temperature dependent specific detectivity of interdigitated electrodes integrated $Ge_{0.991}Sn_{0.009}$ (a) and $Ge_{0.93}Sn_{0.07}$ (b) photodetectors are shown at 1.55 μm. 113

List of Tables

Table 2-1 The experiment design and results for lift-off trouble shooting are shown. 31

Table. 2-2 The summary of EBL dose calibration is presented with various geometry parameters of fishnet structures. 36

Table 2-3 The achieved minimum feature size with covered area of different patterns is summarized. 37

Table 2-4 The RIE processing parameters for nanostructures patterning on c-Si are summarized. 47

Table 2-5 The color setting of bitmap CAD files used in FIB patterning is summarized. 48

Table 2-6 The brief summary of fabrication process development of metallic nanostructures on various substrates and nanostructures patterning on c-Si substrates. 54

Table 3-1 The applied PECVD parameters of 300 nm thick a-Si deposition are shown.............. 64

Table 3-2 The a-Si RIE dry etching parameters are used to etch stop at Al layer. 64

Table 4-1 The detailed parameters of dry etching and descum is shown. 99

Chapter 1: Introduction

Efficient light concentration and manipulation are major challenges for future Group IV light detection devices such as photovoltaic devices and photodetectors. Plasmonic technology shows promising future that investigates unique optical properties of metallic nanostructures to guide and manipulate light in subwavelength scale with better absorption performance. By integrating metallic nanostructures on light detection devices, increased light absorption has been observed. However, the energy loss during the transport of photon generated carriers between contacts has not been considered simultaneously. A thorough consideration of both optical and electrical properties of the metallic nanostructures integrated light detection devices has not been fully understood. Moreover, considering the intrinsic properties of plasmonics, an optimized device platform to fully utilize these integrated metallic nanostructures is still under investigation.

As one of the future alternative energy supply candidates, the material cost of photovoltaic devices has been the barrier holding its worldwide applications. Various methods have been applied to reduce the cost including innovative materials development, improved fabrication processes and special device structure consideration. However, the achieved energy conversion efficiency has to be further improved to compete with fossil fuels. Decreasing the device geometry size is one of the direct ways to reduce the cost. By integrating metallic nanostructures on photovoltaic devices, the light absorption and energy conversion efficiency have been reported higher than devices without them.

Meanwhile, integration of optoelectronics and high speed Si based electronics has been investigated for several decades. Although many technology developments have been achieved, the integration level is relative low comparing to the electronics development which directly follows “Moore’s law”. The possible reasons could be the size of optical components, the

heterogeneity of materials with Si and the cost. For example, the III-V material based photodetectors have been successfully integrated with CMOS circuits by wires between components. Nevertheless, the increased device density on single chip by much more components integrated approaches the intrinsic limitation of copper wires. Comparing to the III-V heterostructures hybrid-integrated on Si, the group IV photonics has attracted much more interest in recent years. With integrated group IV based photodetectors, the optical interconnect could provide lower signal losses, higher speed and possibly fully CMOS fabrication compatibility. However, current Si/Ge detectors need higher temperature growth to achieve direct band gap absorption and the operation wavelength is shorter than 2 μm. Therefore, a low cost CMOS compatible infrared photodetectors is required with operating wavelength beyond 2 μm at room temperature.

Considering these two light detection devices, integrating metallic nanostructures has been utilized to achieve better light absorption. Although plasmonics has been discussed as one of the possible solutions for low cost light detection devices, only the optical performance improvement has been addressed with exact conclusion. Most researchers have demonstrated plasmonic enhanced light detection devices with increased absorption and energy conversion efficiency [1-8]. The optimized methods are normally analyzed and simulated from optical side which maximizes the overall light absorption. However, the electrical properties of these metallic nanostructures have not been thoroughly studied. The device electrical properties such as carrier transport and collection from the metallic nanostructures as light trapping center to contacts have not been optimized even included in these models. Without considering the recombination processes in photon generated electro-hole pairs, the established device model is not accurate and might not be able to provide accurate guidance for future device development.

In this dissertation, the typical light detection devices integrated with metallic nanostructures have been developed considering both the electrical and optical aspects to improve energy conversion efficiency.

1.1 Metallic Nanostructures Integrated Light Detection Devices

If embedded nanoparticles sizes are much smaller than the wavelength of incident light, the metallic nanostructures could exhibit a dipolar surface plasmon resonance based on Mie's theory [9]. The electric field associated with the light waves exerts a Coulomb force on the conduction band electrons of metallic nanostructures. When the incident light frequency is far away from the intrinsic plasmonic resonant frequency of metallic nanostructures, no resonant oscillation of free electrons occurs. With the approaching photon frequency of incident light, the plasmonic enhancement is induced by the coherent oscillation within metallic nanostructures. With tens of nanometer metallic nanostructures, the incident light on metallic nanostructures can be strongly scattered with negligible absorption. However, as the particle size increases, the dipolar plasmon resonance shifts to longer wavelength and the resonant peak is extended. With the size of the nanoparticle approaching wavelength, the dipolar approximation is not valid to estimate the scattering cross section. To determine the resonance frequency, the metal material, structure geometry and dielectric environment need to be considered. The resonance peak will shift to longer wavelength with increased dielectric constant of surrounding area.

The basic mechanisms of plasmonic enhanced photovoltaic devices and photodetectors can be explained in three ways. First, the nano-scale metallic structures can be treated as scattering center of incident light to increase the passing length within absorption layer. Most metallic nanoparticles enhanced devices are designed in this way. Second, the induced strong near field effect by the localized surface plasmonic resonance of metallic nanostructures

increases the absorption. Third, as the scattering center excite surface plasmon propagation (SPP) along metallic nanostructure surface. The momentum mismatch between incident light and SP mode can be overcome by period metallic structures and prisms. With the mode propagating at interface, more energy will be absorbed in the semiconductor layer through evanescent wave.

Along with the nanofabrication technique progress, innovative plasmonic enhanced photovoltaic and photodetectors have been developed. In 1985, the grating structure has been fabricated by optical lithography to couple incident light into surface plasmonic waves confined to the air-metal interface to enhance quantum efficiency (QE) internal photoemission detectors [10]. Gratings with a period of 2 μm and a line/space ratio of ~1/3 were fabricated on heavily doped p-InP. Meanwhile, another grating structure was fabricated holographically with a UV laser (325nm) on photoresist film to investigate the influence of SPP on the reflection spectra of $Ag/Al_2O_3/Al$ and $Al/Al_2O_3/Al$ junctions detectors [11]. The SPP photon coupling efficiency was optimized as a function of the grating morphology and dielectric layers. In early 1990s, plasmonic enhanced organic solar cells were investigated by many research groups [12-16]. Metal-oxide-metal tunneling junction and Schottky-barrier organic thin film solar cell copper phthaloeyanine (CuPc) have been studied with SPP excited by attenuated total reflection (ATR) coupling method [12-14, 16]. Due to the lack of nanofabrication techniques, metal nanoclusters have been incorporated at the ITO-CuPc interface to study the plasmonic effect on organic solar cells [15]. With the development of holographic technique, a 2D hexagonally textured silver surface has been fabricated to study SPP that propagate at Ag/air interface [17]. The chemical synthesis method to form metal islands film was introduced to improve the sensitivity of very thin semiconductor photodetectors [18, 19]. After very thin (~10 nm) metal film deposition, the samples were annealed under flowing nitrogen at 300 °C within certain time to coalesce into

metal islands. Beyond chemical methods, electron beam lithography (EBL) and focused ion beam (FIB) are also applied to fabricate metal nanoparticles [20]. Interference lithography, which is able to fabricate sinusoidal patterns but not sharp corner patterns, is also utilized to investigate the absorption of using periodic metallic gratings structures in a-Si thin films solar cells [21]. After 2005, various well-organized metallic nanostructures have been integrated on solar cells and photodetectors due to the maturity of nanofabrication technologies. In 2006, the first nano antenna integrated Ge photodetector was demonstrated with C-shape nanoaperture by using focused ion beam (FIB) [2]. As reported by K. Nakayama *et al.* [5], Ag nanoparticles with a diameter at 110 nm were patterned on thin GaAs solar cell by anodic aluminum oxide template. The particle spacing and height were varied to investigate the plasmonic effect on efficiency improvement. Nanoimprint lithography is reported as fabrication technique to patterning holes on the Ag back contact of an n-i-p a-Si:H solar cell [7]. The demonstrated device showed an efficiency increase from 4.5% to 6.2%. Various nanofabrication techniques have been developed based on applications. They all have their own advantages and limitations. The interference and nanosphere lithography can pattern well-organized periodic repeatable structures with higher throughput. The nanoimprint and anodic aluminum oxide template techniques can provide relative good pattern resolution with prefabricated mask. However, the FIB and EBL are two maskless fabrication techniques with much higher resolution and more flexibility in pattern design. Although the throughput is relative low, the FIB and EBL are still two ideal fabrication technique candidates in research environment. In this dissertation, the FIB and EBL were utilized as fabrication tools for photovoltaic devices and photodetectors.

1.2 Overview of This Dissertation

The target of this dissertation was to first develop nanofabrication processes of different metallic nanostructures on various conductive and nonconductive substrates using EBL. Meanwhile, the nanostructures patterning processes on c-Si were developed using EBL dry etching and FIB techniques. Furthermore, based on a developed fabrication integration platform and established processing parameter data base, two typical light detection devices integrated with certain metallic nanostructures were developed that included fishnet integrated Schottky contact a-Si solar cell and a metallic nanostructures integrated GeSn photodetector. Not only the optical properties but the electrical improvement was under consideration during device development.

The topics in this dissertation are organized as follows:

Chapter 2 presents the fabrication process development of metallic nanostructures on various substrates including crystalline silicon (c-Si), amorphous silicon (a-Si), Indium Tin Oxide (ITO) and glasses. A single horizontal Si nanowire device was developed as a process integration platform that can be easily transferred and integrated with other typical 2D materials and devices. Meanwhile, the fabrication results of nanostructures patterning on c-Si by FIB and EBL are presented.

Chapter 3 introduces the fabrication and characterization of metallic fishnet nanostructure integrated Schottky contact a-Si solar cell. The detailed continuous band structure of a-Si was calculated with the analysis of possible nonradiative recombination loss. Through electrical and optical measurements, the device performance was evaluated.

Chapter 4 provides the development process of metallic nano antennas integrated GeSn photodetectors. The optical characterization results of fabricated metallic nano antennas on thin

ITO coated glass substrates were presented first. The transmission, reflection and absorption measurements were conducted on a spectroscopic ellipsometer. With different geometry parameters, the resonant wavelengths consistently changed in infrared wavelength range. Furthermore, the device fabrication and integration processes were presented.

Chapter 5 shows the further investigation of metallic interdigitated electrodes integrated GeSn photodetector based on the development of previous devices. Through the systemic electrical and optical characterization of two Sn composition devices, the optimized metallic nanostructures integrated light detection devices were developed. The critical parameters to develop high efficiency light detection devices were discussed.

Chapter 6 summarizes the completed work and suggests possible directions for future research in metallic nanostructures integrated light detection devices.

Chapter 2 Fabrication and Process Development of Nanostructures Using EBL and FIB

2.1 Introduction

Metallic nanostructures integrated light detection devices have been studied for many years. The research on the application of metallic nanostructures introduced plasmonic effect can be tracked from 1980s [22, 23]. The exploited applications include biological sensor [22-26], nanooptics [27, 28], nanophotonics [20, 29, 30] and optical metamaterials [31]. Beyond that, solar cells and photodetectors are under heavily investigated in recent several years. A variety of studies have been conducted to integrate the metallic nanostructures on these light detection devices [1, 3, 13, 15, 19, 32-36]. The possible mechanisms of plasmonic enhancement by these structures include far field scattering, localized light confinement by enhanced optical field and surface plasmonic resonance. However, the detailed theoretical study is still under development. In order to fully understand the device properties guiding future device development, it is necessary to develop device fabrication and integration processes in which nanofabrication of metallic nanostructures needs to be first established. Meanwhile, Si based nanostructure fabrication techniques are also essential for future possible optical integrated circuit.

Electron beam lithography (EBL) and focused ion beam (FIB) are two developed techniques for nanostructures patterning on various substrates without quartz mask. The EBL requires electron beam sensitive resist as a pattern transfer mask. Since the electrons with smaller wavelength are utilized instead of photons, the achievable smallest feature size is down to the 5 nm range that is sufficient for research environment. However, the throughput is a major concern since it is a series exposure process. The FIB is a maskless nanofabrication technique in which dielectric or metal structures can be fabricated directly by gas assisted ion beam etching or gas assisted electron/ion beam deposition. Nevertheless, the available metal materials are limited

and complicated device integration capability is insufficient. Even so, it is now widely used as device prototype fabrication technique.

2.2 Electron Beam Lithography

The general metallic nanostructures patterning process using EBL is shown in Fig. 2-1 based on interaction between focused electrons and resist molecules. After EBL exposure, the chemical properties of exposed resist area change leading to solubility difference in certain chemicals (developer). Followed by metal deposition and lift-off, certain metallic nanostructures are formed on the substrate. The detailed processing parameters will be discussed later in this chapter.

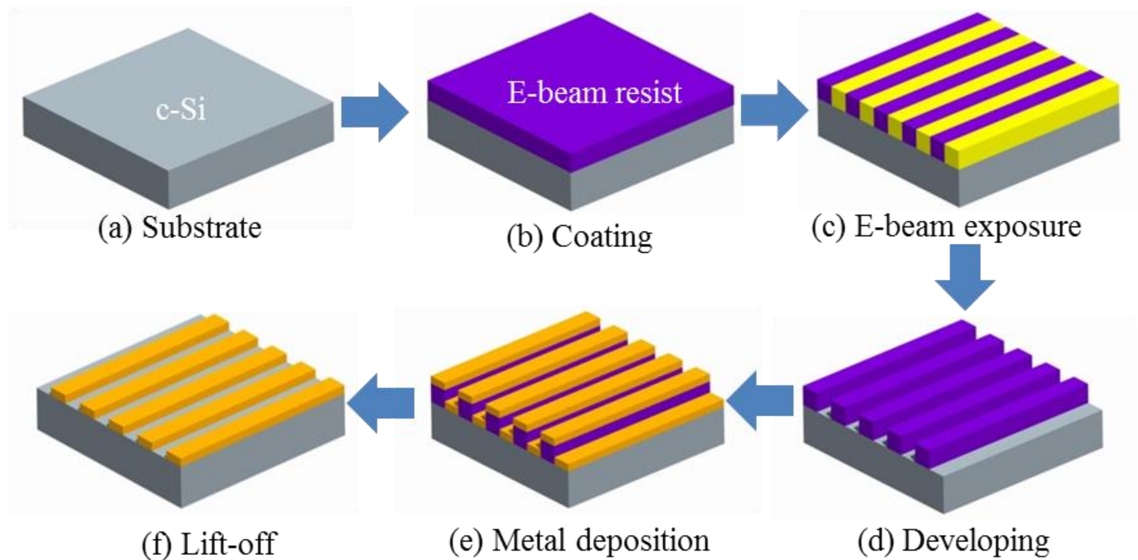

Fig. 2-1 Standard EBL processing flow of fabricating metallic nanostructures on c-Si is demonstrated with lift-off process.

The typical electron beam resists can be classified as positive and negative based on the solubility of exposed region in developer. As positive resists, the molecular weights decrease due to polymer chain scission by exposure. This leads to the exposed area can be easily dissolved in developer. As negative resists, the crosslink occurs after electron beam exposure that causes the exposed area to be hardly dissolvable in developer. Poly(methyl methacrlylate)

(PMMA) and ZEP-520 have been the most widely used positive e-beam resists. PMMA has very high resolution and low contrast corresponding to various molecule weights. Several concentration options are available corresponding to different film thickness. No shelf or film life issues exist with PMMA. Beyond that, it is not sensitive to white light that makes it useful in non-ideal clean room environment. However, because of dry etching resistance is relatively poor it is not used as dry etching hard mask. ZEP-520 is a positive tone resist that has comparable resolution and contrast of PMMA. Most remarkable characteristic is 10 times dry etching resistance that makes it an ideal candidate as dry etching mask material. In this dissertation, PMMA with different molecule weights and concentrations (2% and 4% 495K, 6% and 8% 950K) and ZEP-520 were used as EBL resists for process development and device fabrications. Here the PMMA was used in the processing flow as example. After coating and pre-baking (Fig. 2-1 (b)), the PMMA thin layer was exposed by electron beam with certain moving strategy on substrate (Fig. 2-1 (c)). After exposure, the exposed PMMA was dissolved in the developing process leaving the unexposed area covering by PMMA (Fig. 2-1 (d)). In the following metal deposition, the deposited metals covered the whole substrate. At the exposed area, the metals were deposited on substrate directly. At unexposed area, the PMMA sat between the metal layer and substrate (Fig. 2-1 (e)). After immersed in certain resist remover chemical (stripper), at unexposed area the PMMA layer was dissolved always with the metal layers above. This left the unexposed area clear (Fig. 2-1 (f)). Since the metal layers contact directly with substrate at exposed area, certain metal patterns could be formed.

The feature size and pattern quality relied on different parameters including electron beam acceleration voltage, scanning field, resist thickness, beam current, spot size, objective lens aperture, pattern spacing, etc. During EBL exposure, the electrons scattered by resist molecules

and substrate atoms resulted in forward scattering and back scattering. Fig. 2-2 shows the schematic drawing about the incident electrons, forward and back scattered electrons [37]. If the electrons are scattered in large angle directions, the adjacent resist area might have higher chance interact with unexpected electrons. After developing, the pattern area could be much wider than the exposure pattern which is called proximity effect. With higher acceleration voltage, the achieved minimum feature size is smaller. Typically, the required dose to expose a certain volume of resist is constant. As shown in equation 2.1, with higher beam current, the required exposure time (dwell time) is less.

$$required\ dose\ (Coulomb) = beam\ current(Ampere) \times dwell\ time(second) \tag{2.1}$$

However, the beam spot size is larger due to the higher current. Furthermore, changing the objective lens configuration and aperture size can also increase the resolution. With more objective lens involved and smaller aperture size, the beam spot size and exposure field are both decreased. With certain metal layer thickness, the EBL exposure parameters needed to be optimized.

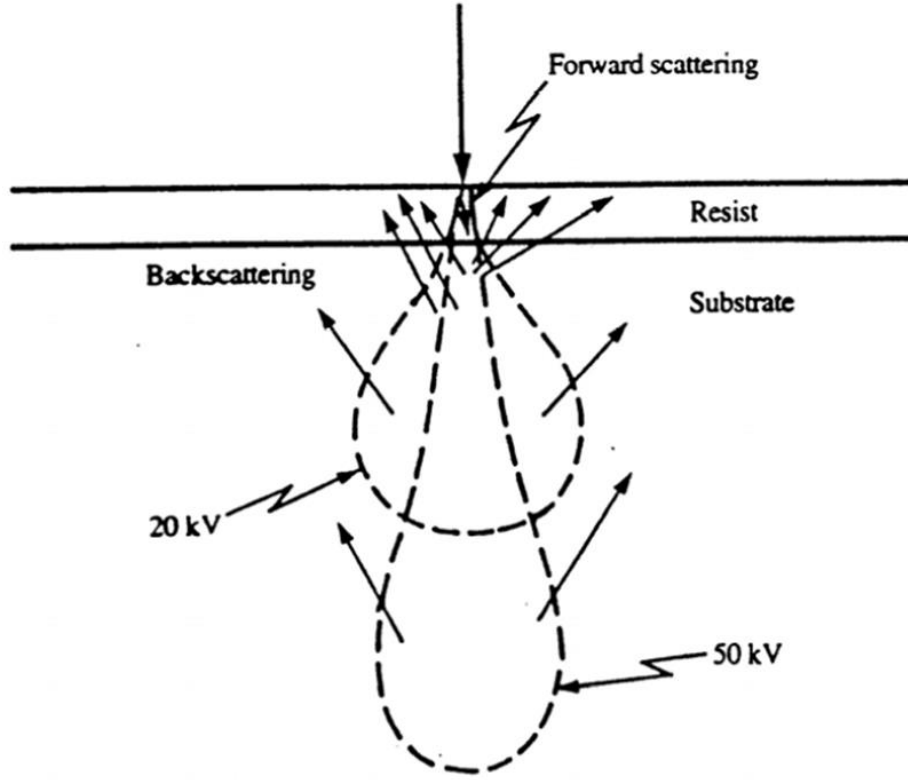

Fig. 2-2 The interaction between electron beam and substrate is shown with exposure distribution by forward and back scatterings [37].

To successfully develop the fabrication process, the interaction between electrons and substrates needs to be fully understood. Both of the forward and back scatterings can be described by Gaussian distribution [38]. The exposure amplitude is calculated as:

$$f(r) = \frac{1}{\pi(1+\eta)}\left(\frac{1}{\alpha^2}e^{-\frac{r^2}{\alpha^2}} + \frac{\eta}{\beta^2}e^{-\frac{r^2}{\beta^2}}\right) \quad (2.2)$$

where $f(r)$ is the exposure amplitude at the substrate surface with distance r away from the substrate beam center position. The parameters α and β are the distribution width of forward and back scatterings, respectively. Parameter η reflects the ratio between back scattered beam and incident electron beam. The beam broadening radius can be calculated using following equation 2.3:

$$d_i = \left(\frac{Z}{E_0}\right) \times t^{\frac{3}{2}} \times \left(\frac{\rho}{A}\right)^{\frac{1}{2}} \tag{2.3}$$

The parameter $d_i$is the broadening radius at the surface of substrate. E_0 is the beam energy. The resist properties are presented by parameters t as film thickness, ρ as material density, Z as atomic number and A as atomic weight. Following this equation, with thicker resist or lower beam energy more electrons will be scattered in a lateral direction and vice versa.

Based on this double Gaussian model, the electron beam and sample interactions can be analyzed through typical Monte Carlo simulation. In this dissertation, the Monte Carlo simulation software CASINO [39] and LMS-MS [40] were used and compared. These two can simulate the large amount electron trajectories in solid especially designed for low beam interaction. It provided the prediction to guide the utilized parameters in electron beam lithography such as acceleration voltage, film thickness and pattern spacing. The collected data included backscattered coefficient, electron penetration depth and scattering width of different films. As shown in Fig. 2-3, the scattering effects of electron beams at different working conditions were presented using CASINO. The scattering width was 40 nm after 30 kV electron beam went through a 100 nm PMMA layer. With a thicker PMMA layer of 500 nm, the scattering width at the same voltage extended to 640 nm, which tended to have a strong proximity effect on adjacent patterns. If the voltage increased to 50 kV, the scattering width fell to 300 nm. With higher voltage, the smaller scattering width was predicted. Furthermore, the 100 kV electron beam can penetrate 1000 nm thick PMMA with almost the same scattering width of 300 nm. After the simulation, the general exposure parameters were decided as high acceleration voltage, low resist thickness and smaller beam spot size.

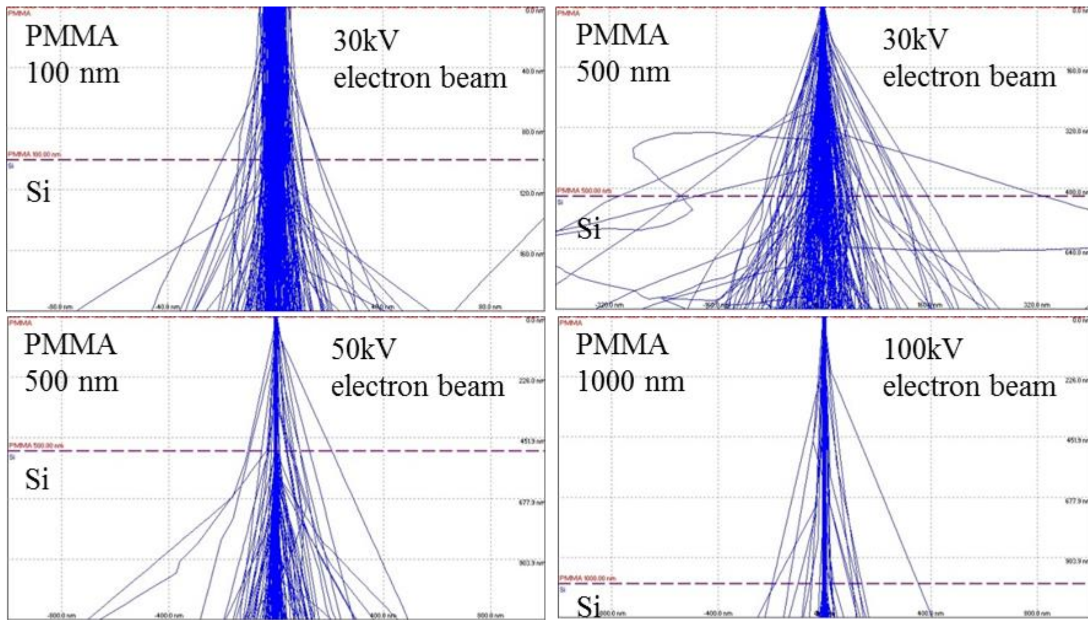

Fig. 2-3 Monte Carlo simulation results of different acceleration voltages and resist thicknesses using CASINO.

Using LMS-MS [40], the trajectories of forward and back scattered electrons can be simulated with estimated broadening radius. As shown in Fig. 2-4, the forward scattering radius at the interface between 100 nm PMMA and 1 μm Si was 17.5 nm at 30 kV and 10 nm at 50 kV which matched with the equation 2.3 within 10% error. With well calibrated electron beam at higher acceleration voltage and thinner resist, the resolution of nanofabrication was under control. In contrast, with a higher beam energy at 50 kV the back scattering was much wider up, to tens of microns level, with energy intensity decreased gradually. In general, the exposure effect by back scattering electrons can be neglected because the energy levels of scattered electrons are lower than the critical dose which is the minimum dose to change the solubility of resist.

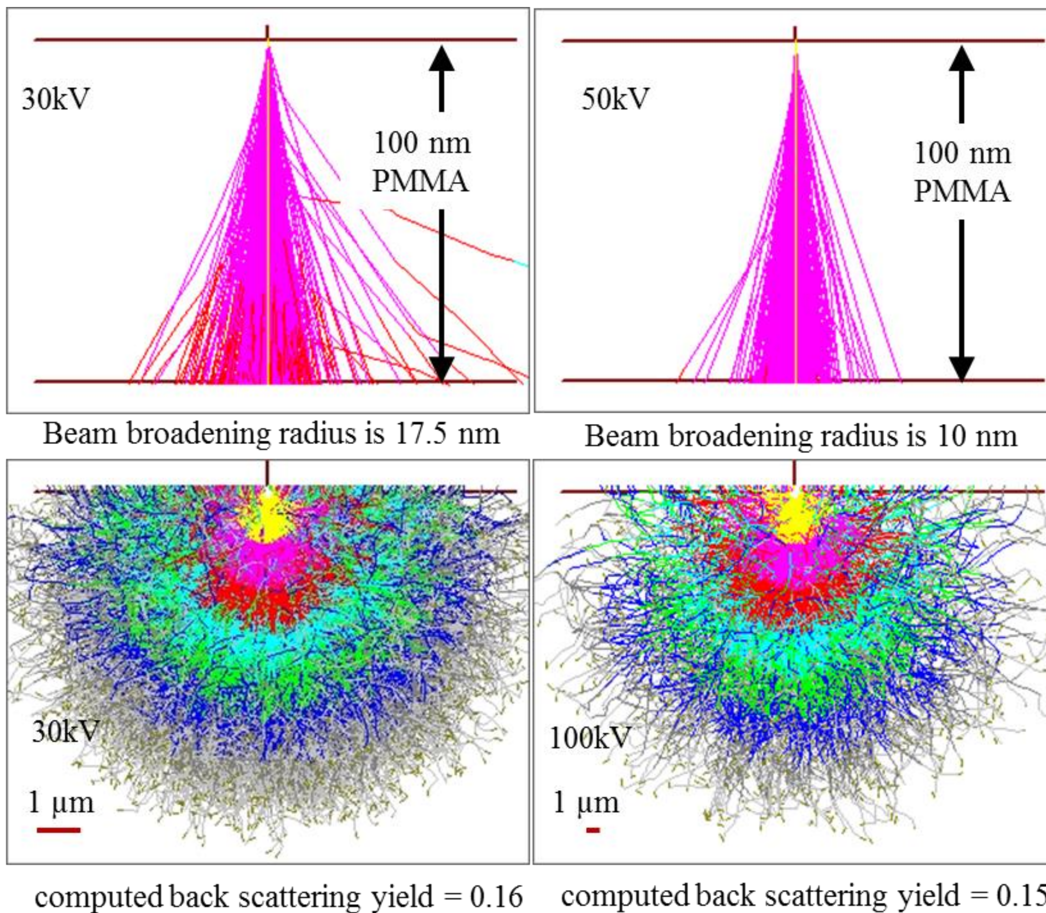

Fig. 2-4 The forward and back scattering effect at 30 kV and 50 kV with the beam broadening radius changes using LMS-MS [40].

In this dissertation, two EBL systems were utilized to conduct process development including a Philips XL30 ESEM modified EBL machine integrated with Nanometer Pattern Generation System [41] (it will be called NPGS system in this dissertation) and a dedicated JEOL JBX-5500ZD EBL writer (it will be called JEOL EBL writer in this dissertation). Both of these two systems had their unique advantages and limitations. The processing development started on the NPGS system because of its flexibility and ease to use. Based on the need of smaller structures and higher alignment resolution, the developed processes were seamlessly transferred to the JEOL machine. Further processing integration and device development were

conducted on JEOL EBL writer. The detailed information will be discussed in next several chapters.

In the NGPG system, the electrons were accelerated by voltage up to 30 kV to the sample in a vacuum of 10^{-6} Pa. Through the adjustment on condenser lens, objective aperture and working distance, higher resolution EBL exposure was achieved combined with dedicated NPGS control software. Since this SEM used a field-emission source, the beam diameter was extremely as small as 2 nm at 30kV. Fig. 2-5 below shows this SEM modified EBL system.

Fig. 2-5 The Philips XL30 ESEM modified EBL writer is shown integrated with Nanometer Pattern Generation System (NPGS) [42].

The NPGS system was an economical direct write electron beam lithography system. It included a commercial SEM machine controlled by NPGS software integrated computer. The schematic system configuration and operation procedures are shown in Fig. 2-6. As shown in Fig. 2-6 (a), the CAD pattern design was first generated by the integrated DesignCAD software (Fig. 2-6 (b)). Other commercial CAD software such as AutoCAD could also have been used but would have needed one more step of file conversion. After loading the CAD file into the writing plan module, the integrated DAC converter analyzed the CAD file and generated a series

voltage signals to control the beam scan traces on samples. A typical EBL sample mount with standard gold particles on carbon and another Faraday cup was used to conduct a resolution test and current measurement. With measured current information and CAD design, the detailed exposure information was organized in the control software shown in Fig. 2-6 (c) including exposure time, pattern sequence and overall stage movement based on the required electron dose. After general calibration on the scanning electron microscope system, the NPGS software took over to guide the stage movement and conduct exposure according to the scheduled EBL writing strategy. Detailed pattern quality did vary based on systems with different beam acceleration voltage, beam spot size, focus condition, stage speed, etc. The software also provided the exposure simulation function that was needed to examine the whole exposure process and estimate the total writing time (Fig. 2-6 (d)).

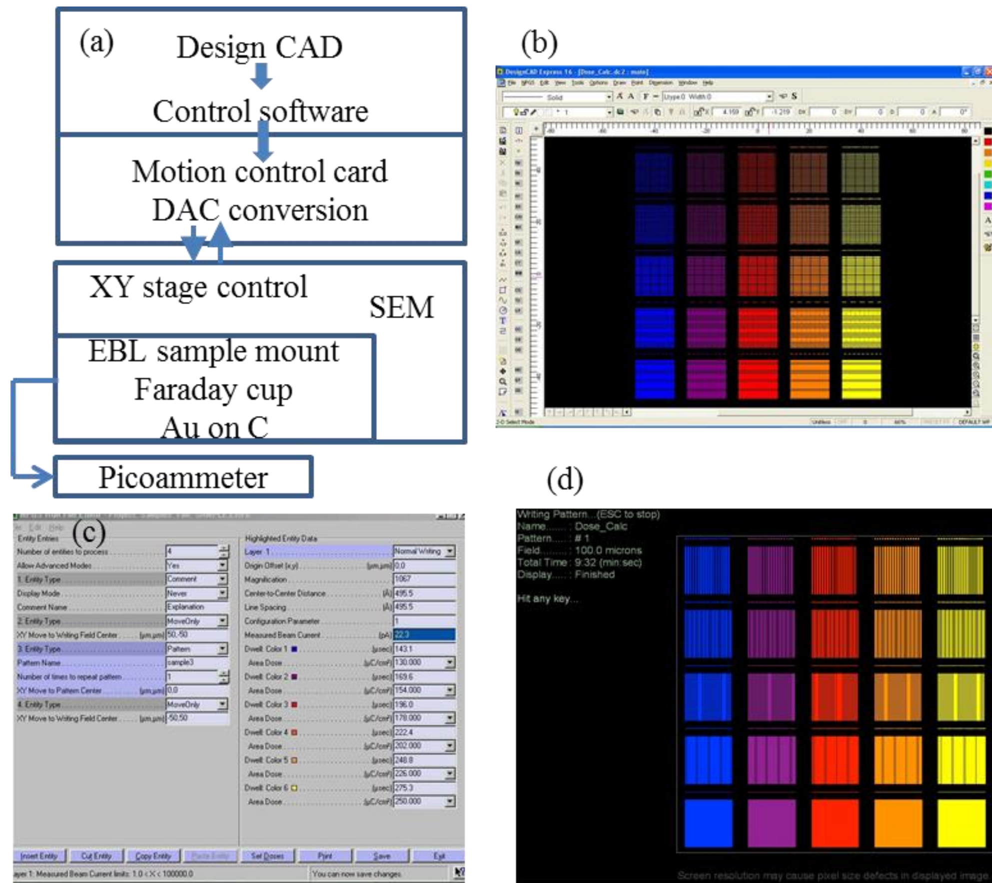

Fig. 2-6 The schematic NPGS system [41] operation process is shown in (a). The integrated CAD software is demonstrated in (b) with beam written strategy schedule interface (c) and EBL writing simulation interface with estimated time consumption (d).

With larger scan fields, the resolution of the NPGS system typically decreased due to the SEM constant. For the NPGS system, the magnification and scan field followed equation 2.4:

$$magnification \times scan\ field = constant \tag{2.4}$$

The constant value in this Philips XL30 ESEM was 100540. The typical EBL exposure parameters using the NPGS system were 30kV acceleration voltage, 10 nm beam spot size, 10 pA exposure current, 10 μm × 10 μm field size with beam blanker control.

This SEM based EBL system was economical, flexible and easy to use. However, the feature size, writing speed, field distribution and moving accuracy was limited by the electron microscope intrinsic properties. Since the beam was designed for electron imaging, it was not

well controlled to stabilize at a certain spot size. With increased field size (hundreds of microns level) the beam resolution decreased dramatically. The writing speed was limited by the relative low speed of DAC card. Moreover, the stage moving accuracy could not be guaranteed due to the lack of stage movement monitoring.

The JEOL JBX-5500ZD is a dedicate electron beam lithography system with a minimum line-width specification below 10nm. Fig. 2-7 shows the actual machine located in the clean room at University of Arkansas Fayetteville High Density Electronics Center (HiDEC). The maximum capacity was a 4" wafer that was ideal for research and development environment. The ZrO/W thermal field emitter was utilized for electron production and was capable of generating electron beam as small as 4 nm in diameter. Two electron beam acceleration voltages were available for use at 25kV and 50kV. With integrated vector scanning system, the single scan field could be as large as 2mm. The larger writing area was achieved through field to field stitching process that the stage movement accuracy well below 10 nm allowed. The HeNe laser interferometer was used to calibrate actual stage position with 0.62nm errors in both the x and y directions by a closed loop servo control that is the critical factor for EBL. The focus and astigmatism corrections were achieved either by automatic functions or manually. With the deflection measurement of fields and subfields, the electron beam scanned uniformly both at the center and around the edge. Although three different electron beam detection modes were available (secondary electron, backscattered electron, absorbed electron), the secondary electron detection (SE) was normally used as image and detector reference.

Fig. 2-7 JEOL JBX-5500ZD EBL writer is located in High Density Electronics Center (HiDEC) at University of Arkansas, Fayetteville [43].

Fig. 2-8 shows the overall system software (Fig. 2-8 (a)) and sub-functions interfaces under Microsoft Windows XP system. The integrated CAD software is shown in Fig. 2-8 (b) which could also have been achieved through AutoCAD with a following file format conversion. Fig. 2-8 (c) is the beam calibration sub-function interface. The beam condition was calibrated through standard procedures including beam current measurement, beam size justification and deflection error evaluation that could not be achieved in NPGS system directly. Through a standard schedule file (Fig. 2-8 (d)) the patterns and exposure information were combined to generate the writing strategy files without detailed any movement plan requirement. However, the machine had its own maximum running speed that was related to DAC frequency, beam current, scan step and exposure dose.

$$t = \frac{s^2 \times D}{I^2} \tag{2.5}$$

$$F = \frac{I^2}{s^2 \times D} \leq F_M \tag{2.6}$$

The parameter t is the shot time during exposure. Parameter s is the assigned scan step. The required dose D is calculated by beam current and writing frequency. The parameter F_M is the allowed maximum frequency. The typical EBL exposure parameters using JEOL system were 50 kV acceleration voltage, 10 nm spot size, 5 nm scan step, 1 nA exposure current, 1 mm × 1mm writing field and objective aperture size 2.

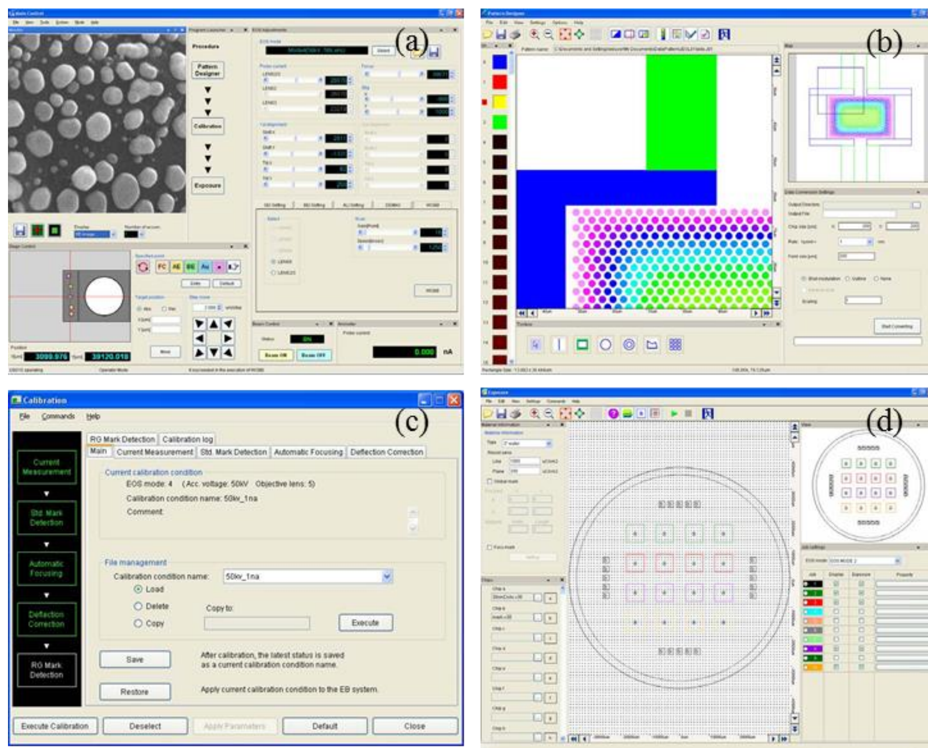

Fig. 2-8 JEOL JBX-5500ZD system software and sub-functions interfaces are shown [44].

2.3 Focused Ion Beam

FIB is a technique for pattern writing utilizing an ion beam scanned substrate instead of electrons in scanning electron microscope (SEM). It has been widely used in semiconductor industry, materials science and biology research. As shown in Fig. 2-9 Ga ions are utilized in most commercial FIB systems.

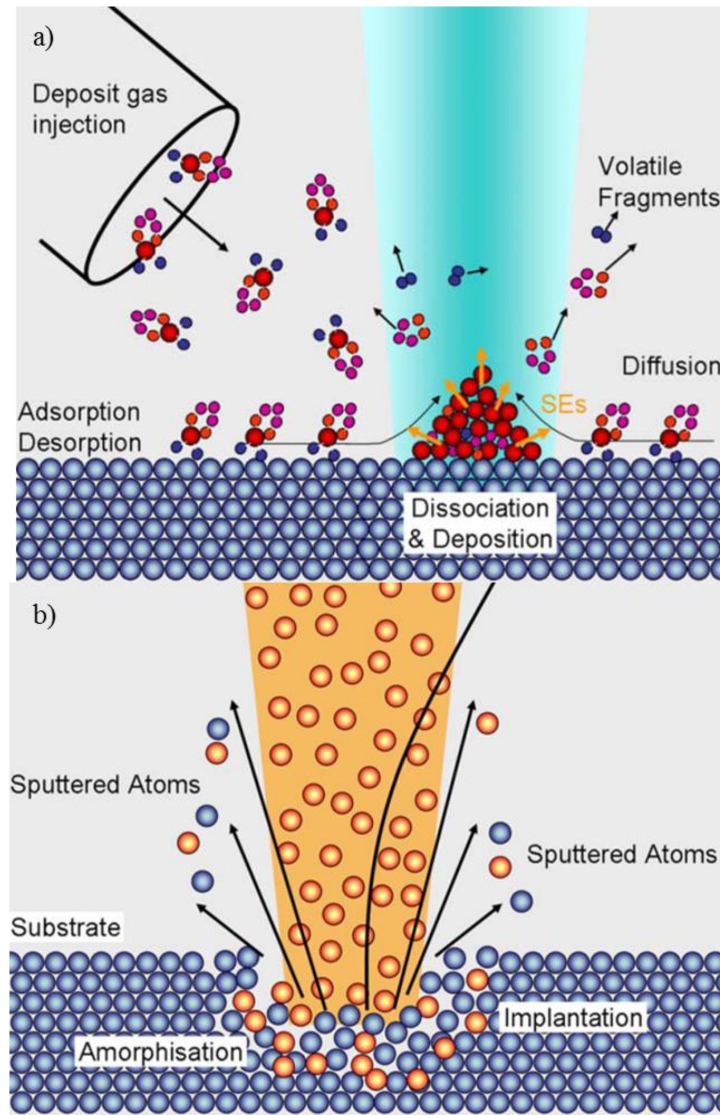

Fig. 2-9 Gas-assisted electron beam deposition (a) and focused ion etching mechanisms (b) are shown [45].

Generally, since the ions sizes are larger than electrons the microscopy resolution of FIB is lower than SEM. Besides this, when the high energy Ga ions hits the sample, the substrate material might be bombarded and sputtered from the surface. With the Ga ions sputtered properly, it provides a precise micromachining method with high geometry control. Combining with gas injection capabilities, the ion beam can also be used to assist deposition by decomposing the precursor gas into volatile and non-volatile components. Since there is no

mask needed, FIB is normally utilized as fast prototype fabrication tool. The ions will also be implanted into the substrate that might make the substrate surface amorphous. This really limits the application of FIB since a special surface treatment might be required, such as a protective passivation layer deposition before FIB operation. In this dissertation, the FEI Nova Nanolab 200 Dual-beam workstation was used that was located in the Arkansas Nano-Bio Materials Characterization Facility, which is affiliated with the Institute for Nanoscience and Engineering at University of Arkansas, Fayetteville.

The FEI Nova Nanolab 200 Dual-beam workstation system used for this dissertation integrates electrons and ions beam for micro machining and imaging functions [46]. The schematic drawing of the two beams position is shown in Fig. 2-10 (a). The electron beam column produced high quality microscopy images and assisted in depositing metals and dielectric layers on the sample surface. In this machine, Platinum (Pt) and Oxide were two available materials for deposition. In the high resolution mode, over 2500 kX magnification was achieved with 1 nm resolution. The ion beam tilted 45° was used as both etching and deposition tools that provided powerful and fast device prototype fabrication capabilities. To achieve Platinum (Pt) or Oxide layer deposition, the OmniProbe 100 nanomanipulator was integrated in the system. Through the conjunction of electron or ion beams, specific structure was patterned on surface. The advantage of electron beam assisted deposition was a uniform surface without the sputtering effects of ion assisted deposition.

For electron beam assisted deposition, as shown previous in Fig. 2-9 (a), the gas was introduced first above the target area hundreds of microns. With gas injection, the gas molecule was adsorbed at the sample surface. With the electron beam hit the surface, it generated secondary electrons that broke the chemical bonds of the adsorbed gas molecules into several

components: dissociated components that were volatile and deposited elements on the surface. However, as shown in Fig. 2-10 the deposited elements would have a higher chance to be bombarded away if no fresh gas was injected. A proper writing plan with well controlled beam was critical to an efficient FIB induced deposition system. The FIB assisted etching had a similar process as deposition (Fig. 2-9 (b)). The gas was introduced first above the target area hundreds of microns. With gas injection, the gas molecule reacted at the sample surface forming volatile and nonvolatile species. Instead of depositing the nonvolatile components, it was sputtered with evaporated volatile components. The beams operation and microscopies are shown in Fig. 2-10 (b) with control software interface.

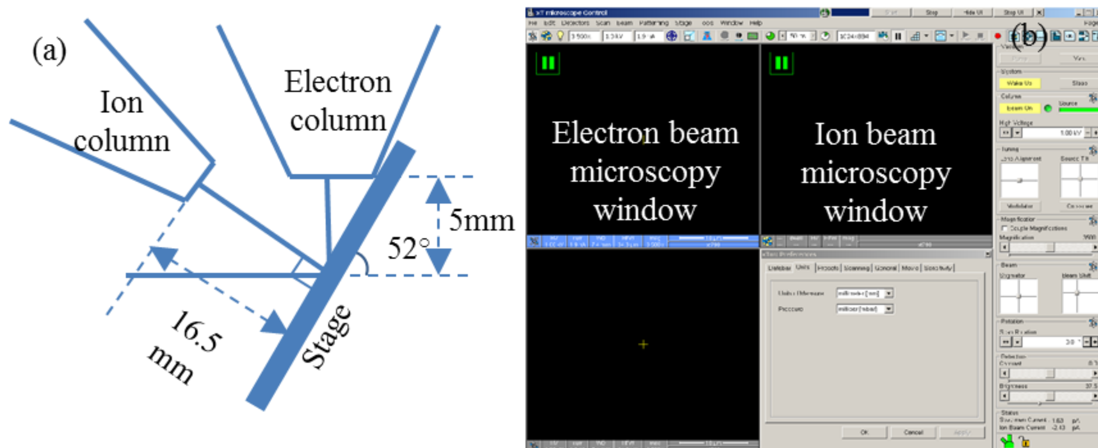

Fig. 2-10 The schematic drawing of FEI Nova Nanolab 200 Dual-beam workstation system configuration (a) is shown with control software interface (b) [46].

2.4 Metallic Nanostructures Fabrication on c-Si and ITO Substrates

The developed fabrication process using EBL to fabricate metallic nanostructures on c-Si has been presented previously in Fig. 2-1. The Si substrate was scribed to 1 cm × 1 cm size from 5 inch c-Si wafer, followed by a cleaning process using Acetone, Methanol and IPA. After rinsed in DI water, the sample was baked at 180°C for 10 minutes to dehydrate the substrate. 495K or 950K PMMA with concentrations of 2%-8% dissolved in Anisole was chosen as the

electron beam sensitive resist based on required pattern geometries. Different concentrations corresponded to certain film thickness as needed to be considered for further processing. Generally, the sample did not need special surface preparation before PMMA coating due to its excellent adhesion properties. After PMMA coating at certain speed, the sample was baked on a hot plate at 180°C for 2 minutes to evaporate solvents. The film thickness of typical 6% 950K PMMA dissolved in Anisole was calibrated with different spin speeds as shown in Fig. 2-11 (a). The thickness calibration results of several different PMMA concentrations at 3000 RPM are shown in Fig. 2-11 (b). In EBL exposure the typical exposure dose was chosen around 200-1200 $\mu C/cm^2$. Several specific cases will be discussed in this chapter. The standard developing process was sample immersion in mixed solution (MIBK: IPA=1:3) for 30-60 seconds followed by 15 seconds IPA rinse. The commercial mixed product from MicroChem was used in this case. The followed metal deposition was conducted using thermal evaporator. Typically 5nm Chromium (Cr) and 30nm Gold (Au) layers were deposited on the substrate. In the early processing development period, 10 nm Titanium (Ti) and 30 nm Au layers were used as metal combinations in the e-beam evaporator. After metal deposition, the sample was immersed in N-Methyl-2-pyrrolidone (NMP) based solvent stripper (PG remover from MicroChem) at 80°C to remove all resist, leaving the metal layers in the exposed area. The actual lift-off time varied based on different pattern geometries. Ultrasonic clean is optional for accelerating this process on Si and glass substrates. The final step was rinsing the sample with IPA and DI water.

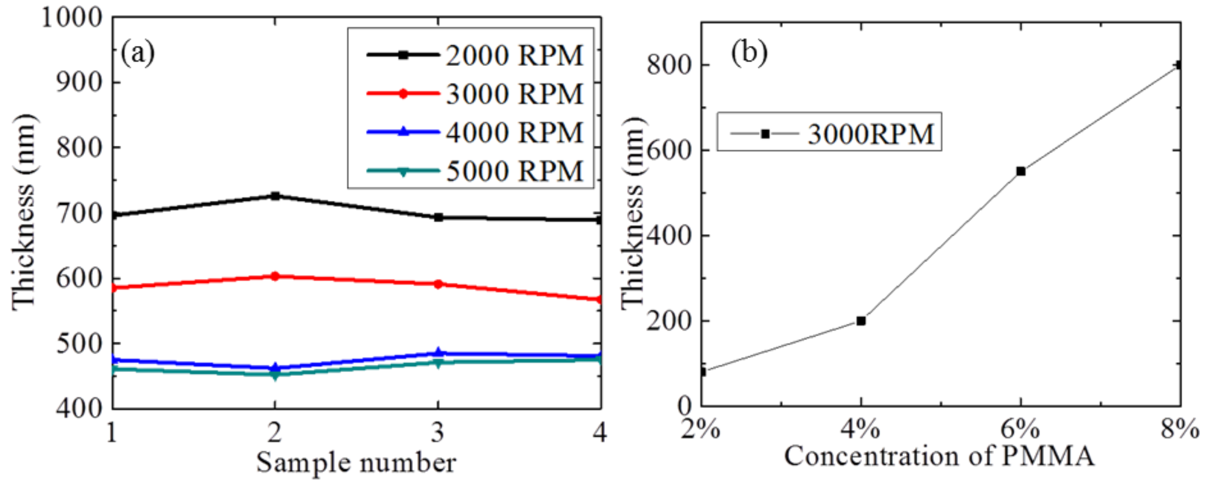

Fig. 2-11 The thickness of 6% 950K PMMA at different spin coating on 1 cm × 1 cm samples is shown in (a). The thicknesses at 3000 RPM of PMMA with various concentrations are shown in (b).

During early processing development, the processing yield was not quite high because the metal layer could not be fully lifted off. As shown in Fig. 2-12 (a), the metallic nanodisks were successfully deposited on c-Si substrates with surrounding areas clean. In contrast, the nanodisks with smaller spacing in Fig. 2-12 (b) could not be fully lifted off. The possible reasons were inaccurate electron dose, low thickness ratio between resist and metal layers, small spacing between patterns and other specific machine related problems.

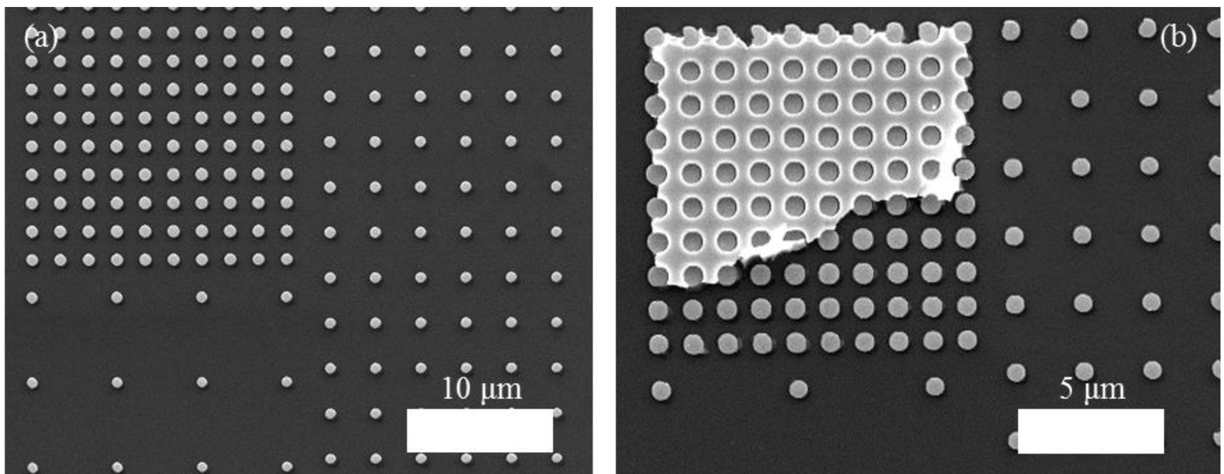

Fig. 2-12 The comparison between successful and unsuccessful lift-off results is shown with metallic nanodisks arrays.

Fig. 2-13 shows different situations during metal deposition. If the resist is underexposed by the electron beam, the edge at the metal layer might have a 30 degrees slope. With resist residual in the exposed area, the deposited metal layers in exposed and unexposed area might connect together with possible unsuccessful lift-off result [Fig. 2-13 (a)]. Even with the proper electron beam exposure, the thickness ratio between resist and metal layers needs to be carefully chosen due to the nonideal surface morphology. As shown in Fig. 2-13 (b) the actual corner of resist could be round shape instead of extremely sharp. If the resist is too thin or the deposited metal layer is too thick, the deposited metal could form a complete layer instead of disconnected patterns as shown in Fig. 2-13 (c). However, the edge slope after an optimized electron beam dose is nearly vertical comparing to underexposed condition shown in Fig. 2-13 (a). Successful lift-off results are achieved when the thickness ratio between resist and metal layers is larger than 3 to avoid the metal layer connection. Fig. 2-13 (d) shows an optimized condition of metal deposition which should succeed in a followed lift-off process. Beyond the possible conditions mentioned above, the pattern density was another factor under consideration. In Fig. 2-12 (b), the nanodisks array with larger spacing showed clear surrounding areas comparing to the array

with smaller spacing. With larger spacing, the stripper could dissolve resist better from different directions.

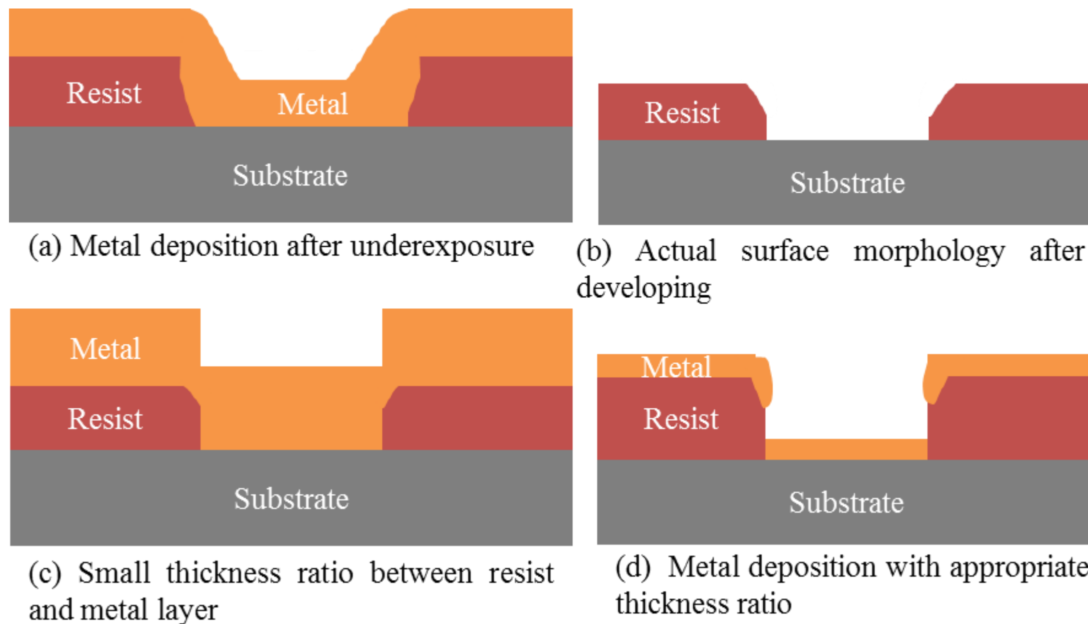

Fig. 2-13 The lift-off considerations in metallic nanostructures fabrication on c-Si substrates are shown with different fabrication results.

During the processing development, the problems mentioned above were solved based on recipe improvement. In other words, those problems were predictable. However, some other issues related to specific equipment were more difficult to solve. They showed similar fabrication results and behaviors as those discussed above. Fig. 2-14 (a) gives an example showing an unsuccessful lift-off result that was similar to Fig. 2-12 (b). The first assumption here was that a complete metal layer formed on top of the structures either by underexposure or small thickness ratios between resist and metal. After this, a thorough electron beam dose screening experiment with 10 times thicker resist obtained the same lift-off result (800 nm resist vs. 35 nm metals). After 15 nm metal layers deposition trials, the problem was found to be the metal deposition process using the Edwards 306 electron beam evaporator. A tentative solution found here was increasing the resist thickness to 1600 nm through a double spin technique in

which the same resist was spun twice on the sample to double the resist thickness. The fabrication results are shown in Fig. 2-14 (b). With this method, the metallic nanostructures were successfully patterned on c-Si substrates with resist residual existing in adjacent areas. However, the feature size was limited to 150 nm because of the too thick resist. The electron beam could not go through the entire thickness of resist without disturbance. In order to fabricate smaller patterns, Ti instead of Au was used as the deposition material. The fabrication result in Fig. 2-14 (c) shows a clear surrounding area of nanostructures. This also proved the problem was not from the well-developed EBL process but from other sources. During the e-beam evaporation, since deposition current was three times higher than published data, the metal atoms transferred heat to the resist during deposition. Because the working distance was only 20 cm, the accumulated heat could not dissipate during the limited deposition time. With the reduced current and longer working distance, this problem was solved as shown in Fig. 2-14 (d). For the device development work discussed later in this dissertation, thermal evaporation was mainly used as metal deposition method.

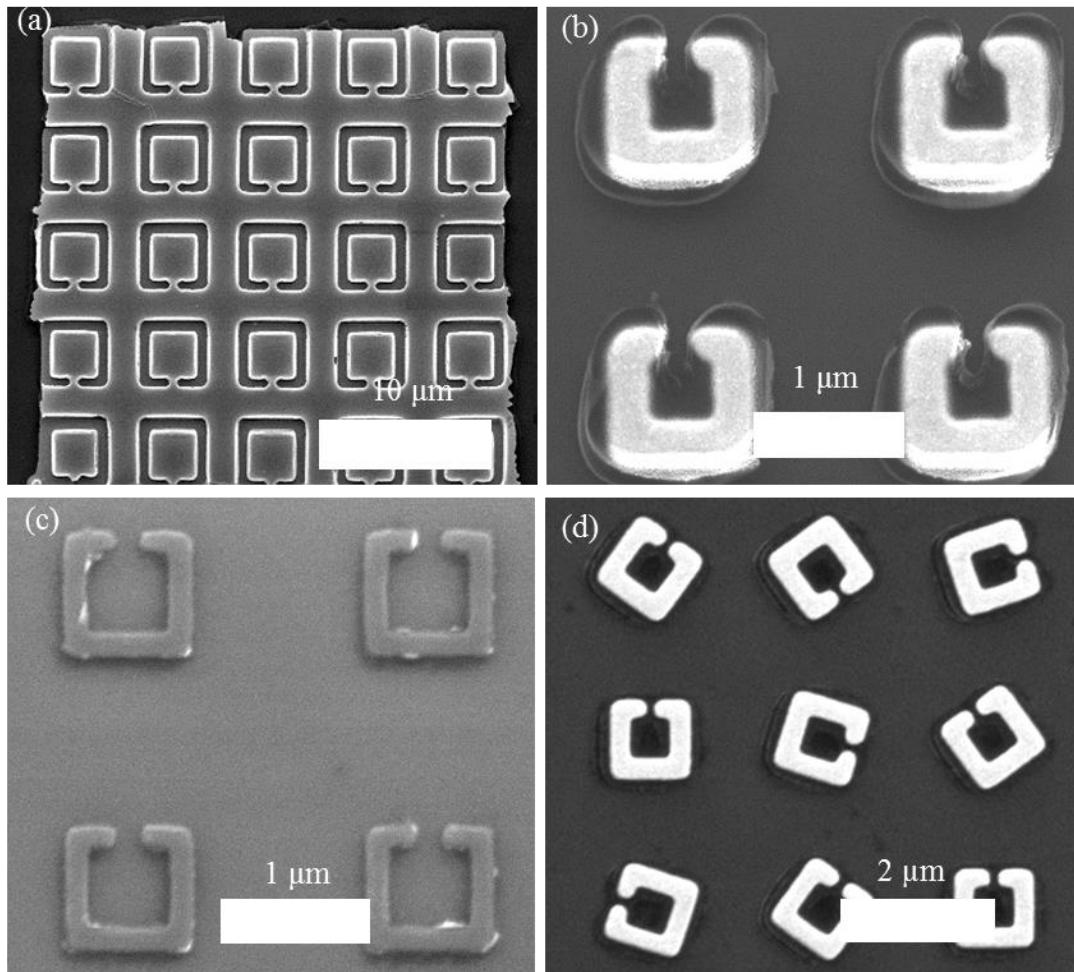

Fig. 2-14 Lift-off problem trouble shooting process is shown with results. Figure (a) shows the unsuccessful lift-off results of fabricated nanostructures. Figure (b) shows the lift-off result after double spinning of resist. The alternative metal Titanium instead of Gold was utilized for trouble shooting reason as shown in (c). Figure (d) presents the fabricated metallic nanostructures after process improvement.

Having the well-defined EBL working conditions, the trouble-shooting experiment to solve this lift-off issue is shown in Table 2-1 with experiment results.

No.	Resist information	Metal thickness(nm)	Deposition current (mA)	Deposition rate (nm/s)	Lift-off results
1	Single layer	5 nm Ti	30	0.05	Unsuccessful
		10 nm Au	125	0.01-0.02	
2.	Single layer	10 nm Ti	30	0.05	Unsuccessful
		30 nm Au	148	0.02	
3.	Single layer	40 nm Ti	35	0.1	OK
4.	Double spin	10 nm Ti	36	0.1	OK
		50 nm Au	79	0.08	
5.	Double spin	10 nm Ti	35	0.1	OK
		30 nm Au	122	0.07	

Table 2-1 The experiment design and results for lift-off trouble shooting are shown.

With the fully developed fabrication process, various metallic nanostructures were then fabricated on c-Si substrates. Fig. 2-15 (a) shows the SEM image of a fabricated nanorod array by the NPGS system with 150 nm width and 2 μm pitch size. The deposited metal layers were 10 nm Ti and 30 nm Au. It also shows a magnified single nanorod image. Fig. 2-15 (b) shows the fabricated nanorod array by the JEOL EBL system. The pattern size was 120nm width and 4 μm pitch size. The fabricated pattern array covered a 1 mm $\times$ 1 mm area shown as inset with 30 minutes writing time. The magnified single nanorod image is also presented.

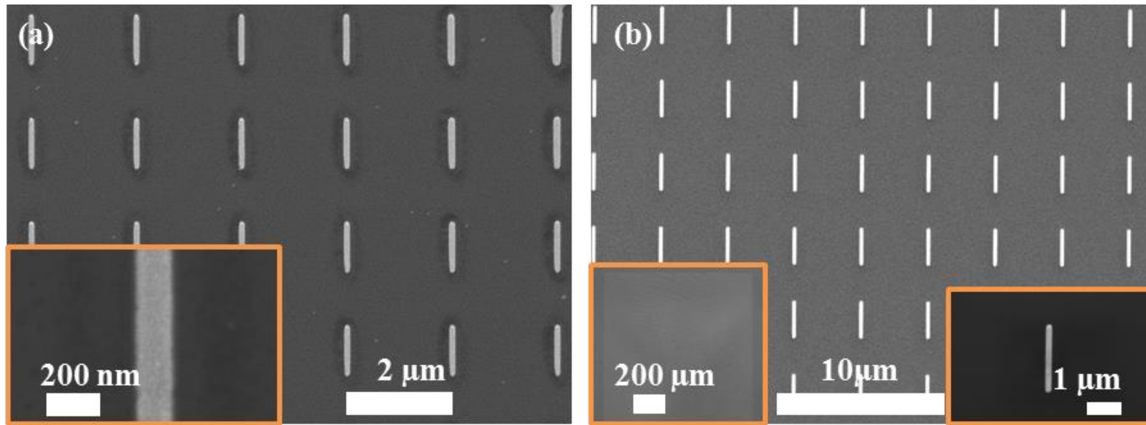

Fig. 2-15 The SEM images show fabricated nanorods array by NPGS (a) and JEOL (b) systems, respectively. The magnified single nanowire is shown. The fabricated patterns array covered 1 mm × 1 mm area shown in bottom left inset of (b). Bottom right inset shows a magnified single nanowire.

Fig. 2-16 (a) shows fabricated nanodisk array by the NPGS system. The diameter of disk was around 800nm with three different pitch sizes (2 µm, 4 µm and 6 µm). Fig. 2-16 (b) shows the fabricated split ring resonator (SRR) array by the JEOL EBL writer. The line width was around 200nm and the pitch size was 5 µm. The fabricated patterns array covered a 1 mm × 1 mm area as shown in the bottom left inset. Two separate SRRs are shown in the bottom right inset.

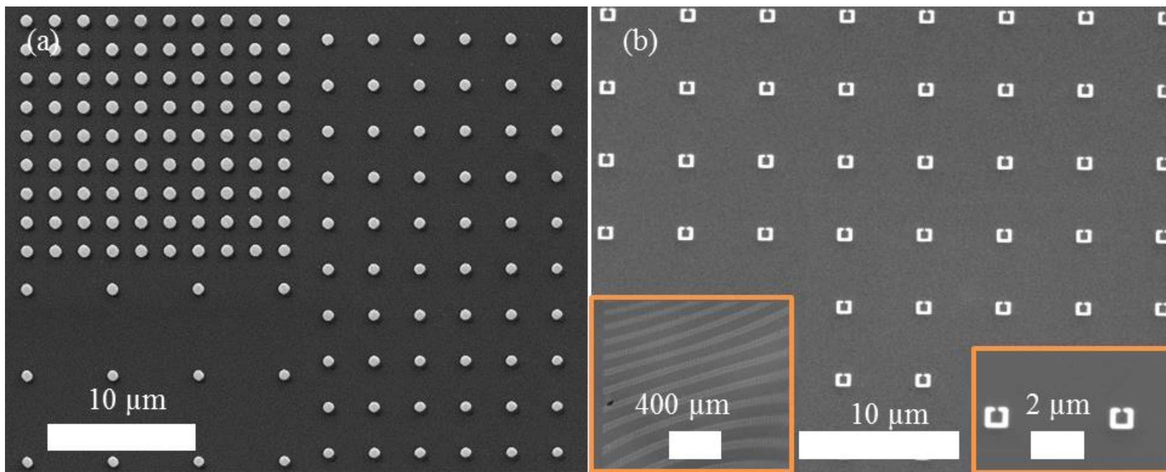

Fig. 2-16 The left image presents the fabricated nano disks array by NPGS system with different pitch size (diameter: 800 nm, 10 nm Ti and 30 nm Au). The right image presents fabricated SRRs array by JEOL system (200nm line width, 5 µm pitch size, 10 nm Cr and 30 nm Au). The fabricated patterns array covered 1 mm $\times$ 1 mm area (bottom left inset). Bottom right inset shows two magnified SRRs.

The images included in Fig. 2-17 (a) show the fabricated random SRRs array by the NPGS system with 150nm line width and 1 µm spacing. The 8 $\times$ 10 array of the SRRs is also presented as an inset. Each array covered 20 µm $\times$ 20 µm with 25 µm period distance. The bottom right inset shows a magnified SRR structure. Fig. 2-17 (b) presents the fabricated regular SRR pairs array by the JEOL EBL system. The achieved minimized spacing was around 40nm deposited with 10 nm Cr and 30 nm Au.

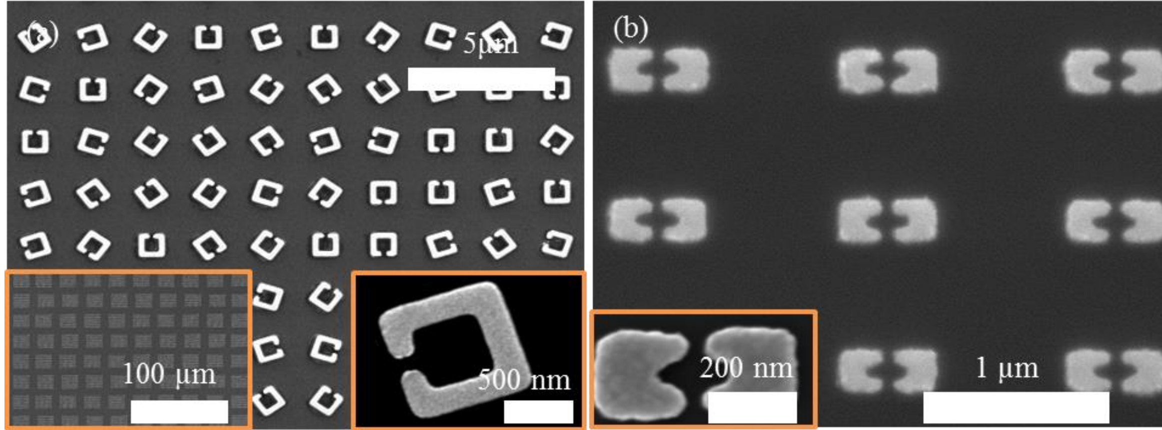

Fig. 2-17 (a) is the fabricated 8 × 10 random SRRs arrays by NPGS system. The geometry parameters were 150nm line width and 2 μm pitch size deposited with 10 nm Cr and 30 nm Au. Overall fabricated patterns array is shown in bottom left inset. Bottom right inset shows a magnified random SRR. Fig. 2-17 (b) shows the SEM image of fabricated SRR pairs array by JEOL system (40 nm gap, 1.5 μm pitch size, 10 nm Cr and 30 nm Au).

A 2D connected fishnet structure was proposed as an optimized light trapping structures for solar cells mainly due to the surface plasmonic propagation and connectivity of metallic lines as carrier transport path [47]. The detailed device development will be discussed in chapter 3. In order to integrate metallic fishnet structures on light detection devices, this structure was first developed on a c-Si substrate with various geometry parameters. Fig. 2-18 shows the fabricated fishnet structure with different sizes by the JEOL EBL writer. The metals were 10 nm Cr and 30 nm Au. The ratio of line width and spacing was 1 from (a) to (c). With decreasing line width, the corners of fishnet patterns became smoother with a round shape which could have been caused by proximity effects. It was clear from the images that the geometry parameters at the corner of the structure were more difficult to control. With 150nm width and 150nm spacing (Fig. 2-18 (c)), the corner could not form a right angle anymore, which meant more detailed process control should be considered. Further dose investigation combined with other parameter adjustments was required. In Fig. 2-18 (d), the fabricated fishnet line width is 100 nm with 1 μm

pitch size which will be used as light trapping structure for Schottky contact amorphous silicon (a-Si) solar cell.

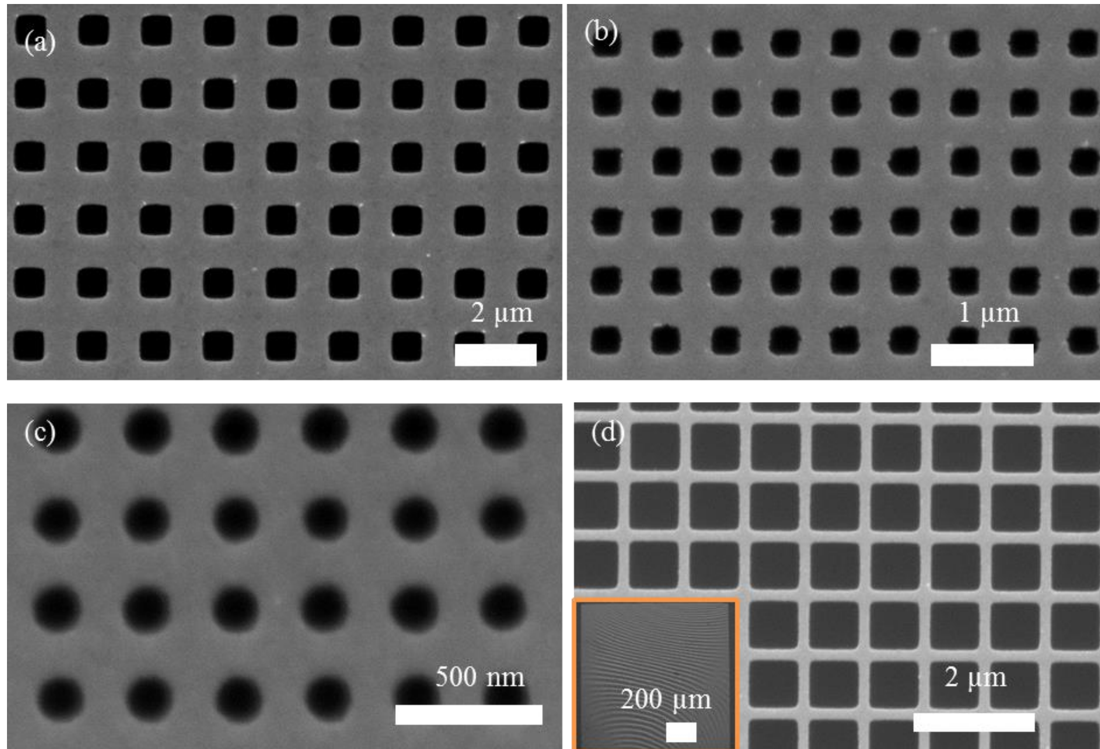

Fig. 2-18 The fishnet patterns with various sizes are fabricated on c-Si substrate. The geometry parameters of fabricated structures were: (a) 800 nm line width and 1.6 μm pitch size; (b)300 nm width and 1 μm pitch size; (c) 150 nm line width and 300 nm pitch size; (d) 100 nm width and 1 μm pitch size.

The detailed geometry parameters and EBL doses are summarized in Table 2-2. The summarized optimized EBL parameters provided a general guideline for fishnet patterning with various geometries.

Line width (nm)	Pitch size (nm)	Proper dose (μC/cm^2)
150	300	400-475
200	400	375-450
300	600	300-350
500	1000	220-280
800	1600	220-280
100	1000	520-560

Table. 2-2 The summary of EBL dose calibration is presented with various geometry parameters of fishnet structures.

In order to pattern metallic nanostructures on real optoelectronic devices, the process development in this dissertation took one more step in fabricating metallic nanostructures on transparent and conductive Indium Tin Oxide (ITO) that is normally used as electrodes. The substrates were purchased from Delta Technologies, LTD. The nominal ITO thickness was 15 nm – 30 nm with sheet resistance around 100 Ω/sq deposited on a glass substrate The surface roughness was below 20 nm with a 5 mm peak to peak measurement. Fig. 2-19 shows the fabricated Spit Ring Resonators (SRRs) and nanorods structures on ITO coated glass substrates. The fabricated SRRs array covered a 1 mm × 1 mm area with 2 μm pitch size as shown in the bottom left inset. The nanorods are around 1 μm long and 120nm width.

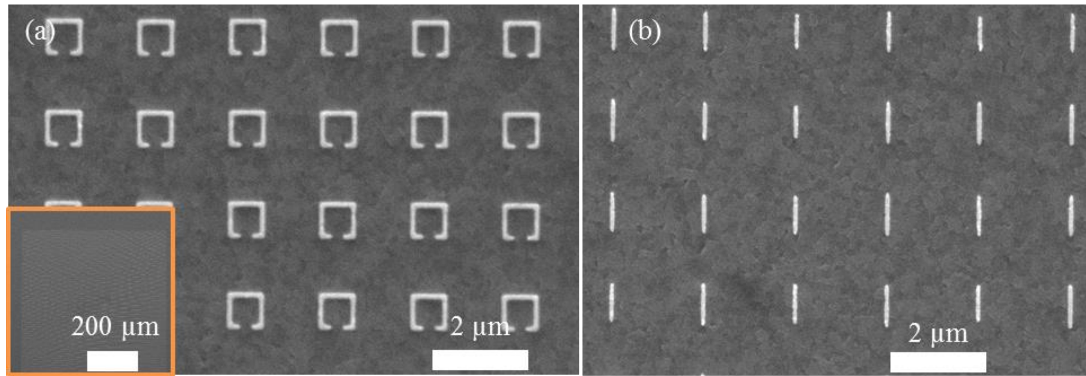

Fig. 2-19 The fabricated SRRs array were patterned on ITO covering a 600 μm × 600 μm area shown in (a). The nanorods were deposited on ITO of 100nm width and 1 μm length covering 500 μm × 500 μm area shown in (b).

Table 2-3 summarizes the achieved minimum feature size of various patterns on c-Si and ITO substrates by EBL. Moreover, the developed recipes were also evaluated to fabricate at relative large area which is necessary for following optoelectronic device applications. These results are meaningful as the start point to transfer the fabrication process to other real device substrates such as glass and a-Si.

Pattern	Feature size and area
Nanorods	100 nm line width, 2 μm length, 1 μm pitch size, 1 mm × 1 mm area
Nanodisks	200 nm diameter, 1 μm pitch size, 500 μm × 500 μm area
SRRs	100 nm line width, 1 μm pitch size, 1 mm × 1 mm area
Fishnet	100 nm line width, 200 nm pitch size, 1 mm × 1 mm area
SRR pairs	40 nm gap, 100 nm line width, 1 μm pitch size

Table 2-3 The achieved minimum feature size with covered area of different patterns is summarized.

In order to evaluate the best performance of the JOEL JBX-5500ZD EBL writer with large area writing capability, two set of experiments were carried out with different purposes. The first was the SRR pair pattern on glass substrates with various length and gap geometries. The CAD design is shown in Fig. 2-20, with the length of the SRR long arm changing from 120

nm to 180 nm and the gap from 20 nm to 160 nm (both with a step of 20 nm). So there were 4 × 8 arrays with 200 μm pitch size covering a 800 μm × 1600 μm area. The detailed process was the EBL exposure of metallic nanostructures on glass substrate followed by metal depositions (2 nm Cr and 30 nm Au) and lift-off. The other geometry parameters are shown in Fig. 2-20 as well.

The SEM and AFM results of the smallest gap value at 20 nm with 140 nm length are shown in Fig. 2-21 (a) and (b). The dark shadow area between SRR pair on the SEM image is due to a known ESEM low vacuum artifact. With a 45 degree rotation from the horizontal position, the SEM and AFM results of largest gap value at 160 nm with 160 nm length are shown in Fig. 2-21 (c) and (d). The shadowing area shown in SEM image was confirmed through AFM results that it is a SEM imaging artifact, not a real feature on the substrate. The surface roughness was around 5 nm due to the much slower metal deposition rate.

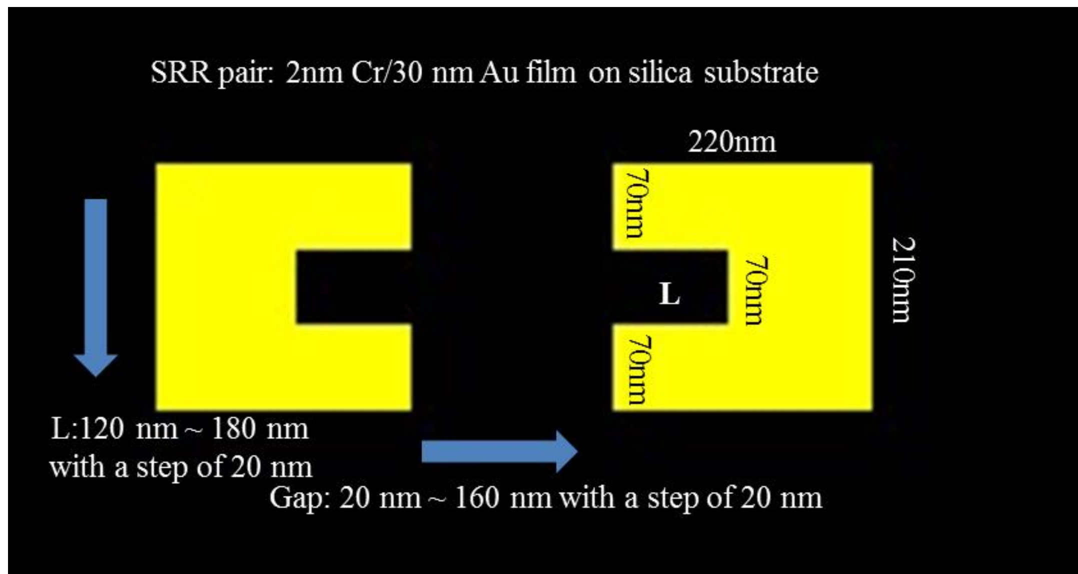

Fig. 2-20 The CAD design of SRR pairs array is shown. For each gap and L value variations, the 50 × 50 SRR pairs array locates with the period of 1.2 um by 0.8 um in horizontal and vertical directions between each pair. There are 8 arrays in horizontal and 4 arrays in vertical in total.

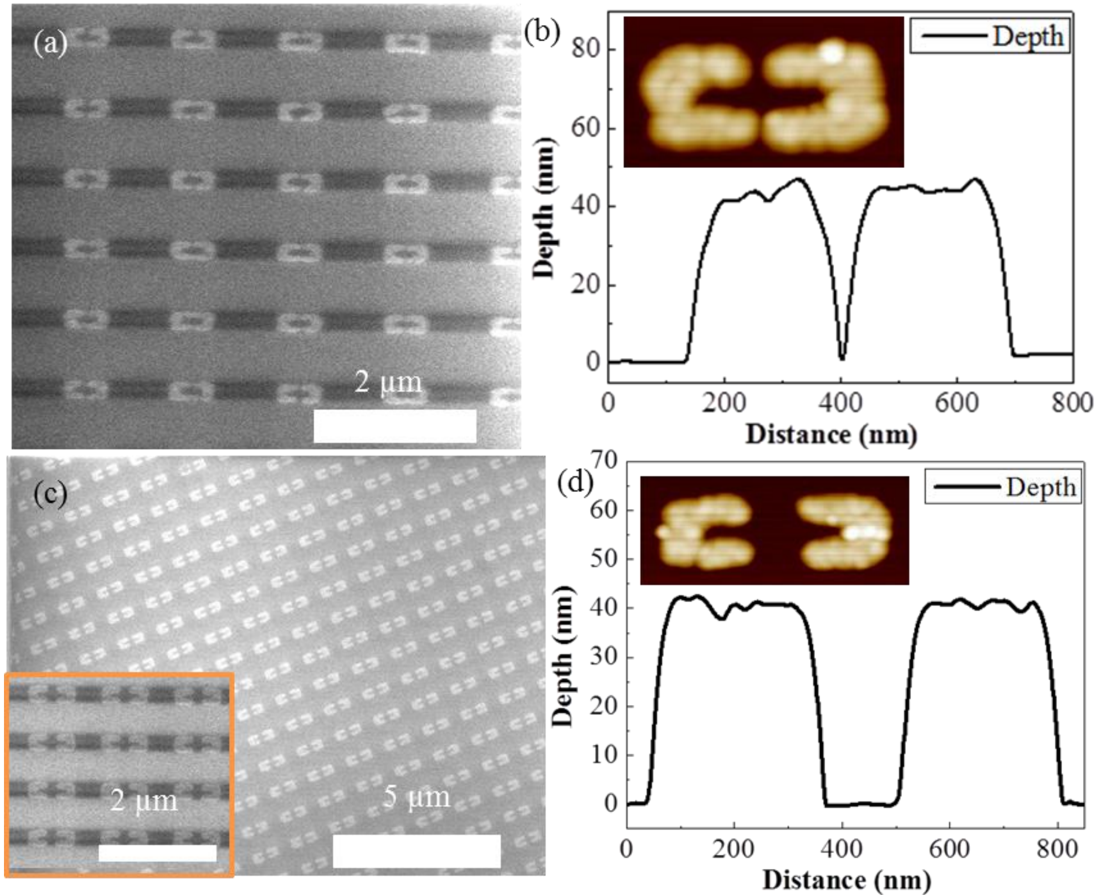

Fig. 2-21 The SEM and AFM results of two gap values (20nm and 160 nm) of SRR pairs are presented.

Other than the minimum gap test, the smallest line width exposure on c-Si was used for the second minimum feature evaluation experiment. As shown in Fig. 2-22 (a), the CAD design used was a straight line instead of a normal rectangle pattern. Instead of the electron beam scanning back and forth generating the pattern, the beam in the minimum gap test only scanned one time forming a line. Theoretically, the electron beam spot size was the limit of the minimum line width. However, the actual metal line width could be much larger because of the writing dwell time, beam calibration condition, resist properties, developing time, metal thickness and lift-off conditions. The writing dwell time was the only variable in this series experiment. Other parameters were set based on the current best known experiment condition. The beam current

was controlled at 100 pA under the 4 lens mode. 2% 495K PMMA was coated at 3000 RPM with 80 nm thickness. The developing time was 60s with 15s IPA rinse and the metal was chosen around 25 nm thick. Fig. 2-22 (b) to (d) shows the line widths changing from 40 nm to 70 nm with different electron beam dose.

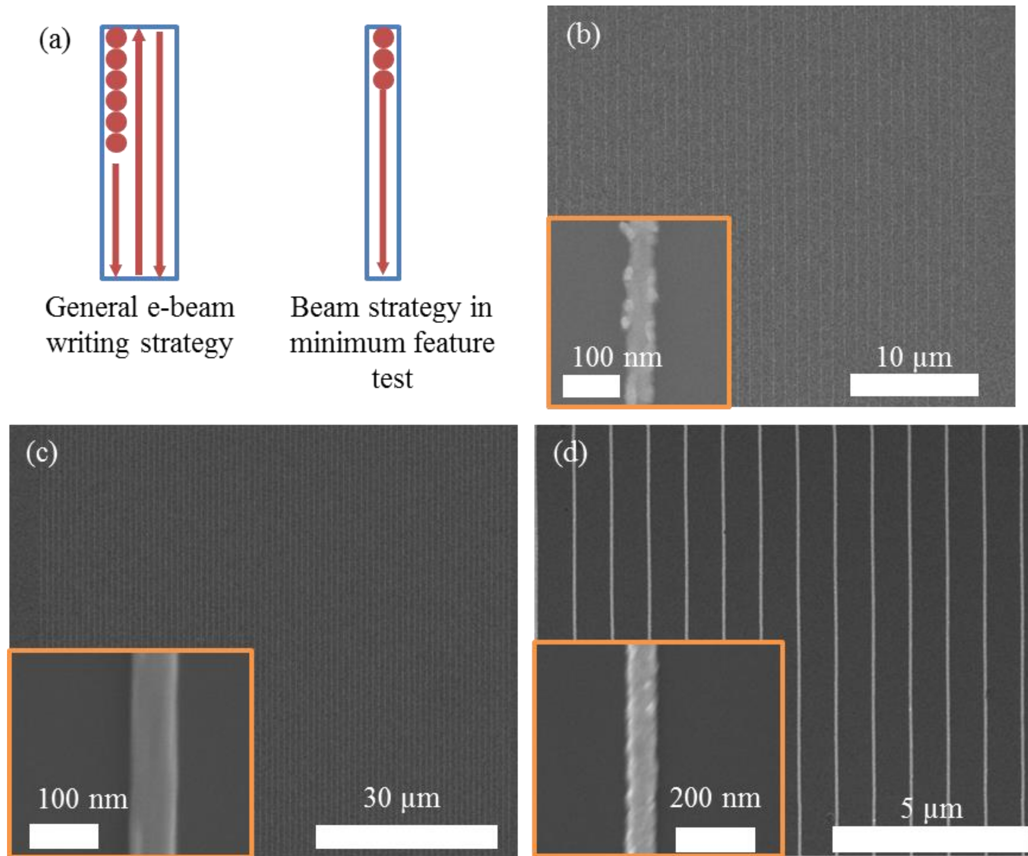

Fig. 2-22 The schematic CAD design and SEM results of EBL minimum line width test are presented. The achieved metal line width was 45 nm (b), 65 nm (c) and 70 nm (d).

Fig. 2-23 shows the summary of required doses to achieve different line width of metal grating structures. With increased dose from 5000 $\mu C/cm^2$ to 9000 $\mu C/cm^2$, the measured metal line width increases from 40 nm to 70 nm.

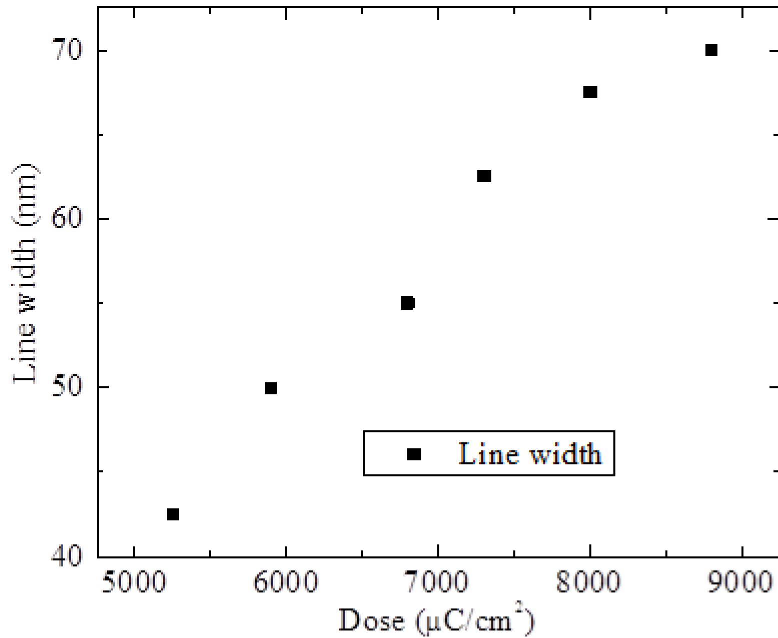

Fig. 2-23 The measured fabricated line width was larger with increased electron beam dose.

2.5 Metallic Nanostructures Fabrication on Glass Substrates

Previous developed processes of fabricating metallic nanostructures on c-Si and ITO coated glass were the preliminary steps to develop plasmonic enhanced optoelectronic devices. In order to investigate the detailed electrical and optical properties of fabricated structures and devices, those structures needed to be patterned on insulating or transparent substrates. Therefore, the EBL fabrication processes on glass (quartz) substrates were developed. The processing flow is shown in Fig. 2-24. Comparing it to the fabrication process on c-Si substrates, a thin film Chromium (Cr) around 5nm thick was deposited as the anti-charging layer on top of e-beam resist before exposure. The accelerated high energy electrons passed through the Cr and resist layers during exposure, and finally were neutralized from Cr layer. The Cr layer was removed after immersed in Cr etchant CEP-200 from Microchrome followed by standard developing, metal deposition and lift-off processes.

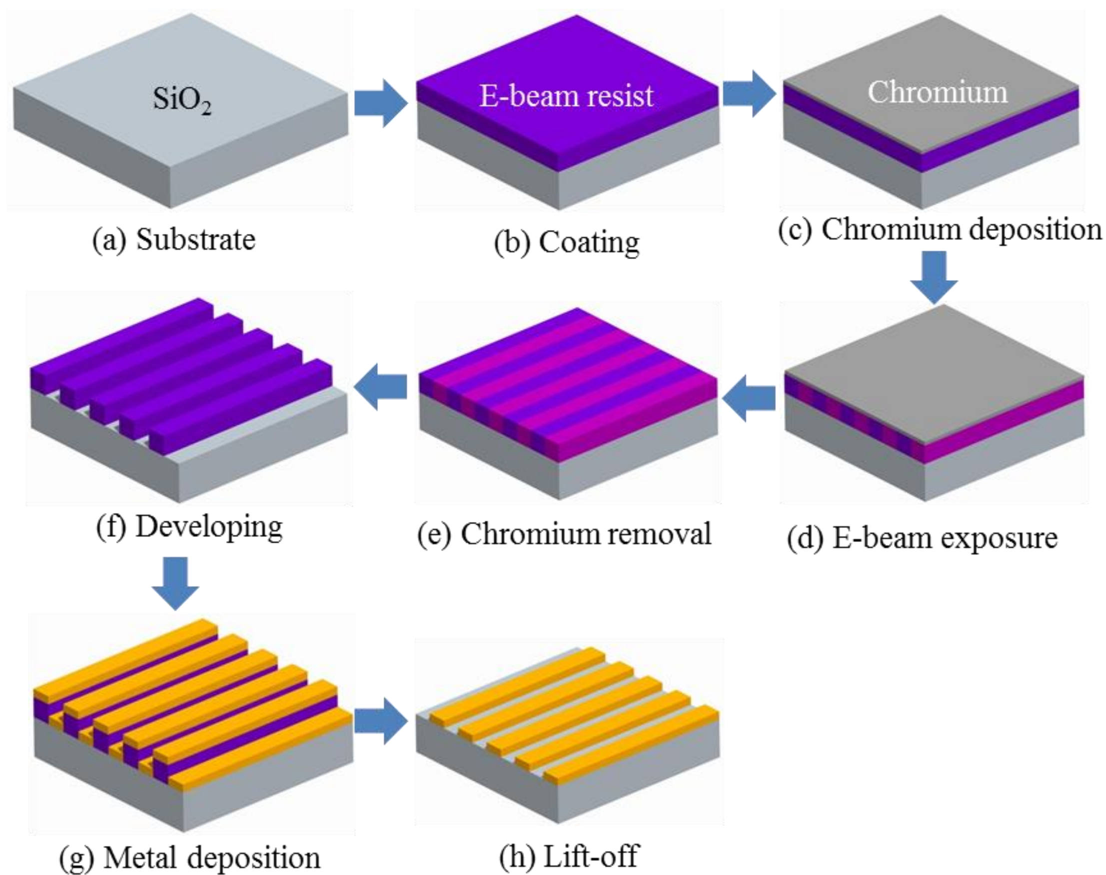

Fig. 2-24 The schematic drawing shows the standard EBL processing flow to fabricate metallic nanostructures on SiO_2 or glass substrates.

Specific techniques were utilized for glass sample morphology images. As shown in Fig. 2-25, during high vacuum SEM analysis the sample is irradiated with an electron beam it will cause static electric charge accumulation on the insulating glass substrates. This static charge will dramatically decrease the image quality as shown in Fig. 2-24 (a). Since the conventional SEM image acquisition is not suitable to glass substrates due to the charging effect, a special treatment needed to be considered such as conductive coating, low acceleration voltage, low vacuum, etc. The surface coating was the relatively straight-forward method. With a coated thin conductive layer, the accumulated electrons were released to ground resulting in better image quality. However, the sample could not be used for further characterization. In this case, the nondestructive method was preferred in which the low vacuum mode of the FEI XL-30

Environmental SEM was used with water vapor gas as the imaging gas (Fig. 2-25 (b)). The electron gun and vacuum were very sensitive to impurities including water vapor. To achieve a low vacuum mode for glass samples, the specimen chamber was isolated with the electron gun column (light blue area). One specific designed structure of 500 μm pinhole and four pressure limiting apertures (PLA) around were utilized to maintain the vacuum level difference (dark blue area). The high vacuum condition kept in the electron gun column and the relatively low vacuum was in the specimen chamber due to water vapor. To acquire the generated electrons for imaging, the gaseous secondary electron detector (GSED) was chosen with a hole in the center as the final aperture for primary electrons to pass through. Although the chamber pressure could be 10 Torr for a 500 μm aperture, a much lower pressure was chosen practically because of the limited electron mean free path. Once water vapor was introduced into chamber, the generated secondary electrons were released from the surface of sample and hit the water molecules, generating more secondary electrons. With increased collisions between water molecules secondary electrons accumulated and finally were collected by the GSED. With 600V positive bias of GSED, the ionized water molecules were driven to the sample surface neutralizing the negative charges from the primary beam.

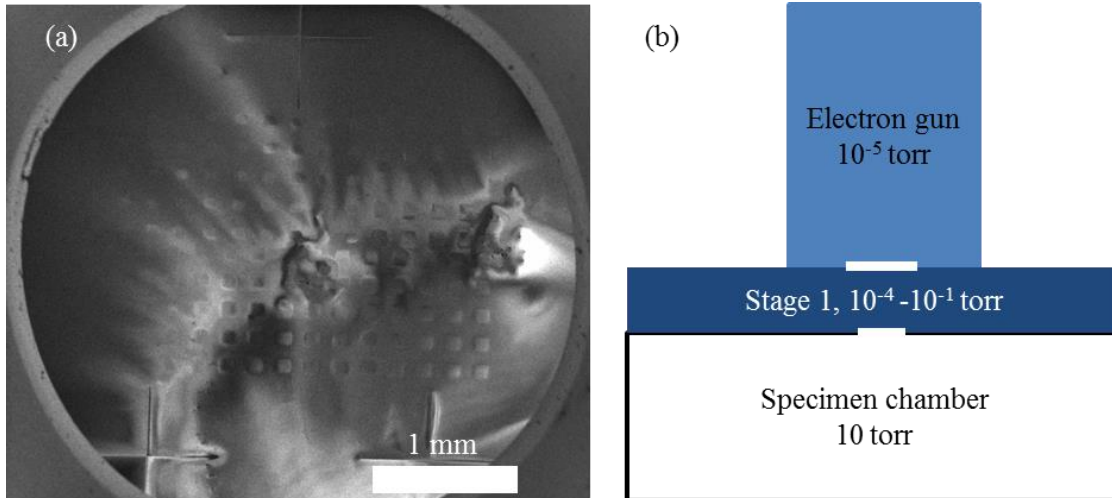

Fig. 2-25 The charging effect on glass substrate is shown in (a). The brief schematic drawing of ESEM machine with various vacuum levels is presented with colors in (b).

Fig. 2-26 shows the fabricated nanostructures on glass substrates. The fabricated nanorings array was imaged in the low vacuum mode of the ESEM. The line width was around 100nm with pitch size of 1 μm. The inner diameter (ID) was 200 nm. The bottom left inset showed the covered large area and bottom right one showed the single ring structures. Fig. 2-26 (b) shows the fabricated nanorods array with 2 μm length and 4 μm pitch size. The fishnet structure (Fig. 2-25 (c)) was patterned covering 50 μm × 50 μm with 1 μm spacing and 120 nm line width. The typical interdigitated structure patterned on a glass substrate was shown in (d). The 200 nm gap with 4 μm finger width was achieved with a 10 nm Cr and 100 nm Au deposition. The whole pattern covered a 800 μm × 500 μm area.

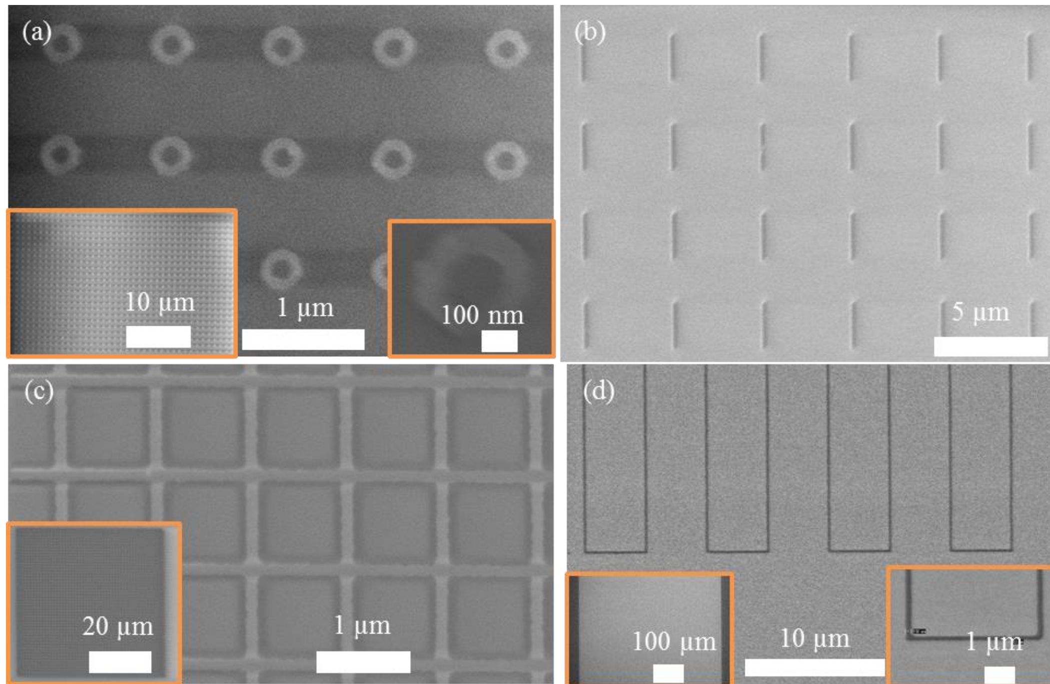

Fig. 2-26 Various metallic nanostructures were patterned on glass substrates. Fig (a) shows the fabricated nanorings with 200nm inner diameter and 300nm outer diameter. Fig (b) presents the nanorods with 2 µm length and 4 µm pitch size. Fig. (c) is the fishnet structure of 120nm width and 1 µm pitch size. Fig. (d) captures the interdigitated electrodes of 200nm spacing and 4 µm finger width.

2.6 Nanostructures Patterning of c-Si by EBL and FIB

Compared to patterning metallic nanostructures on top of various substrates, the patterning of c-Si was focused on the applications of Si photonic and nanophotonic devices. The EBL followed by dry etching and FIB are two methods used in this dissertation for patterning on c-Si. The fabrication processes of nanostructures on c-Si by both of these two methods were developed. The general work mechanism of FIB has been explained in the introduction of this chapter. Fig. 2-27 shows the detailed EBL process integrating with reactive ion etching (RIE) as the following process after EBL exposure instead of metal deposition and lift-off processes.

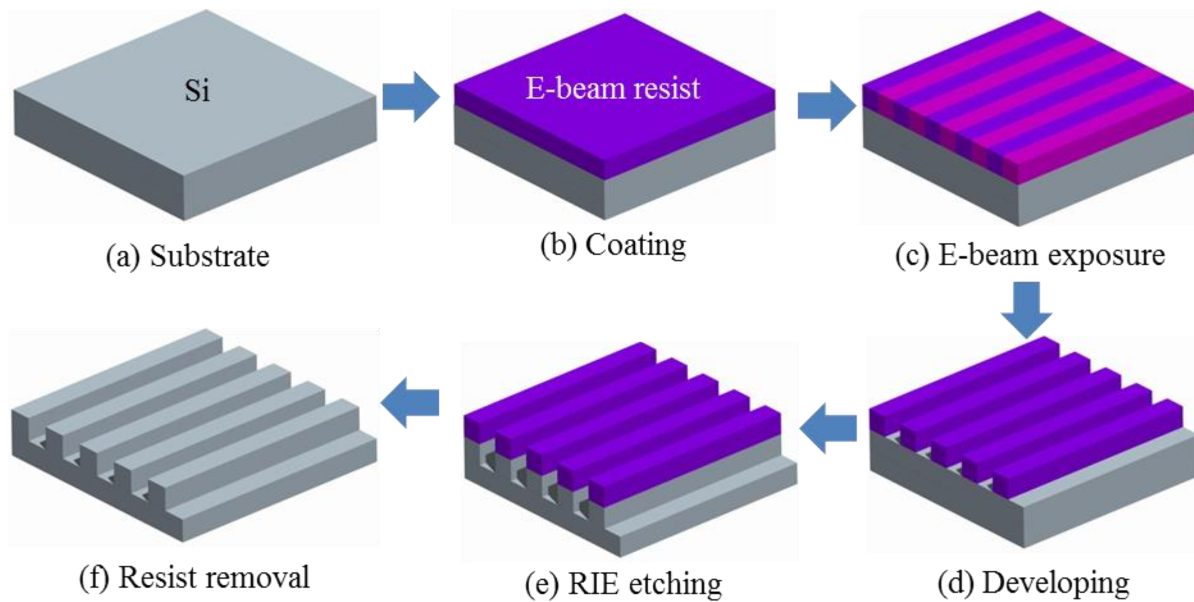

Fig. 2-27 EBL processing flow to fabricate nanostructures on c-Si substrates

Surface Technology Systems Advanced Silicon Etcher (Fig. 2-28 (a)) was used as RIE tool to fabricate nanostructures on c-Si. As mentioned in Chapter 2.1, ZEP-520 was chosen as the resist due to the 10 times better etching resistance than PMMA series resists. The sulphur hexafluoride (SF_6) was used as etchant to selectively remove silicon, with oxygen (O_2) acting as a catalyst. The 100:1 aspect ratio could be achieved by alternating the etch cycles with passivation cycles. Fig. 2-28 (b) and (c) show the 45 degree tilted SEM images of etched fishnet and align marker structures. The gratings structures are shown in (d).

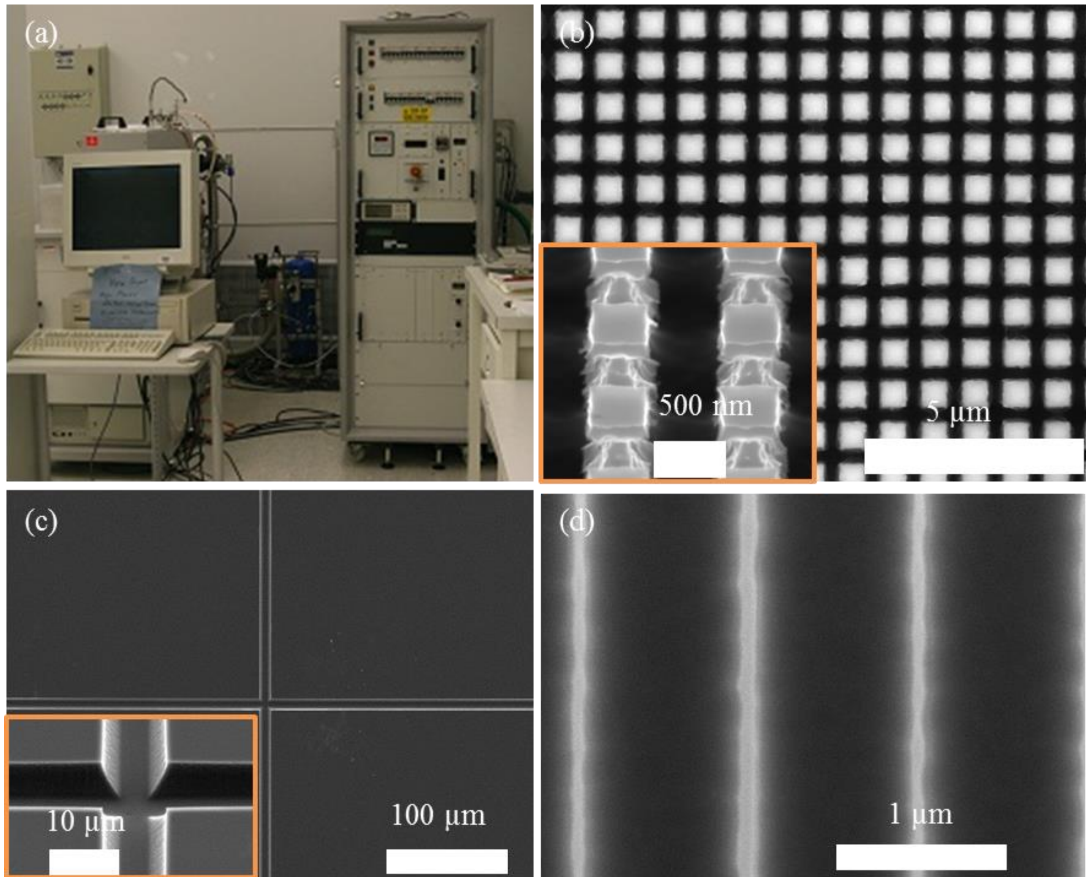

Fig. 2-28 Nanostructures patterning results on c-Si substrates are presented with the RIE machine shown in (a) from ref. [48]. The tentative etching results are shown from (b) to (d).

The summarized etch rate study of RIE by different parameter sets are shown in Table 2-4. With higher applied Coilpower, the etch rate is larger which sacrificed the pattern quality.

Gas flow (sccm)		**Coilpower (W)**	**Platepower (W)**	**Time (s)**	**Etch rate (µm/min)**
SF_6	O_2				
130	13	650	12	60	1.0
20	12	600	20	60	3.1
130	13	120	12	60	0.4
20	13	200	3	60	2.0

Table 2-4 The RIE processing parameters for nanostructures patterning on c-Si are summarized.

The FIB assisted deposition and etching results were investigated over various parameters including acceleration voltage, electron beam current, required minimum feature size and pattern pixel size. With higher voltage and lower current, the best processing resolution was achieved. With the FEI Nova Nanolab 200 Dual-beam workstation system, the pattern was designed using a 24-bit bitmap format. The pixel ranges were from 0 to 4095 in the x direction and from 280 to 3816 in the y direction. Each pixel consisted of red, green and blue colors shown in Table 2-5 (red was not used in the system). Green was used to control the beam with value 0 as blanker. Blue determined the writing time per pixel. Value 0 meant the minimum time of 100 ns and value 255 corresponded to the maximum writing time allowed in the software. The values between these two numbers were linearly interpolated. Fig. 2-29 shows a typical bitmap pattern of writing a 2×2 separate fishnet array with maximum writing time.

Color	**Result**
RGB 0/0/0 – black	Beam is blanked
RGB 0/1/0	Beam is on, 100nm min dwell
RGB 0/1/255	Beam is on, Maximum dwell time
RGB 255/255/255 – white	Beam is on, Maximum dwell time

Table 2-5 The color setting of bitmap CAD files used in FIB patterning is summarized.

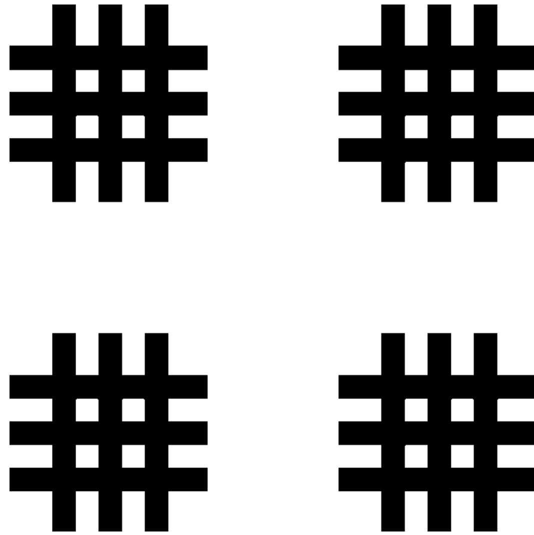

Fig. 2-29 The FIB pattern design of 2 $\times$ 2 separate fishnet array is presented with maximum writing time.

The FIB etching and deposition were finished using a proper bitmap design file. The detailed FIB assisted deposition and etching mechanisms have already been discussed in Chapter 2.2. Figure 2-30 (a) shows the Pt metal grating structures deposited using electron beam with minimum spacing of 50 nm. Since the blue color value from 0 to 255 in the RGB setting determined the real FIB writing time, each pixel was assigned a value with different etching depth based on writing time. The "steps" morphology is shown in Fig. 2-30 (b) with different dwell time. The inset shows the FIB bitmap CAD design leading to corresponded dwell time in actual FIB exposure. Fig. 2-30 (c) shows the FIB etching results of separate fishnet structures on c-Si with the line width at 250 nm. Fig. 2-30 (d) shows the calibration pattern to test the FIB etching quality of rectangles with different length-to-width ratio from 1:1 to 1:10. The etching depth was smaller (~300 nm) than the target value (1 μm).

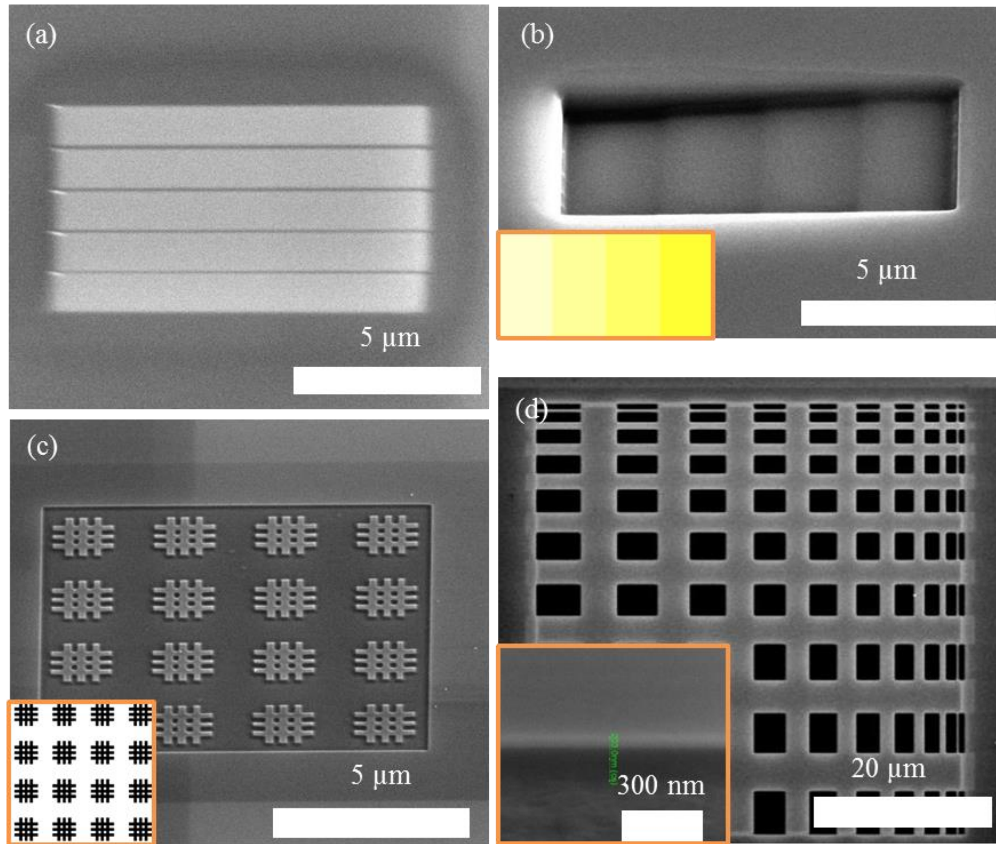

Figure 2-30 The results of electron beam assisted deposition and FIB assisted etching are presented.

To prepare for future device fabrication, a large area FIB etching test was necessary. Fig. 2-31 shows the etched fishnet structures covering a relatively large area of around 100 μm × 100 μm area. The fabricated line widths were 200 nm and 500 nm, respectively. The total writing time was kept under 30 minutes as that was a reasonable time for device prototype fabrication. The smaller line width (200 nm) was achieved with a smaller writing area (10 μm) as shown in Fig. 2-31 (a).

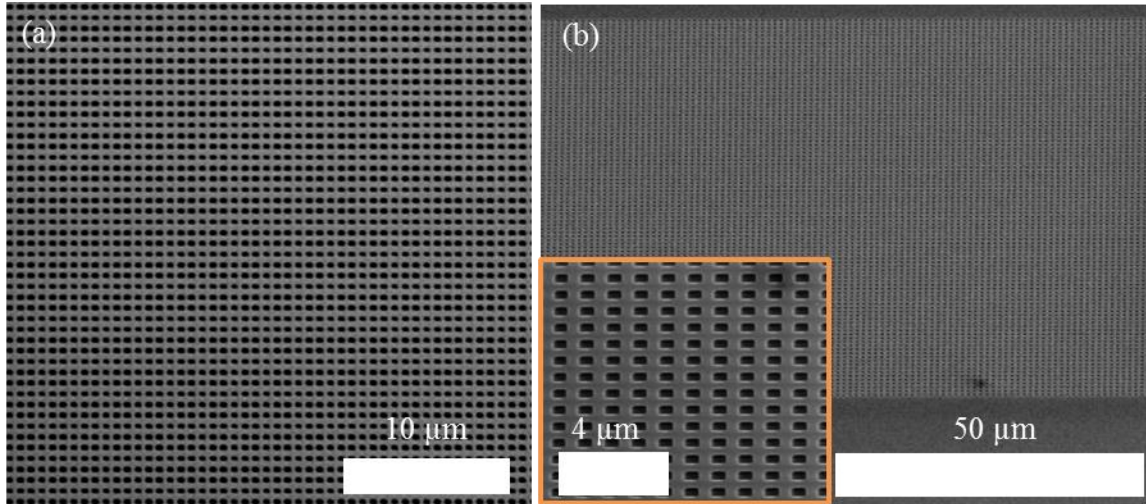

Fig. 2-31 Fabricated fishnet structures covered relative large area 100 μm × 100 μm within 30 minutes. The achieved line widths were 200nm (a) and 500 nm (b), respectively. The duty cycle was 1:1 ratio.

The FIB technique was initiated to develop the nanowire device by FIB assisted etching and electron beam assisted deposition. Fig. 2-32 (a) and (b) show nanowire devices on SiO_2. The global contacts were made of 10 nm Titanium (Ti) and 100 nm Gold (Au). In order to investigate the electronic and optical properties of a single nanowire, other deposited nanowires (marked with red boxes) were etched to be disconnected from electrodes. Fig. 2-32 (c) and (d) shows the corresponded SEM results after FIB assisted etching of nanowires from electrodes. The results show three nanowires disconnected in total by FIB assisted etching with single nanowire left for future characterization.

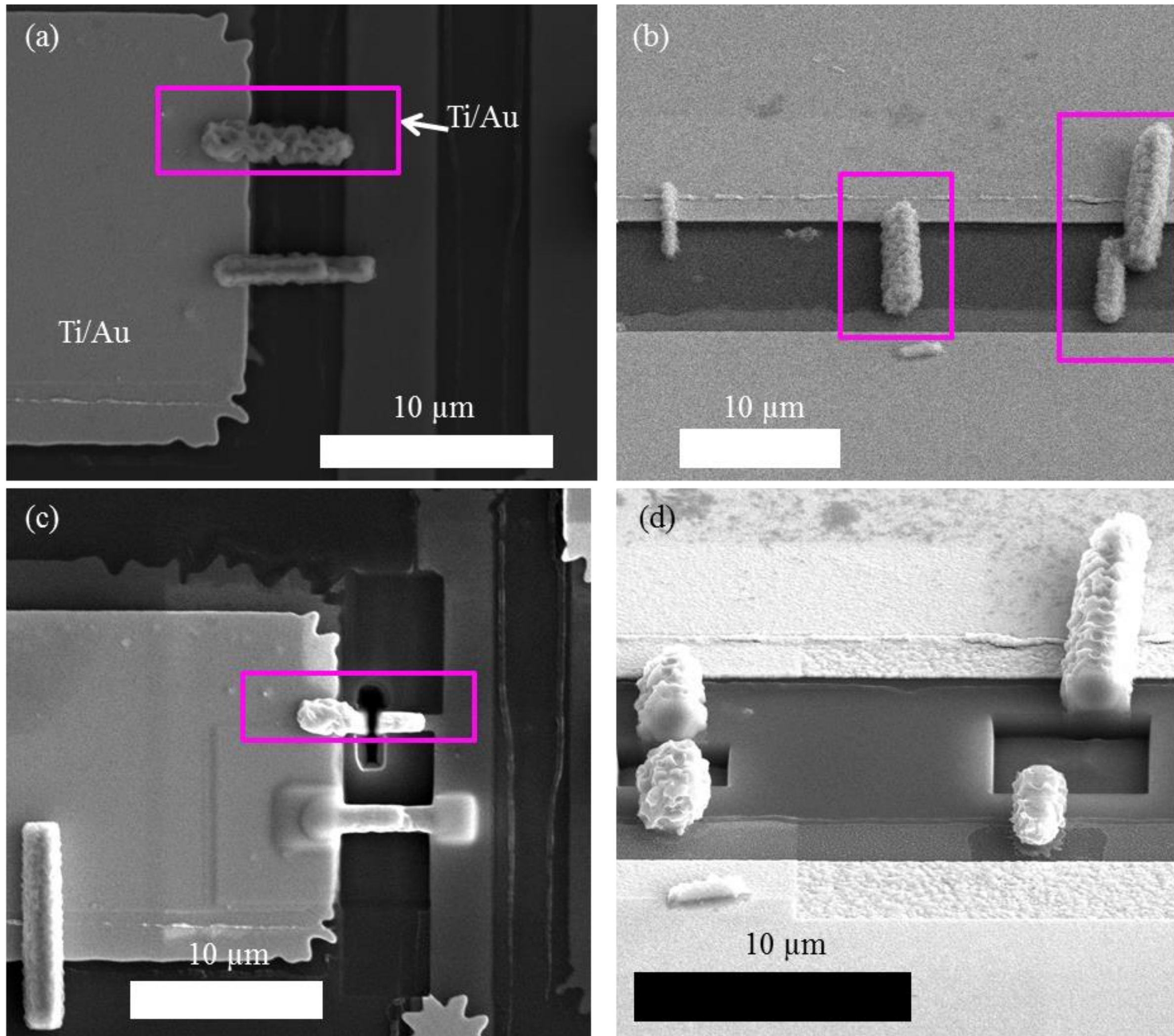

Fig. 2-32 The fabricated single nanowire device by FIB is presented with SEM images shown before and after etching. (a) and (b) show before etching condition of two positions on one nanowire device. (c) and (d) show the corresponded device positions after etching condition. The nanowire in yellow box was the target under test.

A FIB etching test on a thin film metal layer was carried out on Au (100 nm) covered c-Si samples. The fabrication results are presented in Fig. 2-33 (a) and (b). During the experiment the surface morphology changed after etching especially around the etched pattern edge. The possible reason for the amorphous surface was the unintended exposure under ion beam during image acquisition. Since Ga atoms reacted with Au atoms to form isolated islands of alloy, the etching process was carried out very carefully without any ion beam image. Through the

validation experiment, Fig. 2-33 (c) and (d) present the surface morphologies before and after one time ion beam scanning.

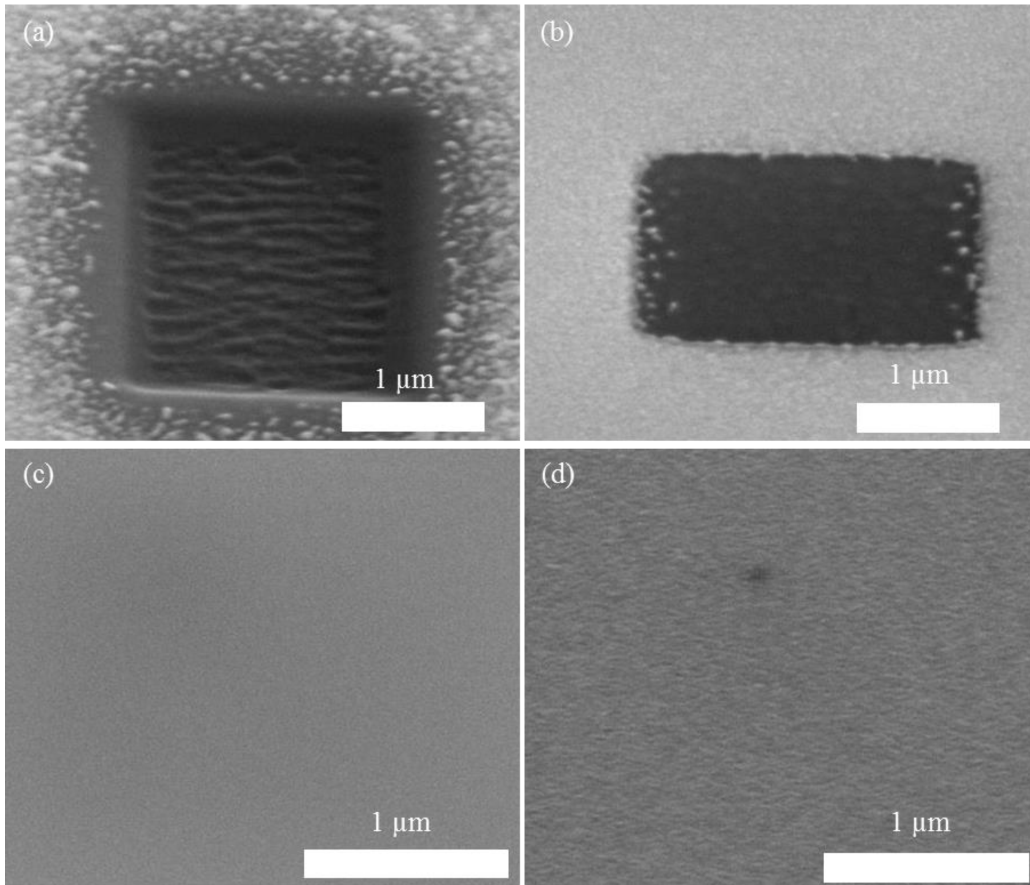

Fig. 2-33 The experiment results of nanostructure patterning on thin film metals show strong interaction between the incoming gases and metal atoms.

As summarized in Table 2-6, the fabrication process of various metallic nanostructures on conductive and nonconductive substrates were developed with different resist types. The achieved minimum feature size was as low as 20 nm with 10% dimension tolerance. The dry etching experiments of c-Si were mainly conducted on ZEP-520 based resist due to the better etching resistance.

<table>
<tr><td rowspan="2">Resist type</td><td colspan="4">PMMA</td><td colspan="3">ZEP (original part : diluted solvent)</td></tr>
<tr><td>2%</td><td>4%</td><td>6%</td><td>8%</td><td>1:1</td><td>1:2</td><td>1:4</td></tr>
<tr><td>Shape</td><td colspan="4">rods, disks, rings, fishnet, SRR, grating, interdigitated, H shape, SRR pairs</td><td colspan="3">holes, fishnet, grating</td></tr>
<tr><td>Accuracy</td><td colspan="7">After dose calibration, the dimension accuracy could be controlled below 10%</td></tr>
<tr><td>Minimum feature size (nm)</td><td>60</td><td>100</td><td>120</td><td>200</td><td>200</td><td>150</td><td>100</td></tr>
<tr><td>Substrates</td><td colspan="4">c-Si, a-Si, ITO, GaAs, glass</td><td colspan="3">c-Si, ITO</td></tr>
<tr><td>Dry etching</td><td></td><td></td><td>Y</td><td>Y</td><td>Y</td><td>Y</td><td>Y</td></tr>
<tr><td colspan="8">Table 2-6 The brief summary of fabrication process development of metallic nanostructures on various substrates and nanostructures patterning on c-Si substrates.</td></tr>
</table>

2.7 Process Integration Platform

In order to integrate metallic nanostructures on light detection devices, a process integration platform was firstly developed. A typical single horizontal Si nanowire device was developed as a universal platform for other 2D device applications such as ZnO nanowire, Graphene, carbon nanotube, etc. The EBL stitching and alignment capabilities were first evaluated on c-Si substrates. Fig. 2-34 (a) shows the EBL stitching mechanism. The dashed line square is the target device area with 2×2 field array in one single EBL writing schedule file. The blue square represents the exposed field and the red square shows the unexposed field. The position error between target and actual fields is marked with d1 and d2 in x and y directions. Through the stitching results shown in Fig. 2-34 (c), the errors at x and y directions were both within 10 nm. Fig. 2-34 (b) demonstrates that the EBL alignment resolution was the position

error between fabricated pattern and second exposure pattern. The EBL alignment resolution after evaluation was within 10 nm as shown in Fig. 2-34 (d).

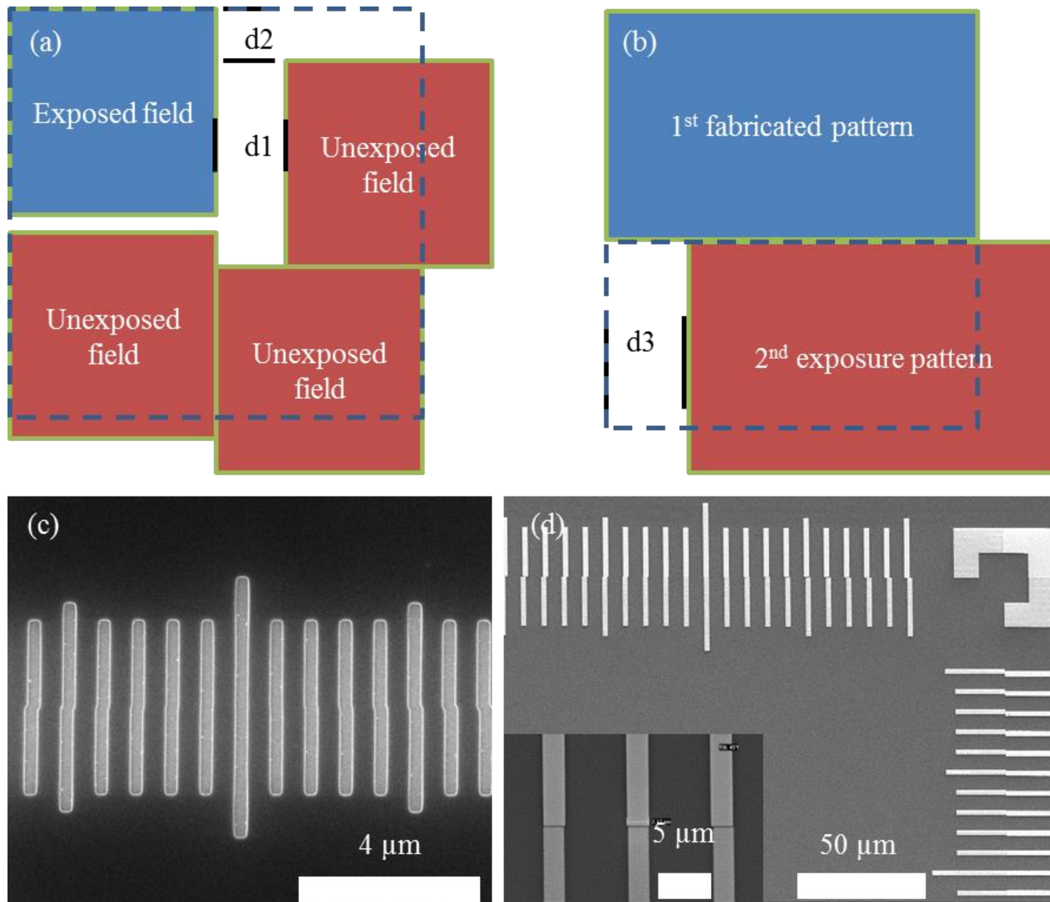

Fig. 2-34 The mechanisms of EBL field stitching and exposure alignment are presented with evaluation results.

The fabrication processing flow of a single horizontal Si nanowire device is shown in Figure 2-35. The global contacts and markers were patterned first by photolithography, originally with 10 nm Ti and 200 nm Au thick. After nanowire deposition, the nanowire positions were randomly located on substrate. Through the EBL alignment procedure, the local contacts were patterned to connect the global contacts with nanowires. With proper modification of this device structure, it could be easily utilized as 2D material photodetectors, photodiodes and transistors.

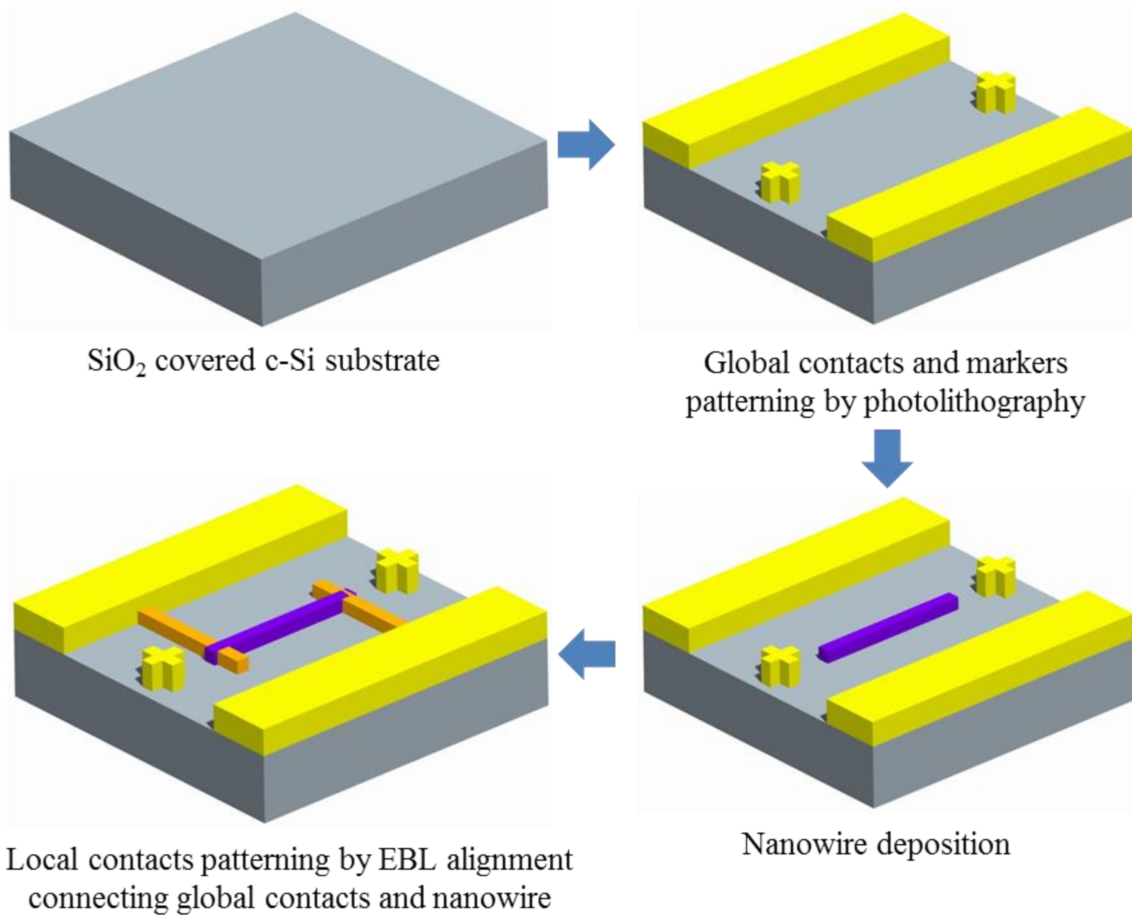

Fig. 2-35 The schematic drawing of horizontal nanowire device is presented.

The SEM image in Fig. 2-36 (a) shows the fabricated global contacts and deposited Si nanowires (marked in yellow squares). In order to develop the single Si nanowire device, the nanowire was connected to global contacts by local contacts. This was achieved by the EBL alignment process using the NPGS system. As shown in Fig. 2-36 (b), the alignment overlays were designed in user defined areas with alignment windows (red squares). The overlays were graphical outlines within the windows. Through SEM imaging, the position of the designed alignment markers was dragged and dropped to match actual patterns. The markers' position before and after alignment are shown in Fig. 2-37 (c) and (d). The fabricated single Si nanowire devices are shown in Fig. 2-36 (a) and (b). The zoom-in image shows the nanowire with two local contact electrodes.

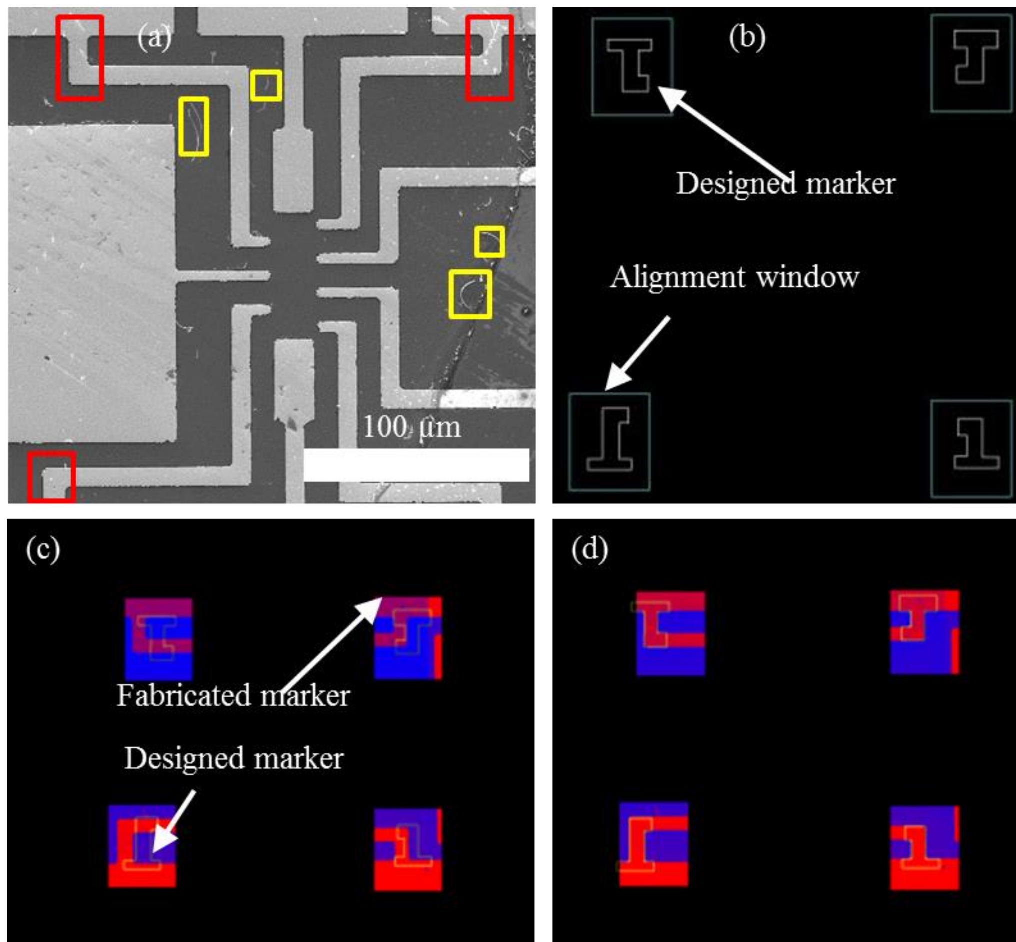

Fig. 2-36 The brief fabrication results of single horizontal Si nanowire device are demonstrated with (a) global contacts fabrication, (b) align markers CAD design; (c) SEM image before alignment; (d) SEM image after alignment.

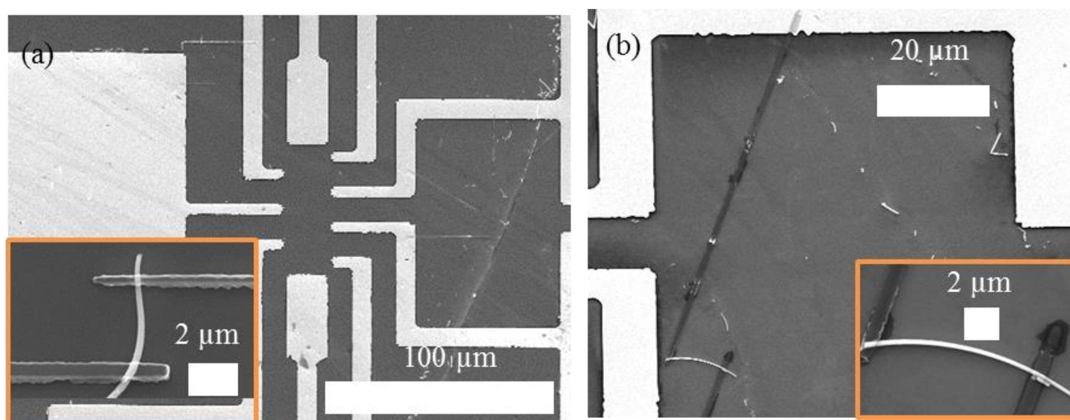

Fig. 2-36 The SEM images show two fabricated single horizontal Si nanowire devices with magnified image shows only the nanowire and local electrodes.

Chapter 3: Fishnet Integrated Schottky Contact a-Si Solar Cell

3.1 Introduction

Schottky contact solar cells have been investigated since 1974 [49]. Different combinations between metals and semiconductor materials have been investigated to estimate the conversion efficiency limit. With the material development, the first Schottky contact a-Si solar cell was reported by D. Carlson *et al.* [50] in 1976. The power conversion efficiency is 5.5% using blanket Pt as Schottky contact with discharge-produced 1 μm a-Si thin film. Although various metallic nanostructures have been proposed as the Schottky contacts, the collective optical and electrical impacts on the device performance were not fully understood. Moreover, the p-i-n a-Si solar cell is preferred due the much better carrier collection efficiency by large internal electrical field. In recent years, metallic nanostructures integrated plasmonic-enhanced a-Si solar cells have been extensively investigated [7, 32]. The incoming light can be scattered and collected more efficient by various metallic nanostructures placed either on top or at the bottom of cells. For a p-i-n a-Si solar cell integrated with 2D electrically connected fishnet structure on top, the modeling work shows the incoming light can be trapped, scattered and concentrated more efficiently [47]. However, these heavily doped p and n regions can introduce high carrier recombination loss in the cell due to the short minority-carrier life time. Comparing to p-i-n structure, it is necessary to revisit the Schottky contact a-Si solar cell integrated with fishnet structure to improve light trapping and carrier collection efficiencies. In addition, by removing heavily doped regions, the carrier collection efficiency can be further improved due to the elimination of the dominant nonradiative recombination loss.

In this chapter, the a-Si continuous band structure was considered with detailed device simulation results. Beyond that, a a-Si solar cell with integrated metallic fishnet structure was

developed. The fishnet structure played multiple roles in this device. It was utilized as a Schottky contact with intrinsic a-Si and light trapping structure to collect more incoming light. If the fishnet spacing was engineered to be less than minority carrier diffusion length, the carrier collection was expected to be more efficient. Since no heavily doped regions were involved, the nonradiative recombination losses were expected to be much lower. Based on simplified analytical calculation, the Shockley-Read-Hall (SRH) recombination saturation current density was predicted to be two orders lower comparing to p-i-n a-Si solar cell. Through numerical simulation, the fishnet structure was optimized with certain geometry parameters to maximize light absorption inside intrinsic a-Si layer. The fishnet structure covered hundreds of microns area integrated on fabricated cells by electron beam lithography (EBL). The detailed device fabrication processes will be reported in fabrication section 3.3.

3.2 Theoretical Analysis

Comparing to c-Si, the non-ideal atomic configuration in a-Si was reflected in the energy band diagram of density of states (DOS). In c-Si, the DOS is formed by a parabolic distribution near the conduction and valence bands. A clear band gap is presented between the band edges. However, the band distribution is broader in a-Si due to the disordered atomic structure. Normally the band tails extend into the band gap with presented defects around the center of the band gap forming the continuous DOS. This continuous DOS distribution consists of parabolic conduction and valence bands, exponentially decaying conduction and valence band tails, and localized defect states related to dangling bonds. Fig. 3-1 shows the calculated DOS distribution in a-Si. The parameters used in calculation were from reference [51]. With the continuous DOS distribution, the carrier transport mechanism was more complicated than c-Si. Not only the band to band transition, but the localized transport was considered. The detailed description was

quantified by the carrier concentrations and mobility in certain states. Since more defect states are involved, the SRH recombination is the dominant mechanism for a-Si.

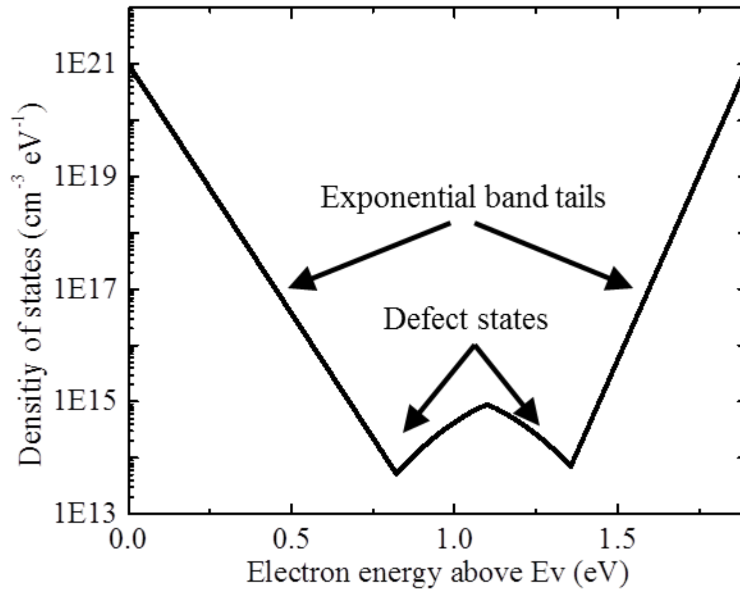

Fig. 3-1 The calculated model of the DOS distribution in a-Si is shown with marked exponential band tails and defect states.

The SRH recombination saturation current density was calculated based on the model in Ref. [52] and [53]. The detailed parameters of a-Si in calculation were collected from Ref. [51]. As shown in Fig. 3-2, the calculated SRH saturation current density in Schottky contact a-Si solar cell was two orders lower than in p-i-n structure a-Si solar cells with carrier life time from 10 ns to 10 μs. It shows that the nonradiative recombination losses of Schottky contact a-Si cells was much less comparing to p-i-n cells because of the removal of heavily doped regions.

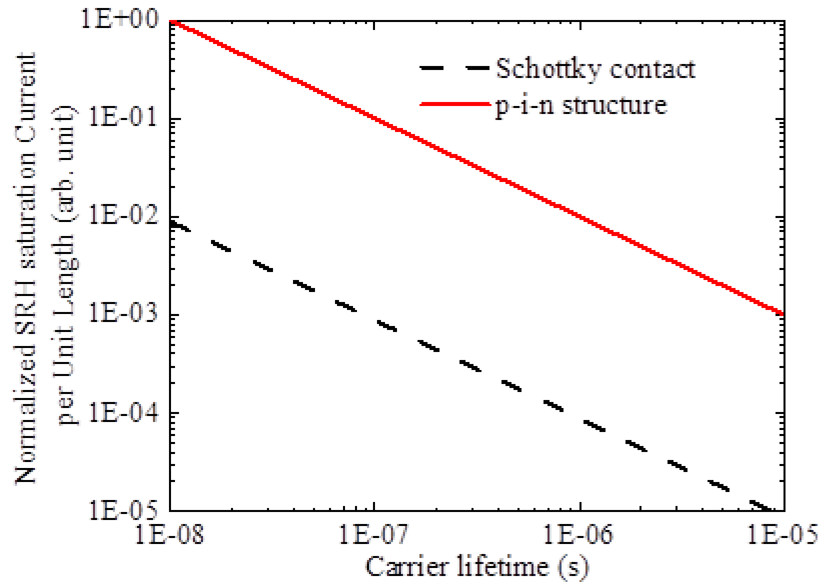

Fig. 3-2 The normalized SRH saturation current densities of Schottky contact (black dashed line) and p-i-n structure (red solid line) a-Si solar cells are shown corresponding to different carrier lifetime [54]. © 2013 IEEE

The light absorption of the metallic fishnet nanostructure integrated a-Si Schottky contact solar cell was analyzed with the finite element simulation by X. Yang [54] using COMSOL Multiphysics). Fig. 3-3 (a) shows the schematic of the solar cell with Au fishnet structure of 50 nm line width and 300 nm intrinsic a-Si layer on the top of aluminum back electrode. The pitch size was 600 nm. In Fig. 3-3 (b), the electric field distributions at the bottom surface of the fishnet structure and the vertical plane of the solar cell were plotted at the wavelength of 632 nm. The strong field localization around the fishnet structure and the constructive interference of optical wave between the fishnet and the aluminum back electrode greatly enhanced the light absorption inside the a-Si layer. Fig. 3-3 (c) gives the simulated reflection spectrum and absorption spectra in the different regions of the solar cell. The plasmon resonance of the fishnet structures could enhance the light absorption in the a-Si layer significantly. Based on the calculated light absorption spectrum in a-Si layer, the short circuit current of the solar cell at AM 1.5G solar spectrum illumination was obtained. Fig. 3-3 (d) plots the calculated photocurrent

generation spectrum, where it is assumed that all the absorbed photons in a-Si layer contribute to the photocurrent. The photocurrent density was enhanced due to the plasmon resonance of the fishnet structure.

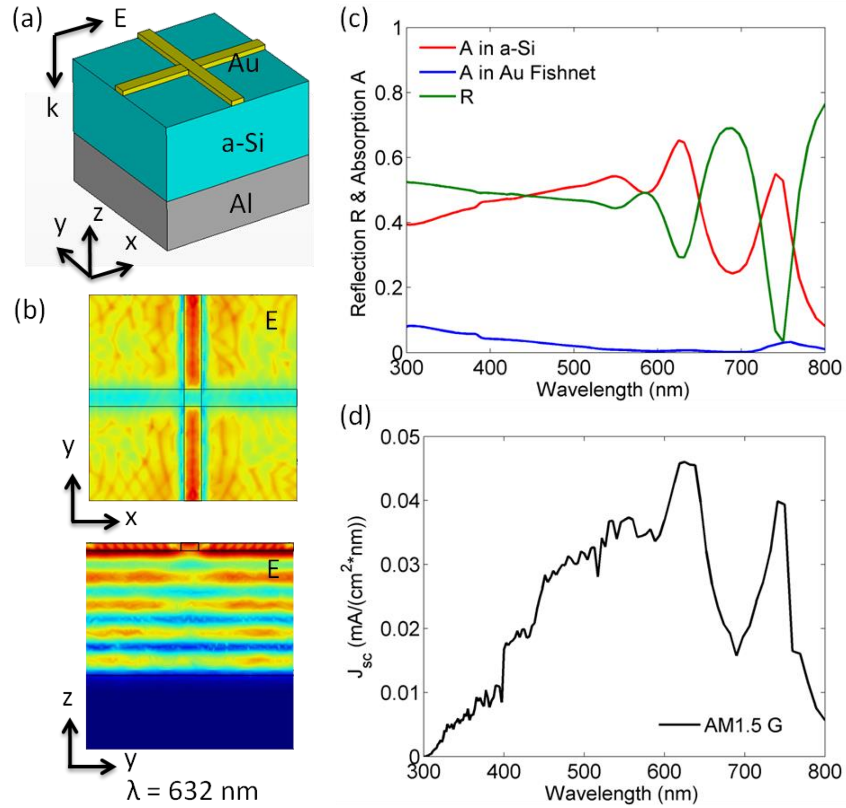

Fig. 3-3 The numeric simulation results are shown [54]. The schematic structure of the simulated solar cell is shown in (a). The typical electric field distributions of the solar cell at the wavelength of 632 nm are shown in (b). The reflection and absorption spectra of the solar cell are shown in (c). The photocurrent generation spectrum is calculated shown in (d). © 2013 IEEE

3.3 Device Fabrication

The mesa fabrication process of a metallic fishnet structure integrated Schottky contact a-Si solar cell is shown in Fig. 3-4. The fabrication started with a glass substrate. The Aluminum (Al) layer was deposited as a bottom contact of 200 nm thick as shown in Fig. 3-4 (b). The 300 nm thick intrinsic a-Si layer was deposited by PECVD on top of Al layer (Fig. 3-4 (c)). After the photolithography exposure, developing, and fluoride based dry etching processes, the intrinsic a-

Si layer was patterned as four different mesa sizes: 2 mm × 2 mm, 1 mm × 1 mm, 800 μm × 800 μm and 500 μm × 500 μm areas (Fig. 3-4 (d) – (g)). The 3 μm thick AZ 4330 was used as photo resist due to its better dry etching resistance. The N-Methyl Pyrrolidinone (NMP) based solvent stripper Remover PG was used to remove the cap layer of AZ 4330 on etched a-Si (Fig. 3-4 (h)).

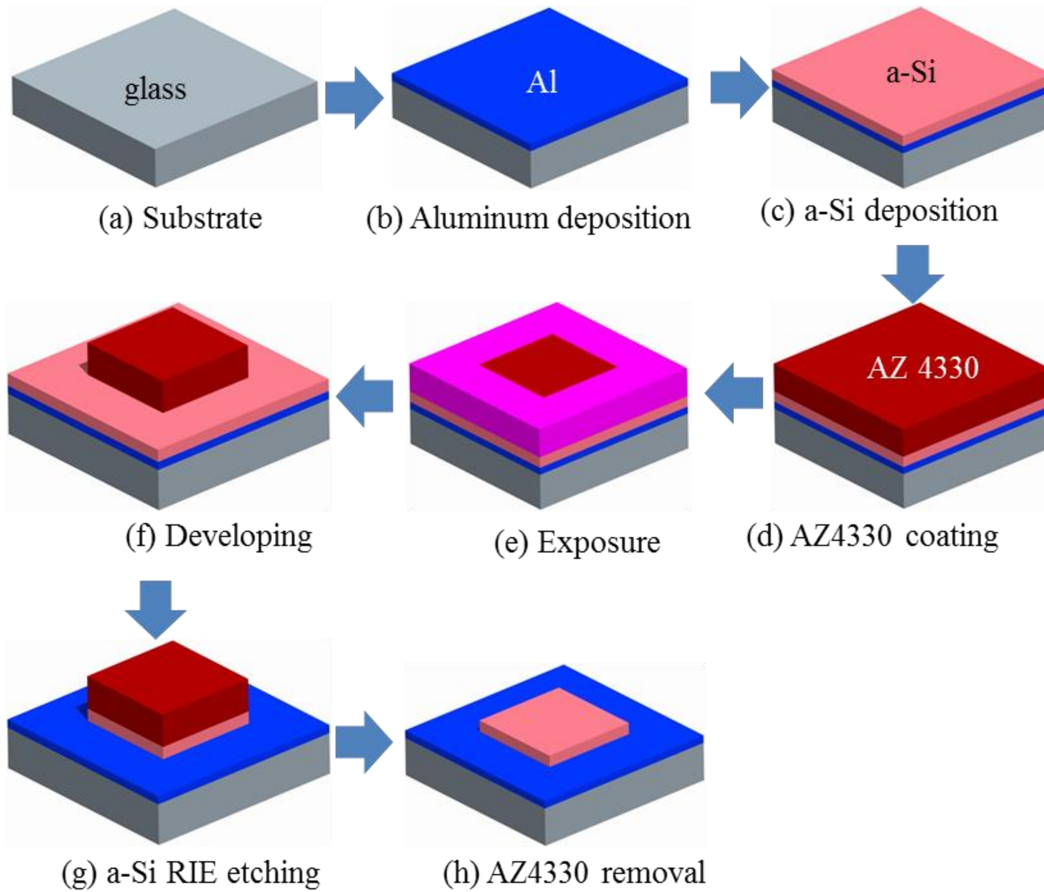

Fig. 3-4 The 3D processing flow shows the a-Si mesa patterning of metallic fishnet structure integrated Schottky contact a-Si solar cell.

The detailed parameters in PECVD and dry etching are summarized in Table 3-1 and Table 3-2.

Temperature (℃)	Gas flow (sccm)	Pres. (mTorr)
250	SiH_4	500
	20	
Power (W)	Time (mm:ss)	
2	30:00	

Table 3-1 The applied PECVD parameters of 300 nm thick a-Si deposition are shown.

Power(W)	Gas flow (sccm)		
	SF_6	O_2	C_4F_8
100	45	5	0

Time(s)	Etch rate of a-Si (nm/min)	Etch rate photo resist (nm/min)
120	325	70

Table 3-2 The a-Si RIE dry etching parameters are used to etch stop at Al layer.

Since the a-Si surface roughness was 80 nm leading to weak EBL alignment detection signal, alignment markers were patterned with 2 nm Cr and 50 nm Au through coating, exposure, developing, metal deposition and lift-off (Fig. 3-5 (a) – (e)). The global contacts were formed in the next step by the same photolithography processes (Fig. 3-5 (f) – (j)). The fishnet structure was aligned and patterned on a-Si by EBL. The 2nm Cr and 10 nm Au were deposited followed by lift-off process (Fig. 3-5 (k)). Since the a-Si surface was rough, a thicker electron beam resist of around 200 nm was used to improve the device yield. Meanwhile, 300 μm × 100 μm metal pads were patterned to collect current.

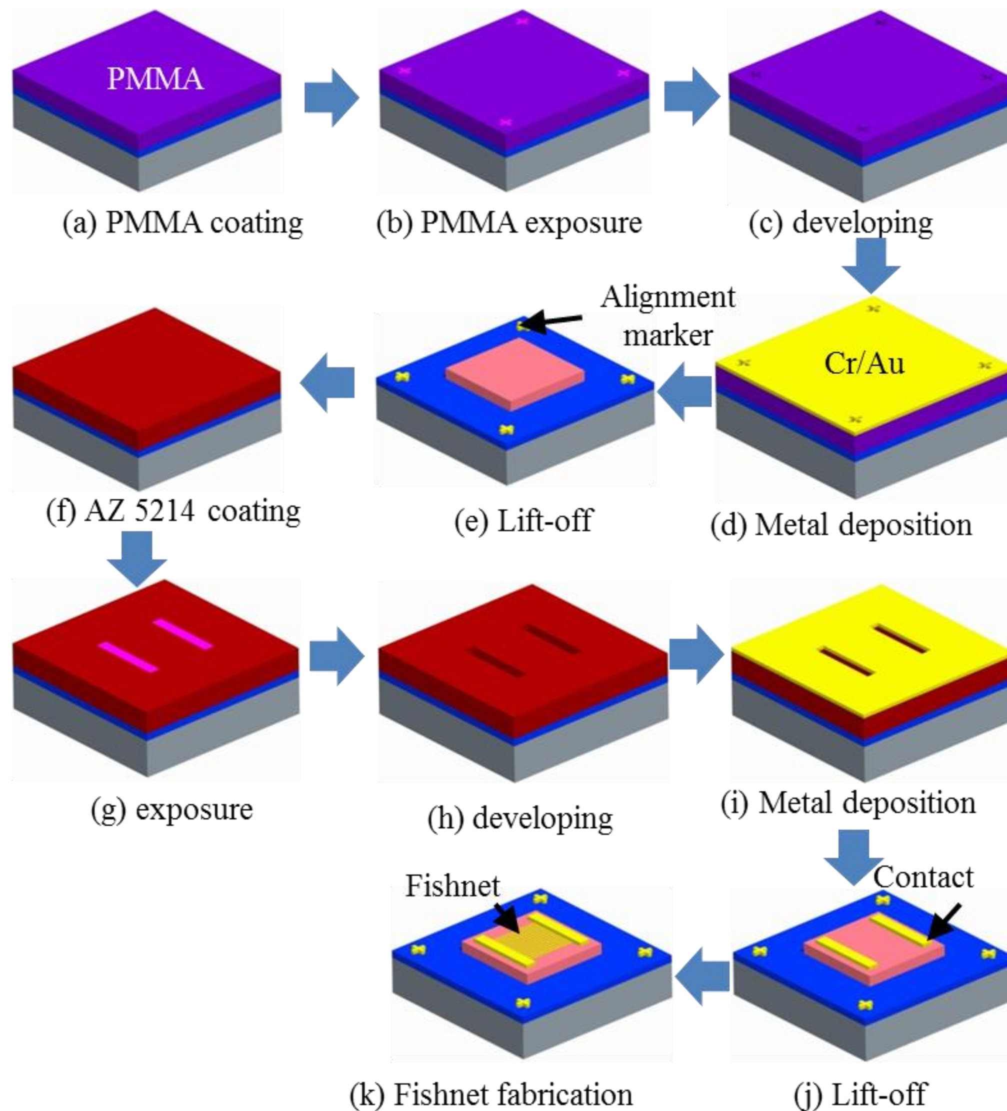

Fig. 3-5 The global contacts and fishnet structures are integrated as fishnet integrated a-Si Schottky contact solar cells.

The device structure shown in Fig. 3-6 was fabricated to verify the ohmic contact between the bottom Al and intrinsic a-Si. The Al contacts were first patterned on glass by photolithography, metal deposition and lift-off. After blanket a-Si deposition by PECVD with the same parameters summarized in Table 3-1, the film was etched by RIE with parameters in Table 3-2. Since the applied processing condition was the same as the fabricated solar cell, the material quality and contact condition kept the same.

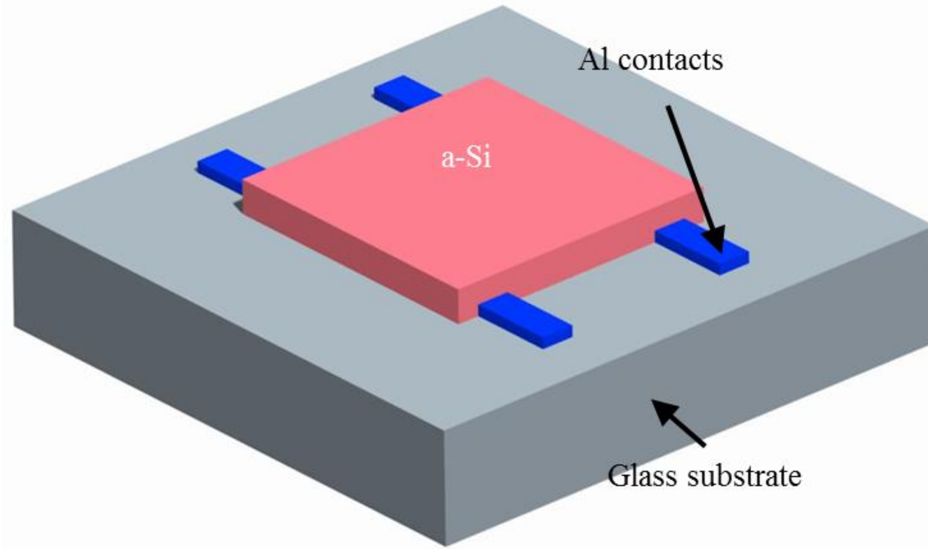

Fig. 3-6 The Al and a-Si ohmic contacts test structure is presented.

3.4 Results and Discussion

The fabricated Al and a-Si ohmic contacts test structure is shown in Fig. 3-7 (a). Since intrinsic a-Si is slightly n-type semiconductor, the formed contact between Al normally was Schottky contact. However, since the followed a-Si deposition was conducted at 250 ℃ (Table 3-1), the Al and deposited a-Si interacted to form Al-Si mixed phase or c-Si as low as 150 ℃ [55]. Through the current voltage (I-V) measurement shown in Fig. 3-7 (b), the ohmic contact was formed between Al and intrinsic a-Si layers.

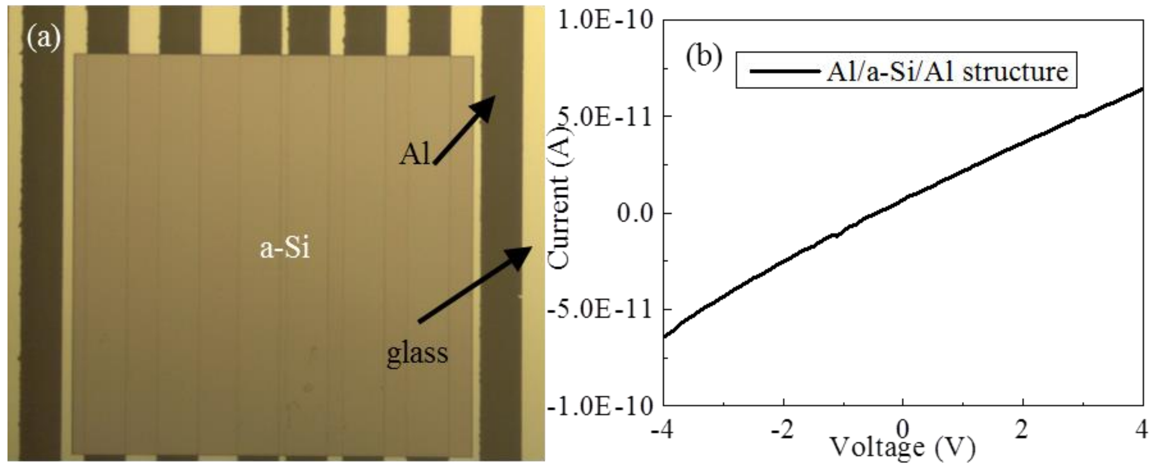

Fig. 3-7 The fabricated Al/a-Si ohmic contact structure is presented with I-V measurement results.

The SEM images of fabricated metallic fishnet structure integrated Schottky contact a-Si solar cell are shown in Fig. 3-8. They showed the a-Si mesa was 800 μm × 800 μm with the inset magnified SEM image of fishnet structure. The line width was 90 nm with two different pitch sizes of 600 nm and 1 μm, respectively. Other cells with different mesa sizes were available including 2 mm × 2 mm, 1 mm × 1 mm and 500 μm × 500 μm. The back Al contact thickness was 200 nm with 300 nm intrinsic a-Si on top. The global contacts and fishnet structures were deposited by 10 nm Au to insure 90% light passing to a-Si active layer. The EBL alignment markers were made by 10 nm Cr and 100 nm Au which provided large signal to noise ratio during alignment.

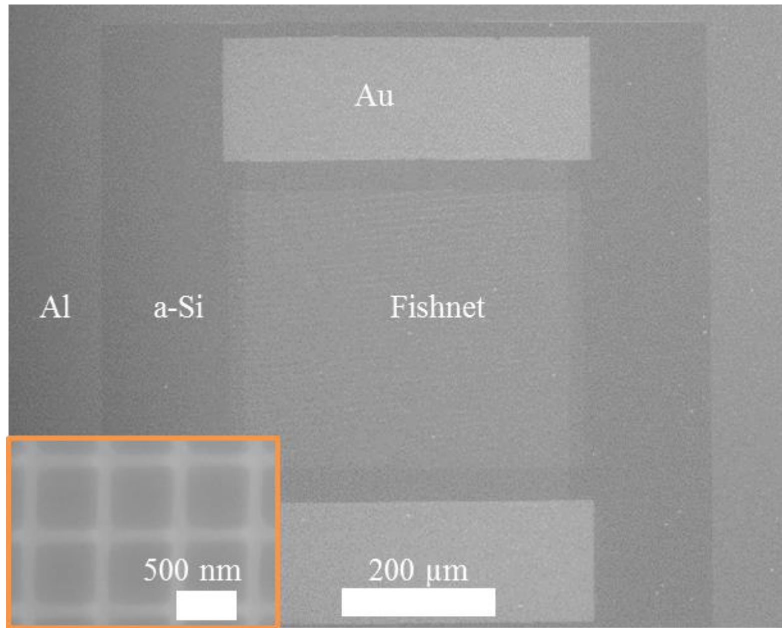

Fig. 3-8 The fishnet structure was integrated on 800 μm × 800 μm a-Si mesa forming Schottky contact a-Si solar cell.

To evaluate the fabricated solar cell performance, the dark J-V measurements were conducted first. The measured J-V curves in Fig. 3-9 (a) present the conductivity changing by applied voltages on various mesa sizes from 500 μm × 500 μm to 2 mm × 2 mm. It showed clearly the consistent conductivity across different mesa sizes. Through following data analysis, the saturation current I_s was calculated around 1.3×10^{-7} A/cm^2 and the series resistance was 6.3×10^4 Ω. The extrapolated ideality factor was around 7.7, which was much larger than 1. The barrier height was calculated around 0.74 V using n-Si Richardson's constant around 112 A/cm^2·K^2. However, after comparing to the published J-V curve of a-Si by C. Wronski *et al.* [56], the conductivity of the fabricated device at 1 V forward bias was two orders lower than the published results, and four orders higher at 1 V reverse bias.

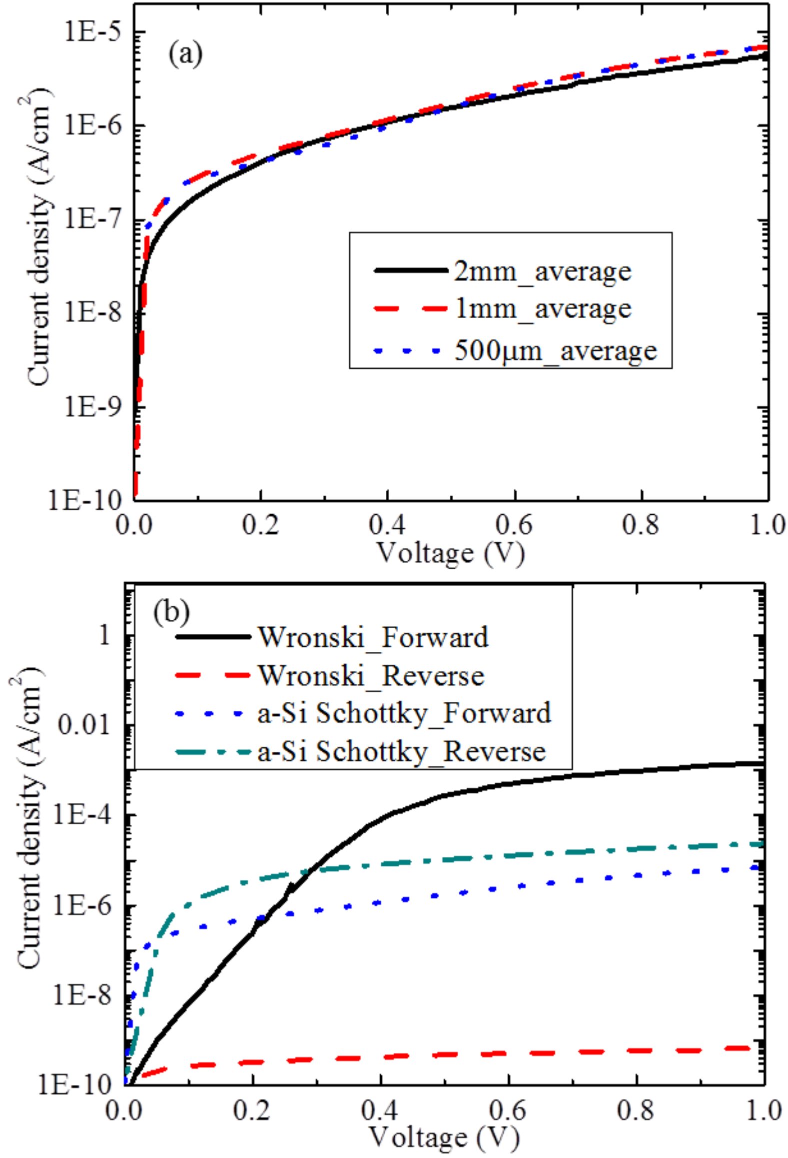

Fig. 3-9 The presented J-V curves show the consistent conductivities on different mesa sizes.

Furthermore, more parameters were extracted and verified through temperature dependent current-voltage measurement. The utilized temperature range was from 270K to 340K. Fig. 3-10 shows the Richardson plot of Log(I/T^2) versus 1000/T at the constant forward bias voltage at 0.2V. Through the Schottky barrier height calculation equation [57]

$$\phi_B = \frac{V_1}{n} - \frac{2.3k}{q}\frac{d[\mathrm{Log}(I/T^2)]}{d(1/T)}$$

With calculated n=7.7 and the slope of $d\left[\mathrm{Log}\left(\frac{I}{T^2}\right)\right]/d\left(\frac{1}{T}\right) = -0.69$. The barrier height $\phi_B\left(I - \frac{1}{T}\right) = 0.16V$ which was much lower than calculated $\phi_B(I - V) = 0.74V$.

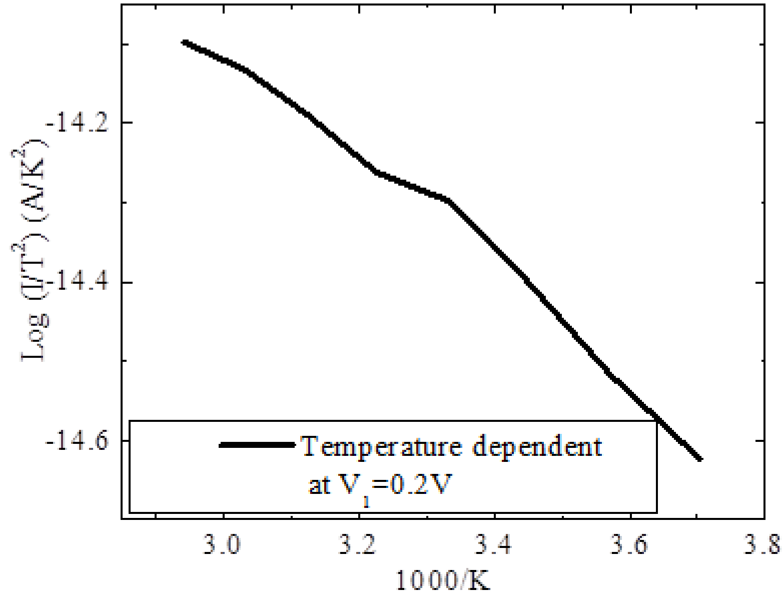

Fig. 3-10 The temperature dependent current-voltage measurement was conducted from 270K to 340K.

To evaluate the photovoltaic device performance, the dark and light J-V measurements were conducted on fabricated cells with and without a fishnet structure. The measured I-V curves in Fig. 3-11 showed that the device quality might not be able to reach the expectation. The calculated filling factor was 25.3%, 25.5% and 15.0% for standard fishnet, 1 μm gap fishnet and without fishnet cells, respectively.

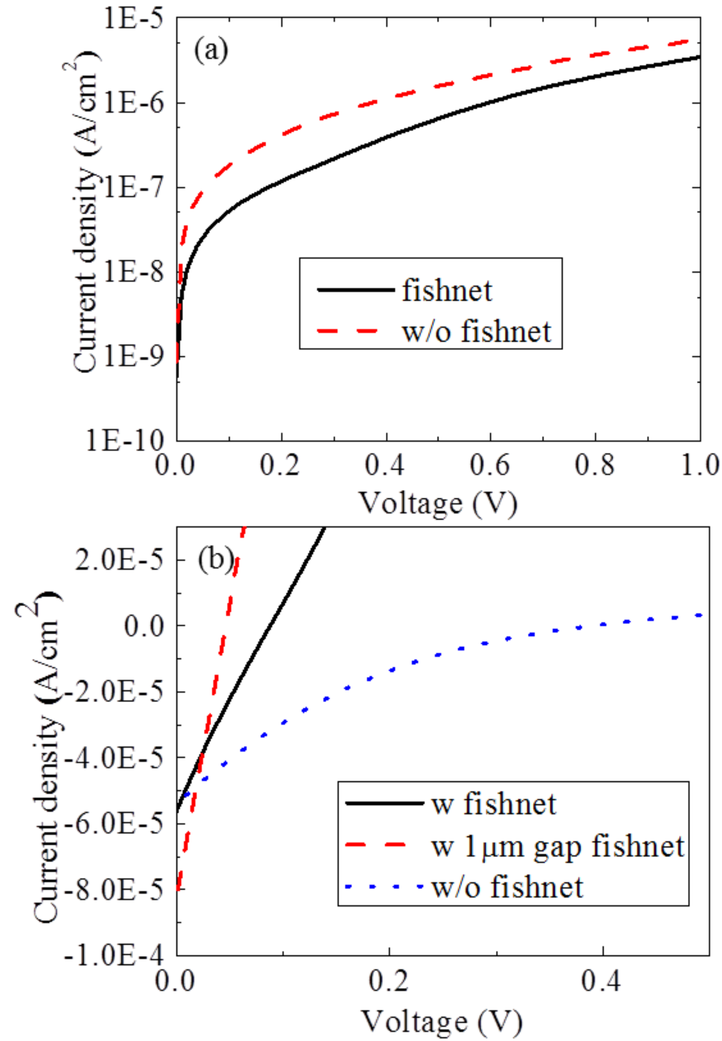

Fig. 3-11 The comparison between cells with and without fishnet structures are shown. Fig. (a) shows the dark I-V curve and (b) shows the light measurement result.

Through photoresponse and quantum efficiency (QE) measurements, the device performance was further evaluated. The fishnet integrated device photoresponse and QE curves were shown in Fig. 3-12. The response value of device with only global rectangle contacts was hundreds of times lower, which was not included in the figure. Instead of the fishnet contact, the device with fully covered thin metal contacts (10 nm) was measured and compared. The device integrated fishnet Schottky contact showed 10% higher response and QE values between 400 nm - 450 nm and 650 nm - 800 nm. For the shorter wavelength improvement, it was due to the

reduced shadowing effect by fishnet structure. For better longer wavelength performance, the photon generated carriers were easily collected by this 2D connected contact. Compared to the device with only global contact, the fishnet structure improved 1000 times of the carrier collection efficiency with light trapping effect and reduced carrier transit time.

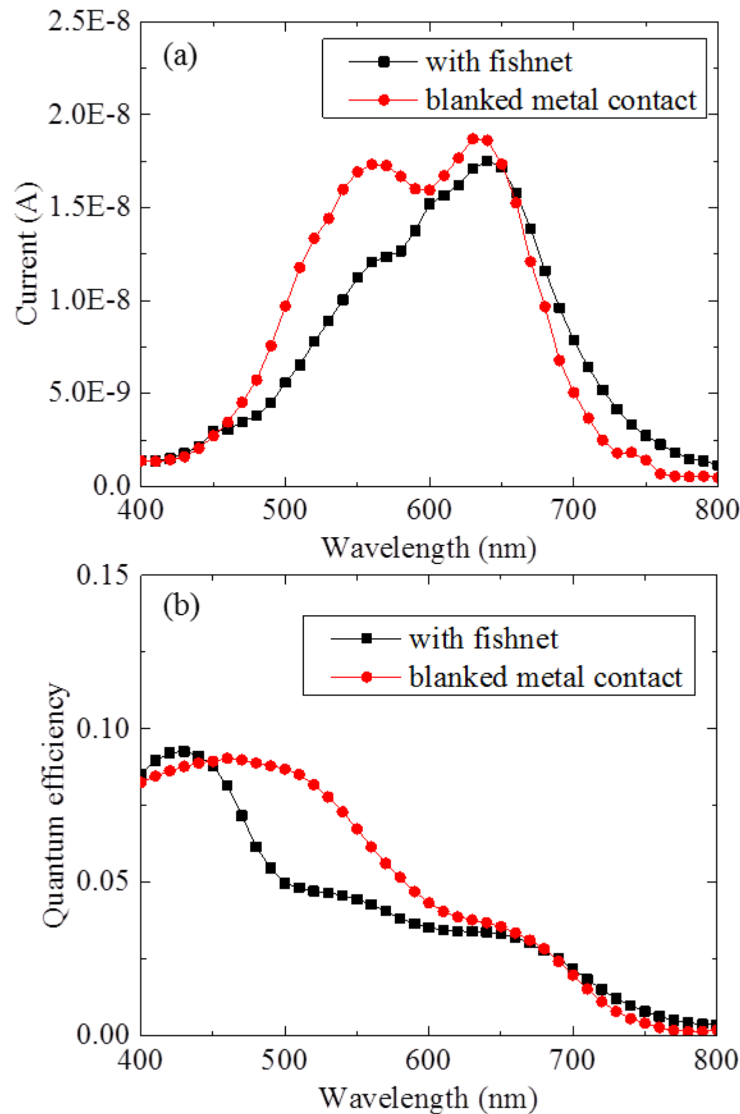

Fig. 3-12 The photoresponse and quantum efficiency measurement results are shown. The devices integrated with fishnet Schottky contact and blanked metal Schottky contact were compared.

Chapter 4: Metallic Nanostructures Integrated GeSn Photodetectors

4.1 Introduction

Si has been the dominant material in semiconductor integrated circuit for many years. With the feature size continues scaling down, conventional electronic interconnects using discrete components and wires limit the whole system performance, especially the chip size and transmission speed. The signal propagation delay between chips and parts becomes comparable with computation delay. Instead of communication by electrons, chip-scale optical interconnects including active and passive photonic devices with much higher bandwidth might be the possible solution for future chips. Optoelectronic devices based on GaAs and InP alloys have been integrated on top of Si with existing 4.1% and 8.1% lattice mismatches respectively [58]. The corresponding thermal expansion coefficient mismatches are 120.4% and 76.9% respectively. This creates unacceptable high densities of threading dislocations of 10^8 - 10^{10} cm^{-2} in the active region of III-V devices [59]. However, with reduced chip size, innovative optoelectronic devices that can grow monolithically with fully CMOS compatible process are required. This limits the future possibility of III-V optoelectronic devices and Si on-chip integration. The preferred interconnect devices also need to accommodate with nano-scale modern electronic devices and the long distance telecommunication at 1.55 μm infrared wavelength.

Ge has been investigated many years as a candidate for on-chip IR fully CMOS compatible optoelectronic components. For light emitting devices, since Ge is an indirect band gap material, it is difficult to realize high efficient devices. Different methods have been applied including heavy doping [60] and strain engineering [60, 61]. An electrically pumped room temperature Ge laser has been demonstrated with heavily doped junction and 0.25% tensile strain, the lasing threshold is around 280kA/cm^2 and the efficiency is very low comparing 1mW of

output is measured [62]. It is not a practical device with its high threshold and poor efficiency. Although the theoretical calculation shows a possible two orders magnitude lower threshold reduction with the same doping level and almost 2% tensile strain [63], the real has not been realized yet. Again, the large tensile strain induced by thermal expansion mismatch between Ge and Si cannot be applied to CMOS process line. Moreover, the developed Ge detectors cannot fully cover all the telecommunication bands.

Tin (Sn) is another group IV material that has two crystal structures (α-Sn of diamond cubic structure and β-Sn of tetragonal structure). The former structure is the interest of this chapter existing below 13.2 ℃ and the latter exists above that temperature. The substitution of Sn atoms into Ge lattice leads to the formation of $Ge_{1-x}Sn_x$ alloys that provide another possible solution for infrared optoelectronic devices. The small difference around 140 meV between indirect and direct band gaps of Ge can be overcome by introducing Sn atoms into lattice as shown in Fig. 4-1 [58]. A active and passive optoelectronic devices could be achieved with different Sn compositions. Moreover, the fabricated device would be fully compatible on Si CMOS processes. It increases the possibility to realize group IV optoelectronic devices by band gap engineering. Nevertheless, this material system is still at the nascent development stage with many unknowns to explore. Many researchers have been investigating on the high quality material growth and device prototype development.

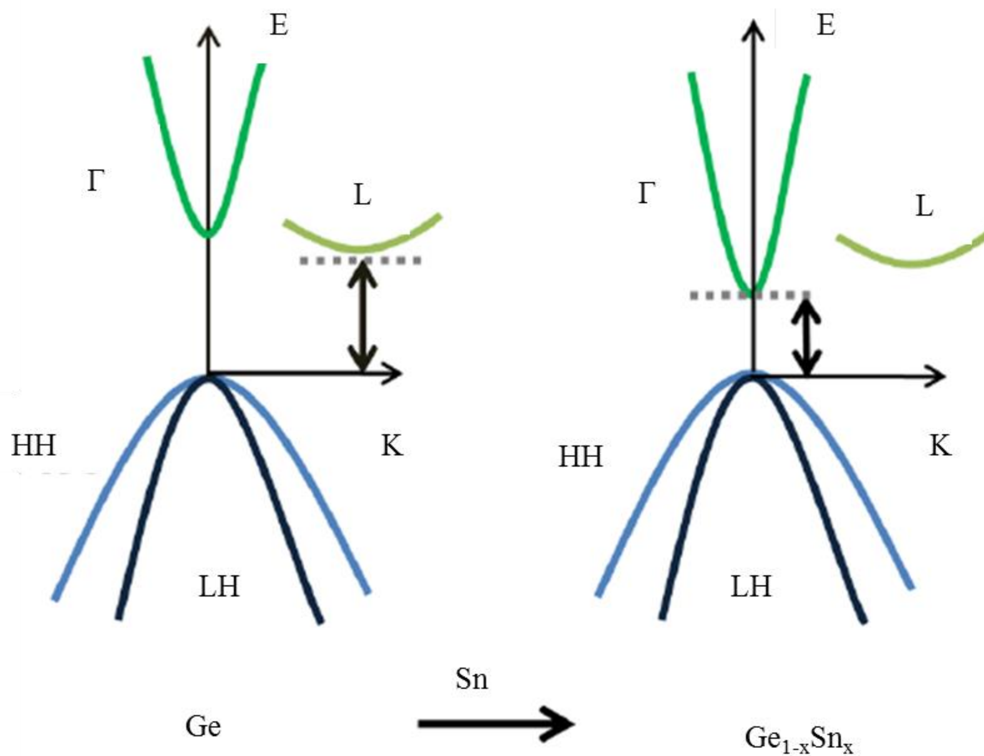

Fig. 4-1 The schematic band structure shows the effect of Sn alloying on the band structure of Ge [58].

In GeSn growth, since the maximum equilibrium solid solubility of Sn in Ge is around 1.1% at 400 ℃ [64], the GeSn layer growth condition is far away from equilibrium to achieve supersaturated solid solution of Sn in Ge. With lower growth temperature, the Sn surface segregation can be minimized by reducing surface mobility. Since no proper gaseous precursors available for Sn deposition by chemical vapor deposition (CVD) until late 1990s, molecular beam epitaxy (MBE) was the dominant method in the earlier period. Because the Sn (6.49 Å) has a 14.7% lattice constant difference from Ge (5.658 Å) and it has the largest lattice constant in group IV, the first GeSn layer growth was on III-V (001) oriented InSb (6.479 Å) and CdTe (6.483 Å) by MBE at 25 ℃ [65]. With these lattice matched substrates, the high Sn concentration GeSn films could be grown with relative low temperatures below 200℃ by MBE

[66], even pure Sn films [67]. The Sn concentrations of GeSn layers grown on Si and Ge substrates by MBE are relative low due to the large lattice mismatch [68-71]. The crystallization forming single crystal GeSn by rapid thermal annealing from thermal evaporated amorphous Ge and Sn has been reported recently with measurable results [72]. For CVD growth of GeSn films, the SnD_4 is firstly applied as Sn precursor with Ge_2H_6 [73]. The deposition is conducted in UHVCVD at temperature between 250 ℃ and 350 ℃ with Sn content s up to 20%. The fabricated film is around 50 - 500 nm and characterized by RBS and XRD (Fig. 4-2). An improved precursors set of Ge_3H_8 and SnD_4 is demonstrated with higher film growth rate with Sn concentrations up to 9% and thicknesses approaching 1 μm [74]. Although SnD_4 has been successfully commercialized as Sn precursor for industrial usage [75], the relative short shelf life and extremely toxic property really limit the further applications both in research and development. Meanwhile, another CVD growth precursor set of $SnCl_4$ and Ge_2H_6 has been developed with Sn contents up to 8% using Atmosphere Pressure Chemical Vapor Deposition (APCVD) [76, 77]. The $SnCl_4$ is a liquid at room temperature and can be evaporated to CVD chamber by using a vapor station. The developed GeSn layers either on Si or Ge process preferred semiconductor device properties as summarized in [78]: (a) strain relaxed film with low threading dislocation density; (b) fully compatible growth temperate with CMOS; (c) adjustable lattice constant and flat surface as ideal substrate; (d) easy cleaning process.

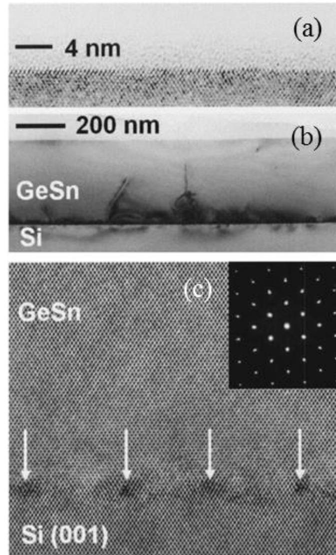

Fig. 4-2 It shows the cross sectional TEM image of $Ge_{0.94}Sn_{0.06}$ grown by UHVCVD [73]. The top image shows the GeSn layer morphology. The middle one shows the uniformity of film. The bottom one shows the GeSn and Si interface with indicated misfit dislocations.

With continuous developed material growth techniques, GeSn based optoelectronic devices attract more attention for applications in near and mid IR ranges, especially at the telecommunication bands. Different simulation and modeling work show the direct band gap of GeSn layer could happen with Sn concentration less than 10% [79] and as low as 6.3% [80]. However, the 2% Sn in Ge films was examined provided ten times larger absorption coefficient at 1.55 μm than Ge that will greatly enhance the detectors performance [79, 81]. The experimental results showed the direct gap is located with 7-8% Sn [74, 82]. With Sn composition increased, the position of Γ-point at the conduction band will decrease that might lead to higher light interaction efficiency with light emitting possibility. The electroluminescence (EL) from direct band gap results have been reported suggesting the possibility of electrical injection in devices [83].

The first GeSn based photodetector was developed using UHVCVD by R. Roucka et al. [84] in 2008. The fabricated device structure with detailed parameters is shown in Fig. 4-3. Two

generation devices of fully CMOS compatible are developed with improved performance. With optimized growth recipe and post rapid thermal annealing process, the fabricated GeSn films achieved better surface and bulk morphology with fewer thread dislocations. Instead of wet etching, reactive ion etching (BCl_3 based) was used to define GeSn mesa area on thicker film (350 nm and 500 nm) devices. The measured photoresponse showed two to three times larger of 500 nm thick samples than thinner ones with optimized growth and fabrication processes.

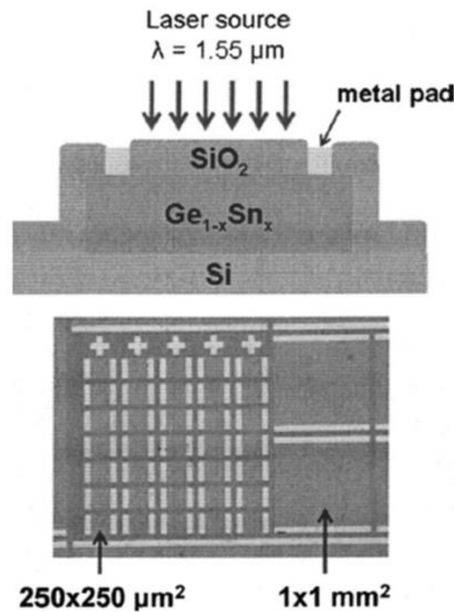

Fig. 4-3 The top image shows the cross-sectional schematic drawing of fabricated GeSn photodetector [84]. The 100 nm SiO_2 is applied as antireflection coating. The top contact is made by 10 nm Cr and 200 nm Au. The bottom image shows the optical image of devices with different lattice geometry sizes from 250 μm × 250 μm and 1 mm × 1mm.

Similar to the Ge based optoelectronic device development strategy, a p-i-n structure device with built-in electric field was proposed instead of requiring perfect material quality for device development. The first device is demonstrated covering the full telecommunication spectrum with p-type Si as bottom contact [85]. Intrinsic GeSn layer thickness of 350 nm was deposited on Boron doped Si (100) substrate using UHVCVD followed by phosphorus doped 64 nm GeSn layer. The top contact was made by 20 nm Cr and 200 nm Au. Circular mesas of

diameter from 60 μm to 300 μm were patterned through RIE. Although the measured dark current density of 1 A/cm^2 was two orders higher than corresponding Ge devices [86], the quantum efficiency measurement showsed photoresponse up to 1750 nm that was beyond the Ge direct band gap. The detailed performance comparison showed the better quantum efficiency of only 2% Sn content of GeSn based devices than Ge ones from 1000 nm to 1800 nm with possible application in multi junction photovoltaic devices [87]. Comparing to UHVCVD growth, the GeSn p-i-n photodetectors developed based on MBE showed a relative low Sn concentration around 0.5% [88]. Instead of deposition on p-type Si substrate and capped with n-type GeSn layer [85], the intrinsic GeSn layer was deposited on 400 nm p$^+$ Ge films and capped with n-type Ge/Si. The measured responsivity at 1.55 μm was 100 mA/W that is twenty times larger than 5mA/W reported in [85]. A similar result with thicker intrinsic $Ge_{0.97}Sn_{0.03}$ layer (820 nm) grown by MBE has been reported with comparable dark current and responsivity of 0.23A/W at 1.54 μm [89]. Instead of a Ge buffer layer on n-type Si substrate, an improved device with GeSn films directly deposited on Ge bulk substrates showed a lower dark current around 6.1 mA/cm^2 (1 V reverse bias) and better photoresponse value of 0.62 A/W (5 V reverse bias) at 1.55 μm [90]. The measured photoresponse extended to 2100nm. Another $Ge_{0.975}Sn_{0.25}$ on Si p-i-n photodetector with improved UHVCVD growth rate and temperature has been reported with comparable responsivity of 0.13 A/W at 1.55 μm [91]. In 2012, a GeSn/Ge heterostructure was grown by atmospheric pressure chemical vapor deposition ASM Epsilon EPI reactor with 9% Sn content [92]. The GeSn quantum wells were grown with thickness of 20 nm and separated by 100 nm Ge barriers. The 2 μm width interdigitated electrodes separated by 4 μm spacing were connected to two large contact pads. The dark current of the sample with Ge as

cap layer was one order lower than the one without Ge cap. The measured photoresponse was 1 A/W at 1.55 μm and can be extended to 2.4 μm with three GeSn quantum wells.

Using GeSn as active layer for light emitting device has been proposed with different structures [93-95]. The direct band gaps with different Sn contents have been investigated by photoluminescence studies [82, 96]. The electroluminescence (EL) from Si/$Ge_{0.978}Sn_{0.022}$ p-i-n heterostructure by UHVCVD has been reported with peak position around 0.70 eV providing feasibility for future GeSn lasers [83]. The injection current density range was from 1.4 kA/cm^2 to 2.26 kA/cm^2 with slightly EL signal blue shift. The Si/Ge/$Ge_{1-y}Sn_y$ p-i-n diodes by MBE showed similar EL results with Sn contents up to 4% [97]. The EL peak shifted to IR beyond 1700 nm with higher Sn contents. The first GeSn LED was developed based on Ge/GeSn/Ge double heterostructure p-i-n diode with Sn content at 7.8% [98]. Two emission peaks were observed at 2.164 μm and 2.275 μm corresponding to indirect and direct band gap of GeSn layer. The injection current density was from 318 A/cm^2 to 493 A/cm^2. Another GeSn LED was developed based on GeSn/Ge p-n heterojunction with Sn content at 8% [99]. The emission peak was indicated at 2.15 μm based on spectral measurement. Although no injection current density was mentioned, the emission power was around 1 μW by 15 mA drive current. With lower temperature at 100K the peak intensity was eight times larger than at 300K with slight blue shift. A recent published Ge/GeSn/Ge heterojunction p-i-n LED showed a single emission peak with reported injection current density from 2.5 kA/cm^2 to 5.0 kA/cm^2 [100]. With Sn content increases from 2% to 4.2%, the emission peak shifted from 0.735 eV to 0.677 eV.

Meanwhile, with the GeSn LED development, a GeSn based Whispering-gallery mode microdisk laser has been demonstrated on GaAs substrate with InGaAs buffer layer [101]. Through transmission measurement of two Sn contents devices (4% and 1%), optical modes

beyond 1.55 μm were confined in fabricated GeSn disks. With this new device structure and improved fabrication method, a Ge/GeSn/Ge quantum well microdisk laser has been developed on Si substrate [102]. The sharp whispering gallery mode resonances (Q>340) have been observed on fabricated 2.7 μm microdisk lasers by PL measurement.

With the SiGeSn material system development, other methods have been investigated trying to increase the photoresponse covering longer wavelengths. Since the speed of photodetector is mainly limited by the transit time of photogenerated carriers to the electrodes and the semiconductor depletion area capacitance, with smaller active areas the photodetector can be much faster due to shorter transit time and lower capacitance. However, the incoming photon number will cause relative lower responsivity. The convergence of speed and responsivity can be resolved by concentrating more light into relative smaller active area. The strong optical near field could localize light achieving better absorption performance.

In this case, nano plasmonic antennas have been applied on Ge substrates. The first nano antenna integrated Ge photodetector was demonstrated with C-shaped nanoapertures [2]. The measured photocurrent from the C-aperture at 1310 nm showed 2-5 times higher than from square apertures. The polarized spectrum from 1.37 μm to 1.54 μm showed the larger current with the light polarized parallel to the two arms of fabricated apertures. One improved Ge photodetector with a half wave Hertz dipole antenna has been demonstrated at 1.3 μm with twenty times difference on polarization contrast [33]. The active volume was 0.00072 μm^3 which was two orders smaller than previous detector at this wavelength. The waveguided Germanium based metal-semiconductor-metal (MSM) photodetector showed surface plasmon effect coupled between Al interdigitated electrodes and dielectric layer [35]. The photocurrents showed three times larger of transverse magnetic mode than transverse electric mode at 1 V

voltage. In 2010, one Ge nanowire based MSM photodetector was developed showing twenty-five times larger photoresponse than Ge bulk beyond 1.5 μm wavelength [34]. The detector preserved the antenna effect in the IR range with ultralow dark current around 20 pA. To make the convergence of responsivity and response speed, one split bull's eye shaped aluminum antenna has been integrated on MSM Ge detectors operating at 1.31 μm [36]. A recent plasmonic enhanced Ge photodetector was reported in 2013 by K. Balram *et al.* by integrating nanoscale resonant cavity. The resonant wavelength could be adjusted from 1500 nm to 1650 nm by changing the geometer parameters. Because multiple devices can be fabricated in a single step, broad band IR detectors can be achieved.

In this chapter, metallic nano antennas integrated GeSn photoconductive photodetectors were developed. The fabricated devices incorporated two different Sn content (7% Sn and 0.9% Sn), respectively. The optical characterizations of these nano antennas on ITO coated glass substrates were conducted using spectroscopic ellipsometry. Furthermore, the H shape metallic nano antennas were applied on GeSn photodetector to investigate the device performance. The detailed fabrication and measurement results will be shown in this chapter.

4.2 Optical Characterization of metallic nanostructures

In order to study the innovative electrical and optical properties of the metallic nanostructures integrated GeSn photodetectors, the optical properties of these nanostructures were characterized first. The processing development of metallic nanostructures has been presented in previous chapter. Here the optical transmission and reflection measurement of certain metallic nanostructures is presented. The detailed experiments were conducted on VASE variable angle spectroscopic ellipsometer from J. A. Woollam Co., Inc shown in Fig. 4-4.

Fig. 4-4 The VASE variable angle spectroscopic ellipsometry system is shown in operation mode (this picture is taken by author at Dr. Shui-Qing Yu's lab on March 10 2014).

Ellipsometry is a contactless optical characterization technique that can analyze material optical constants, film thickness, crystal structure, doping concentration and roughness. It is a very sensitive measurement technique measuring the relative phase change in reflected or transmitted polarized light. Compared to intensity reflectance, the ellipsometry is more accurate since both the amplitude and phase changes are measured. As shown in Fig. 4-5, in typical ellipsometry measurement the p- and s- directions are used to present the beam polarization states [103]. The p-direction is the wave vector in the plane of incidence which is formed by incident and reflected beams. The s-direction is perpendicular to p-direction. A right hand coordinate system is formed combining p-, s- and propagation directions. Compared to single wavelength and fixed angle of incidence, VASE system provides optimized sample information. Furthermore, it can provide the flexibility for various materials and structures. Through the spectroscopic ellipsometry measurement, the wavelength dependent optical constants and properties can be collected for further analysis. The quantified polarization change is described

by the amplitude Ψ and the phase difference Δ. Since these two parameters are collected at every wavelength and angle set, the more detailed material properties can be understood.

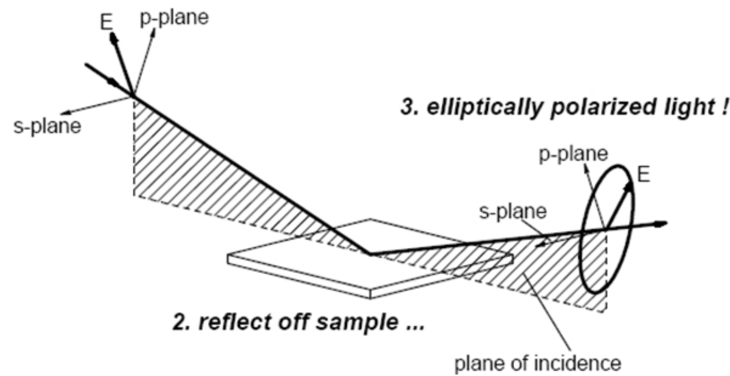

Fig. 4-5 A schematic drawing of ellipsometry experiment is shown with linearly polarized light [103].

The typical procedure for ellipsometry experiments is shown below in Fig. 4-6. The system was first calibrated with a well-known standard sample as a starting point. The measured and collected optical constants were compared with established data to calibrate the system. After calibration, the optical measurement was conducted on a sample with data collection followed by model development. With the developed model, the unknown parameters were fitted into a model based on established data. The model development and data fitting process might take several rounds to find optimized parameter results.

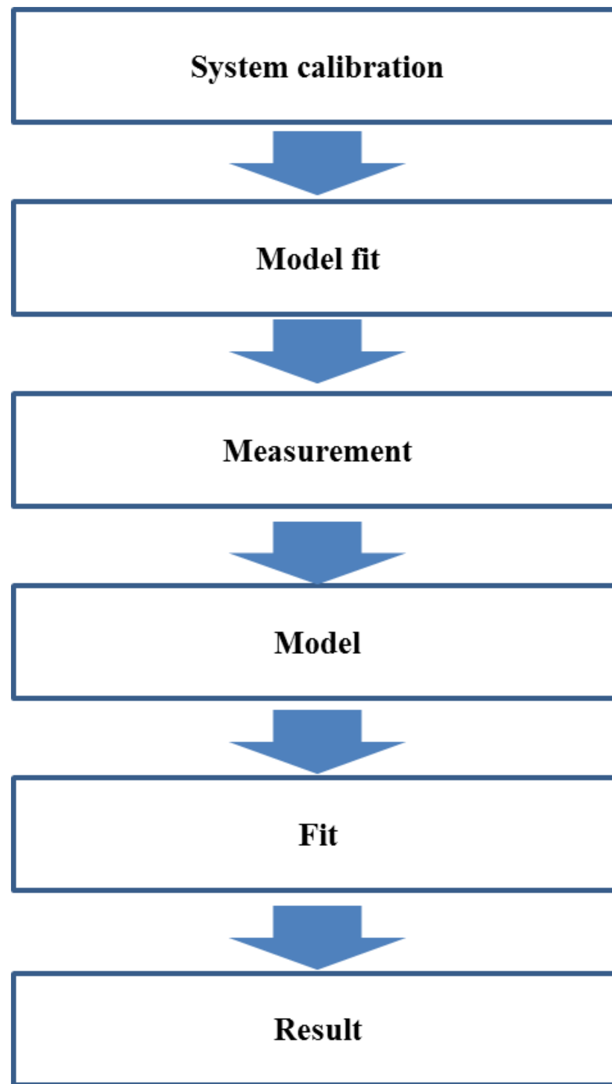

Fig. 4-6 The typical processing flow is shown for ellipsometry measurement.

In system calibration step, a crystalline Si sample covered by 2 nm oxide layer was selected as standard sample. The alignment calibration was first carried out to maximize the signal to noise ratio for x, y and z directions. In x-y plane alignment, the sample surface was roughly aligned vertically to the incident beam at the begining. As shown in Fig. 4-7 (a), after the incident beam reached the sample surface, the light beam was reflected back with an offset position which was shown as the red crossing mark. Through the adjustment knobs, the offset position of crossing mark was tuned less than 0.5 μm to the center position in both directions.

This ensured the incident beam was vertical to the sample surface. The z direction alignment calibration was conducted as a reflection measurement at a 75° reflected angle. As shown in Fig. 4-7 (b), the reflected intensity was adjusted to achieve maximum value.

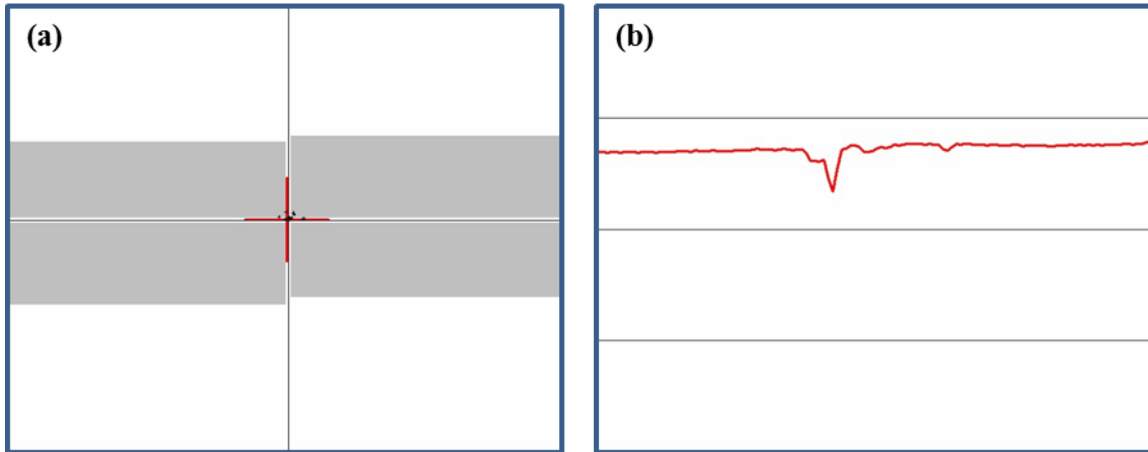

Fig. 4-7 The system calibration windows of x-y and z directions are shown. (a) shows the x-y plane reflection monitoring window with crossing marks. (b) presents the z direction intensity monitoring window.

After the system calibration, wavelength dependent ellipsometry measurements were conducted on the 2” standard oxidized silicon wafer as shown in Fig. 4-8. The measurement was performed at 75° angle of incidence and 500 nm wavelength. Fig. 4-8 (a) shows the actual measurement environment and (b) shows the measured and calculated Fourier coefficients and residual as a function of polarizer angle. It was noticeable that the calculated data were the same from the measurement result which showed the developed model matched with the sample condition and the machine was in nearly perfect condition.

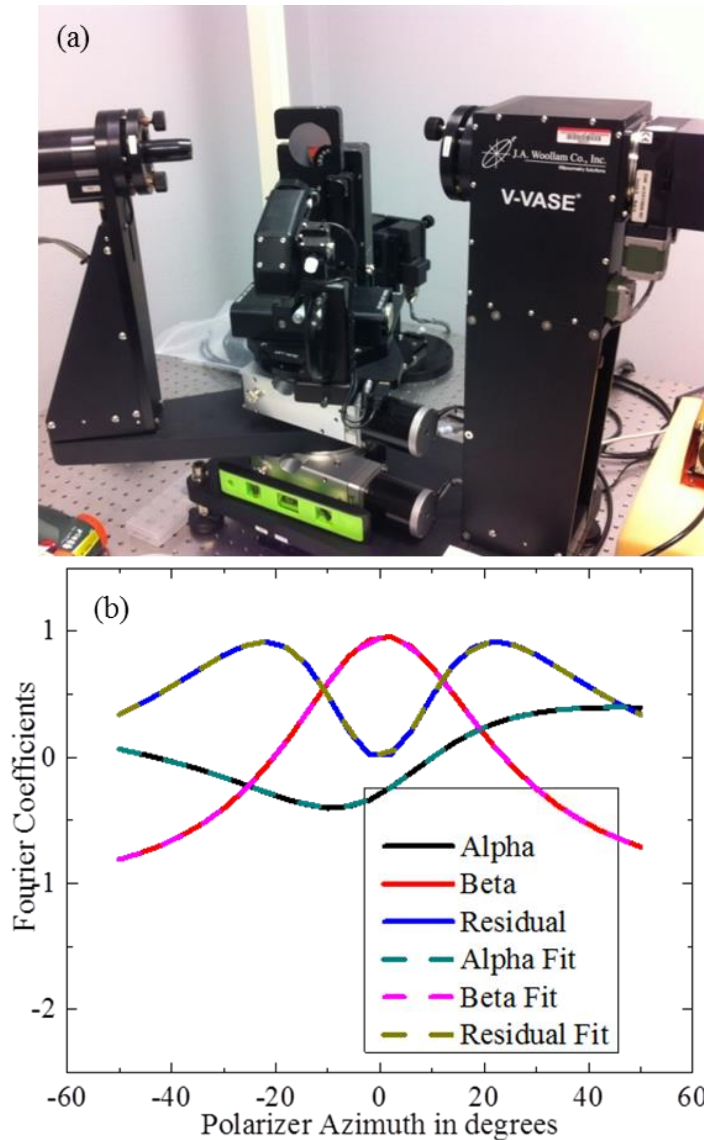

Fig. 4-8 Ellipsometry measurement configuration and results on standard oxidized silicon wafer are shown (the equipment setup picture is taken by author at Dr. Shui-Qing Yu's lab on March 10 2014).

With the verified machine condition and developed model, the ellipsometry measurement was conducted on the fabricated sample. Instead of measuring optical constants and layer thickness directly, the reflected or transmitted beam intensities or polarization rates were measured. The detailed optical constants and sample information were derived through analysis of measured parameters. In this dissertation, the reflection and transmission measurements were two major experimental sets to characterize the properties of metallic nano antennas. With

obtained measurement results, a model was constructed to predict the unknown parameters from known properties. Once the calculated parameters matched with measured curves, the unknown parameters could be derived.

The H-shape metallic nanostructures were fabricated on thin ITO (150 nm) coated glass substrates. The process development has been discussed in chapter 2. The fabricated samples were characterized by transmission and reflection measurement using ellipsometer. Considering the shift of beam trajectory, intensity variation and beam profile changes, a reliable baseline was set first for transmission and reflection measurements. For transmission measurement, two different baselines were compared. The first baseline setup was starting from identical ITO coated glass substrate without nanostructures. The measurement results involved with metallic nanostructures were directly measured. The second baseline sample was assumed as ambient. After baseline data collected from the air, the samples with and without nanostructures were measured in sequence. The real transmission data was the subtraction of these two results data. The detailed comparison results will be discussed in the session. The reflection measurement used a standard oxidized silicon wafer instead of ambient as the baseline measurement. The samples with and without nanostructures were measured as two sets of results. The rt_baseline.mat layer from data base was used to optimize the generated reflection data based on the calculated model. The data acquisition and generated models are shown in Fig. 4-9. With the generated reflection data and previous collected transmission curve, the absorption of the metallic nanostructures was calculated.

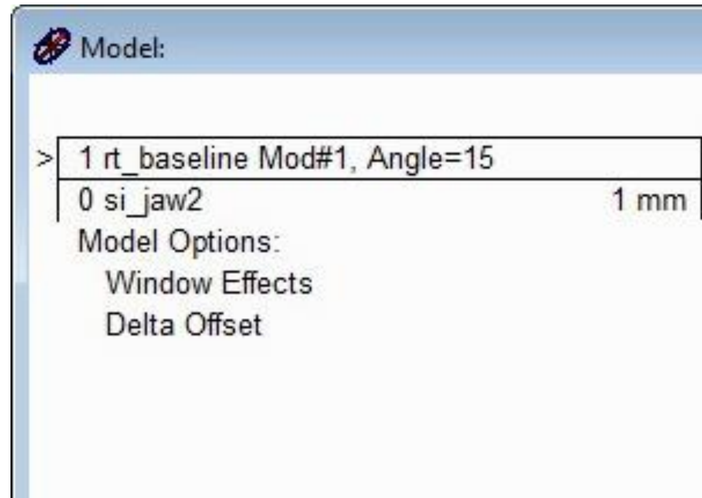

Fig. 4-9 The data acquisition and generated models are shown. (This is a screen shot taken by author at Dr. Shui-Qing Yu's lab on March 10 2014)

The proposed nanostructures and brief fabrication results are shown in Fig. 4-10 (a). The H-shape metallic nanostructures were fabricated with different bridge widths (no bridge, 50 nm, 120 nm and 240 nm). The two different sets of transmission measurements were compared through wavelengths of 400 nm to 2000 nm in Fig. 4-10 (b). The dashed lines present p- and s-polarized transmission data with glass substrates transmission data as baseline. The solid lines were the p- and s- polarized transmission curve by subtraction of sample with and without nanostructures. Ambient air was used as baseline. It was very clearly shown that the transmission measurements which used glass substrate as a baseline was not accurate. The absolute value around 1000 nm was above 100%. In contrast, the transmission curves using ambient air as baseline were relative smoother. In the following transmission measurements, the ambient air was utilized as the baseline model.

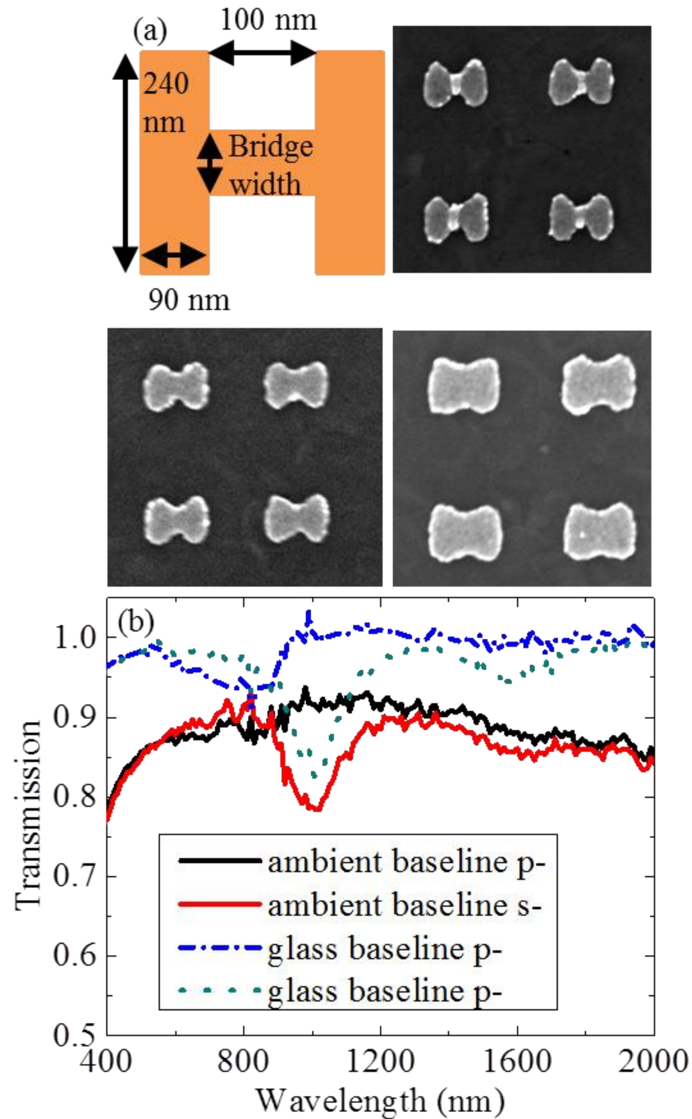

Fig. 4-10 The proposed H-shape metallic nanostructures are shown in (a). The comparison of transmission measurement on different baselines is shown in (b).

According to the well-established baseline, the transmission property of fabricated H shape metallic nanostructures could be analyzed based on measurement results. Fig. 4-11 shows the stacked transmission curves of H shape nano antennas after analysis. Corresponding to various bridge widths, the positions of the transmission valleys were different due to the plasmonic resonance at certain wavelengths, especially for the s polarized direction which was the direction of the bridge. For the H shaped antenna without bridge, the resonant wavelength

was around 830 nm. With the 50 nm width bridge, the resonant wavelengths shifted to around 1700 nm and 1300 nm which were in infrared color. With the increased bridge widths from 50 nm to 240 nm, the resonance valleys shifted from 1700 nm to 1100 nm. In the p- polarized direction, which is vertical to the bridge, the resonant wavelength was around 1000 nm for different bridge widths. The detailed mechanism will be discussed later in this chapter.

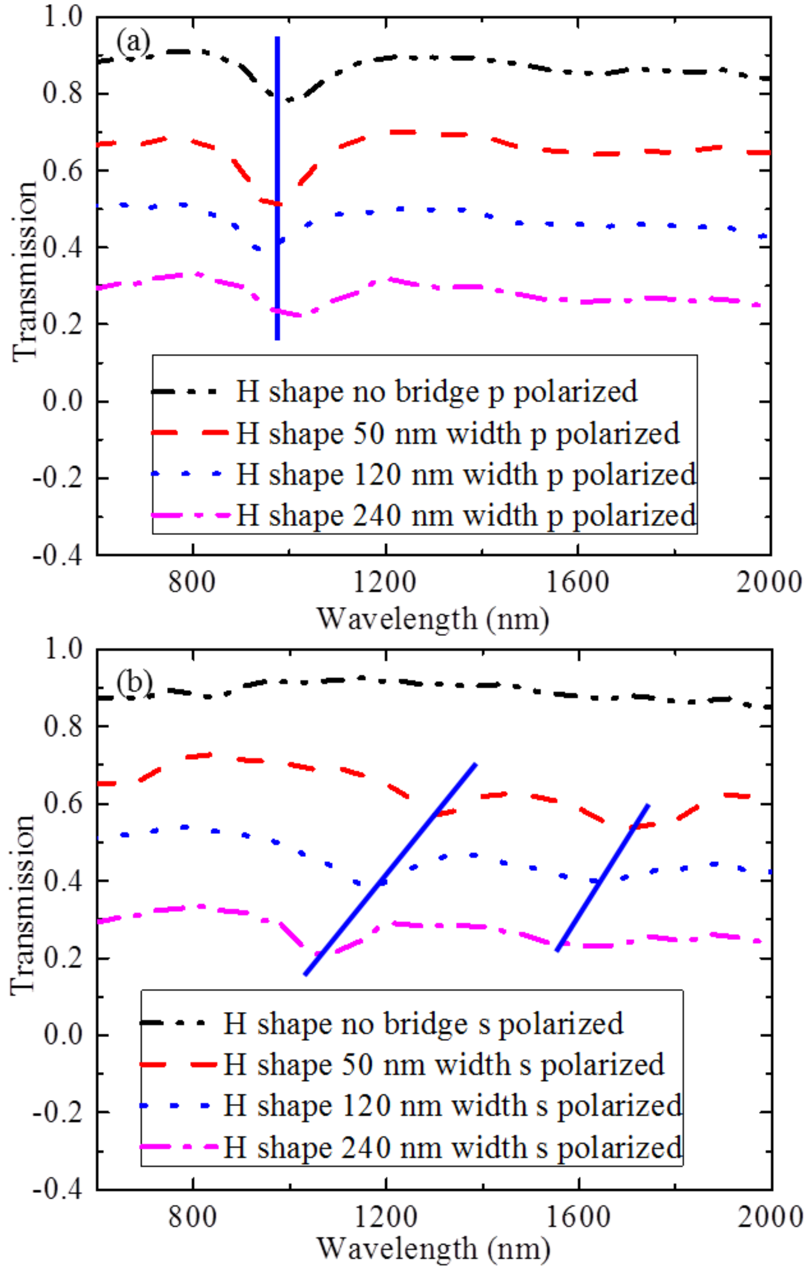

Fig. 4-11 Transmission measurement results of H shape nano antennas with various bridge widths are shown with two different polarized directions. The results are stacked for easy reading.

With the collected transmission data, the absorption amplitude was calculated after reflection measurement. The overall procedure included two steps. First, the baseline reflection measurement was conducted on standard oxidized silicon wafer. Second, the samples with and without H shape antennas were measured. After analysis by the developed model shown in Fig.

4-9, the reflection effect by those antennas was extracted from the subtraction of these two measurements. Fig. 4-12 shows the stacked reflection results after subtraction. There was no obvious peak in both p- and s- polarized directions. These results showed that the geometry difference of H shaper nano antennas did not contribute to the sample reflection.

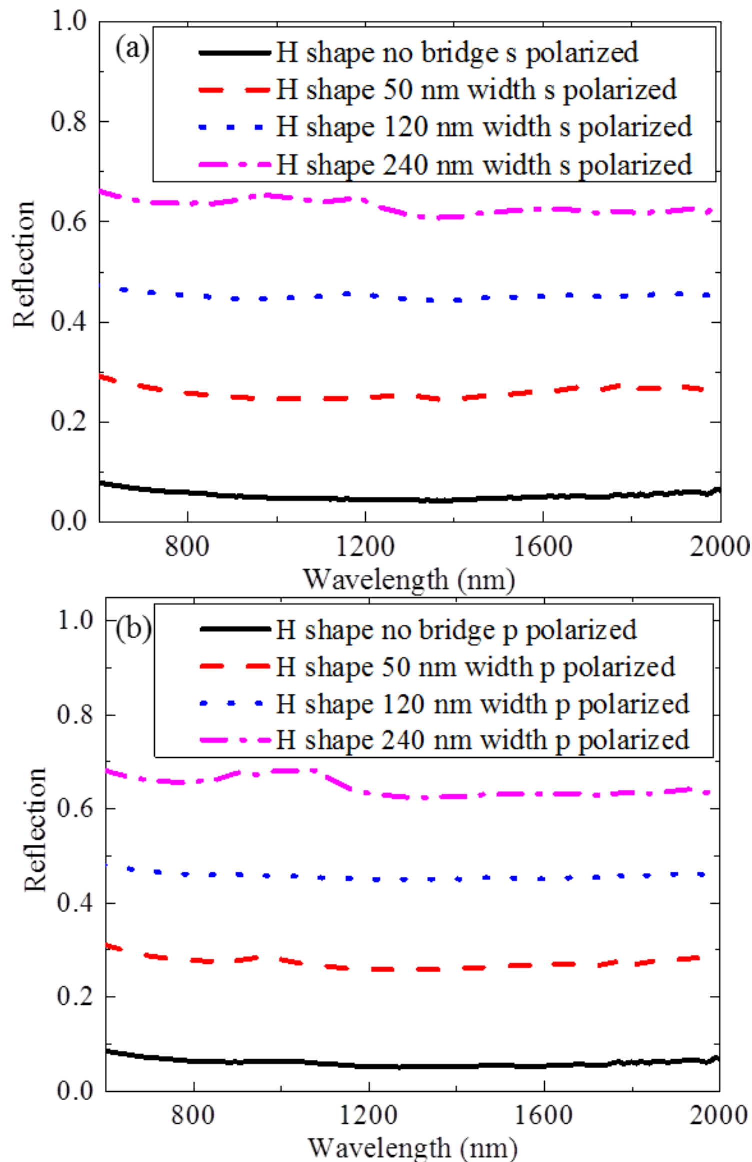

Fig. 4-12 Stacked reflection measurement results of H shape nano antennas with various bridge widths are shown with two different polarized directions.

After transmission and reflection measurements, the absorption curves were calculated shown in Fig. 4-13. For the p- polarized direction, the absorption peaks were nearly all located

at 1000 nm, which was mainly due to the plasmonic resonant by two parallel nanorods. For the s- polarized direction which was parallel to the bridge, the resonant wavelength had a blue shift from 1710 nm to 1020 nm with increased bridge widths from 50 nm to 240 nm. The resonant peak of the H shaped nano antenna without bridge was located at 830 nm.

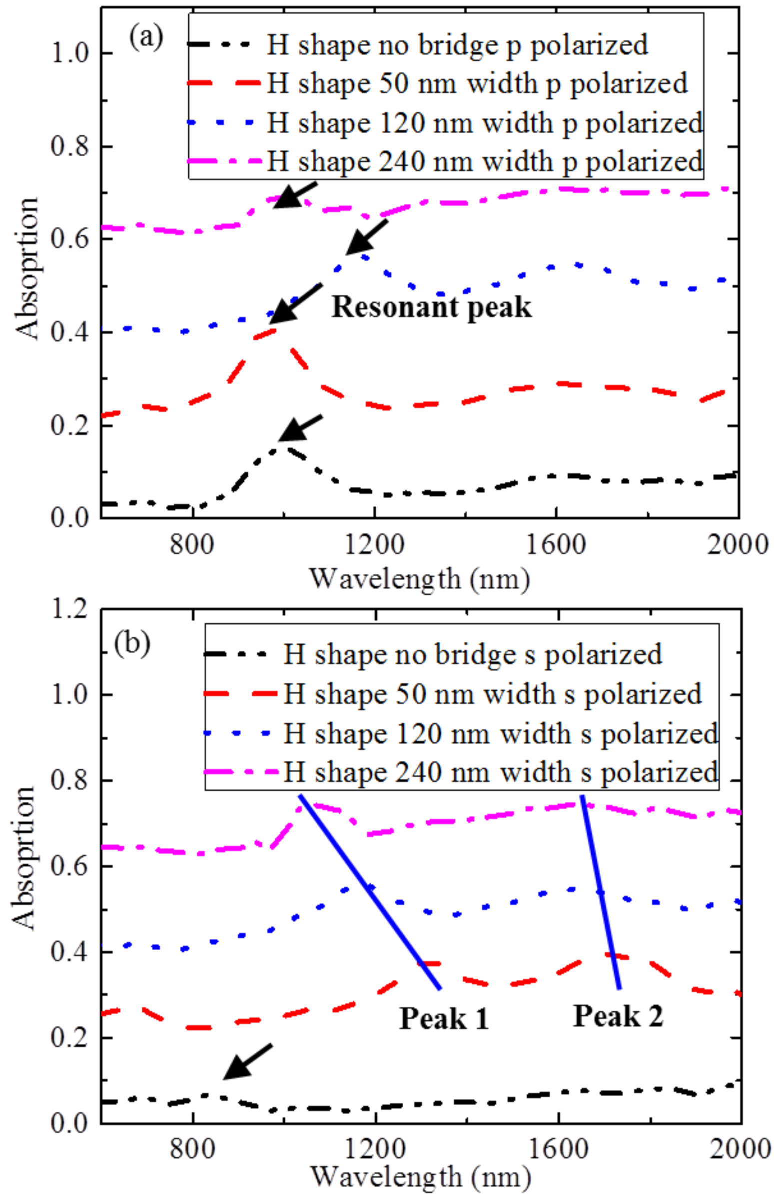

Fig. 4-13 Absorption measurement results of H shape nano antennas with various bridge widths are shown with two different polarized directions. The results are stacked for easy reading.

Compared to the constant maximum resonant wavelength of p- polarized direction, the maximum resonant peaks shifted more than 900 nm in the s- polarized direction. The possible reason was the coupling mechanism transition by the conductive bridge. In the p- polarized direction, which is vertical to the bridge, the resonant was caused by capacitive coupling between nanorods, as the peak positions did not change with or without bridge. However, the situation was totally different in the s- polarized direction with an applied bridge. The coupling changed from capacitive to conductive and showed a strong effect on resonant peak position due to the complete redistribution of the enhanced surface charges. With the wider bridge, the amplitude of redistributed surface charges decreased leading to the blue shift resonance. Moreover, the same explanation could be applied to absorption intensity. With the largest redistribution amplitude by narrower bridge at 50 nm, the maximized intensity was observed.

In order to verify these analysis, the measurement results were compared to published data [104] as shown in Fig. 4-14. Through the comparison, the measured resonant peaks were close to published resonant wavelength with different bridge widths. However, there was one more resonant peak of fabricated nano antennas at each bridge width value. The possible reason here was the slight geometry difference between the fabricated non-ideal structures and published structures shown as the inset of Fig. 4-14.

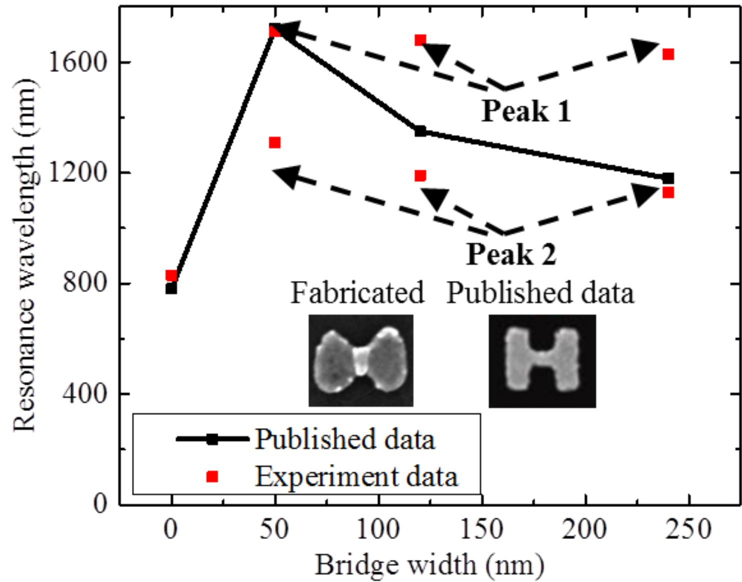

Fig. 4-14 Comparison of the maximum resonant wavelengths of s-polarized direction between measurement results and published data [104].

4.3 Device Fabrication

In the following experiment, all the GeSn substrates were from ASM International Company. The Ge and GeSn layers were grown on Si wafers using ASM Epsilon reduced pressure chemical vapor deposition (RPCVD) reactor. The Ge layer was utilized as virtual substrate for GeSn growth since the lattice mismatch between Ge and GeSn were relative smaller with lower threading dislocation densities. The deposition temperature was well below 450 ℃ which is compatible with standard CMOS processes. The as-grown sample was characterized by Rutherford backscattering spectrometry (RBS) and secondary ion mass spectroscopy (SIMS) to identify the Sn content for different growth condition. The $Ge_{1-x}Sn_x$ samples with x values at 0.009 and 0.07 were used in the following experiments. The corresponding GeSn layers were 327 nm and 240 nm thick, respectively. The detailed heteroepitaxial grown structures are shown in Fig. 4-15.

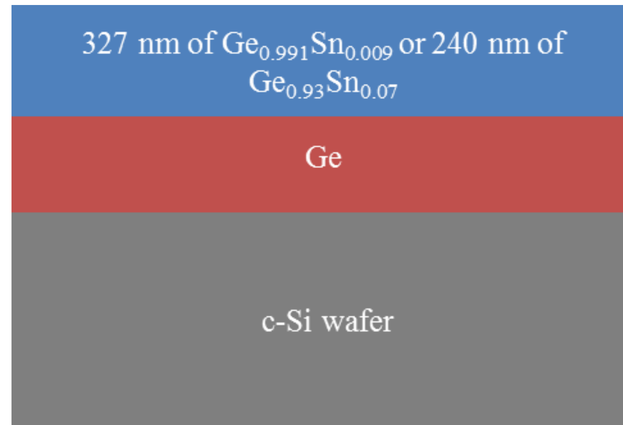

Fig. 4-15 It shows the detailed heteroepitaxial grown structures of Si/Ge/$Ge_{1-x}Sn_x$ with two different Sn contents (327 nm for x=0.009 and 240 nm for x=0.07).

The GeSn photoconductive photodetector fabrication process flow is shown below as Fig. 4-16. The process started with a standard solvent clean as in Chapter 2.3 with optional sonication on the ASM substrates (Fig. 4-16 (a)). After coating with photo resist AZ4330 the sample was spun at 3000 RPM with target thickness around 2 μm (Fig. 4-16 (b)). The pre-baking temperature was around 95 °C for 60 seconds. The photolithography process was performed on a Karl Suss 3" mask aligner with 10 seconds exposure time followed by 60 seconds developing time in commercial developer MF CD-26 from Shipley, which is 2.4% Tetramethylammonium hydroxide (TMAH) in water (Fig. 4-16 (c)). Hard baking at 120 °C for 1 minute was necessary to improve adhesion quality for following processing. After checked under microscope, the sample was loaded in the Plasma Therm SLR 720 Reactive Ion Etching (RIE) tool and etched with the parameters shown in Table 4-1 (Fig. 4-16 (d)). The sample was immersed in Remover PG solution for 20 minutes at 85 °C to remove the resist (Fig. 4-16 (e)). The available Ge/GeSn mesa sizes after etching were 2 mm × 2 mm, 1.5 mm × 1.5 mm, 1 mm × 1 mm, 750 μm × 750 μm, and 500 μm × 500 μm on each sample. To ensure no residual resist was left on the surface, an oxygen plasma asher was used. The photodetector electrodes patterning started with photolithography (Fig. 4-16 (f)), followed by developing (Fig. 4-16 (g)).

The developed area was filled by metals in thermal evaporator (Fig. 4-16 (h)). The 10 nm Cr and 200 nm Au were used in this case. The standard lift-off process was carried out to remove the resist and the metals (Fig. 4-16 (i)). The developed areas filled with metals were used as electrodes. Several alignment markers were patterned simultaneously for the following nanostructure patterning.

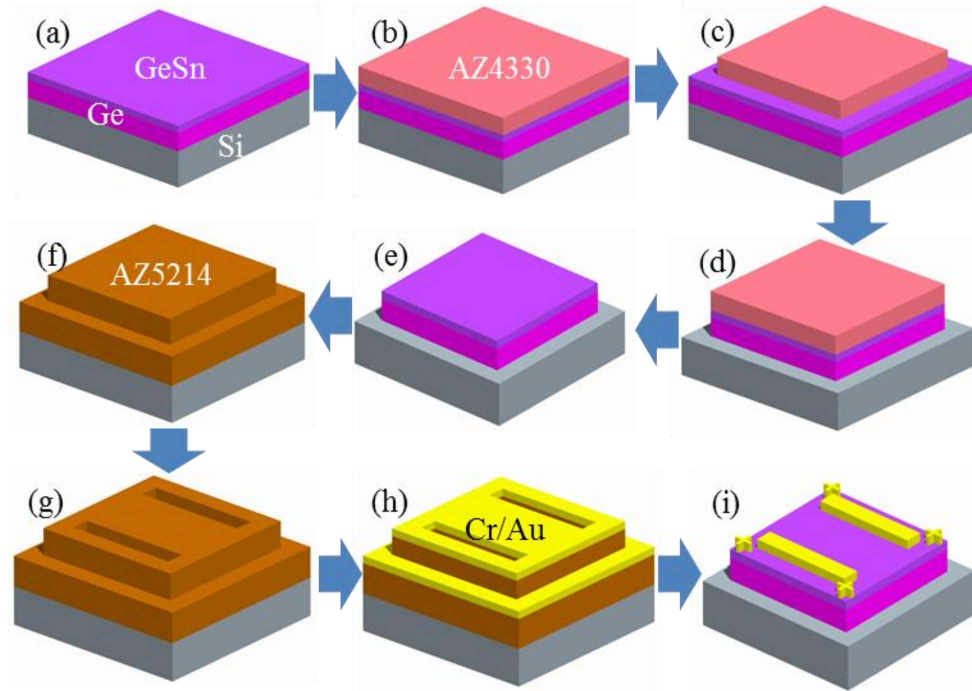

Fig. 4-16 This figure shows GeSn photodetector processing flow. The detailed process is: (a) Cleaning process of Si/Ge/GeSn substrate; (b) AZ4330 coating at 3000RPM and baking at 95 ℃; (c) Photolithography of AZ4330 and developing; (d) RIE of GeSn and Ge layers to form photodetector mesa; (e) AZ4330 removal by resist stripper; (f) AZ5214 coating at 3000RPM and baking at 95 ℃; (g) exposure, image reverse baking at 110 ℃ and developing; (h) metal deposition of 10 nm Cr and 200 nm Au; (i) lift-off process after metal deposition to removal resist.

	Power (W)	Pressure (mtorr)	Gas flow (sccm)	Etch rate (nm/min)	Etch time (minutes)
RIE	100	200	Ar (30), CF_4 (30)	50	25
Asher	150	NA	O_2 (200)	Very small	20

Table 4-1 The detailed parameters of dry etching and descum is shown.

The metallic nanostructures integrated GeSn photodetector was developed to investigate the plasmonic effects. The schematic processing flow is shown in Fig. 4-17. Compared to photolithography, electron beam lithography was used to pattern nanostructures due to the flexibility and high resolution. The detailed process also started with electron beam resist 4% PMMA coating followed by EBL exposure (Fig. 4-17 (b)). The EBL alignment resolution was proved within 10 nm shown in Chapter 2. After EBL developing (Fig. 4-17 (c)), the metals were deposited through thermal evaporation (Fig. 4-17 (d)). After overnight lift-off the interdigitated electrodes were patterned above the GeSn active layer.

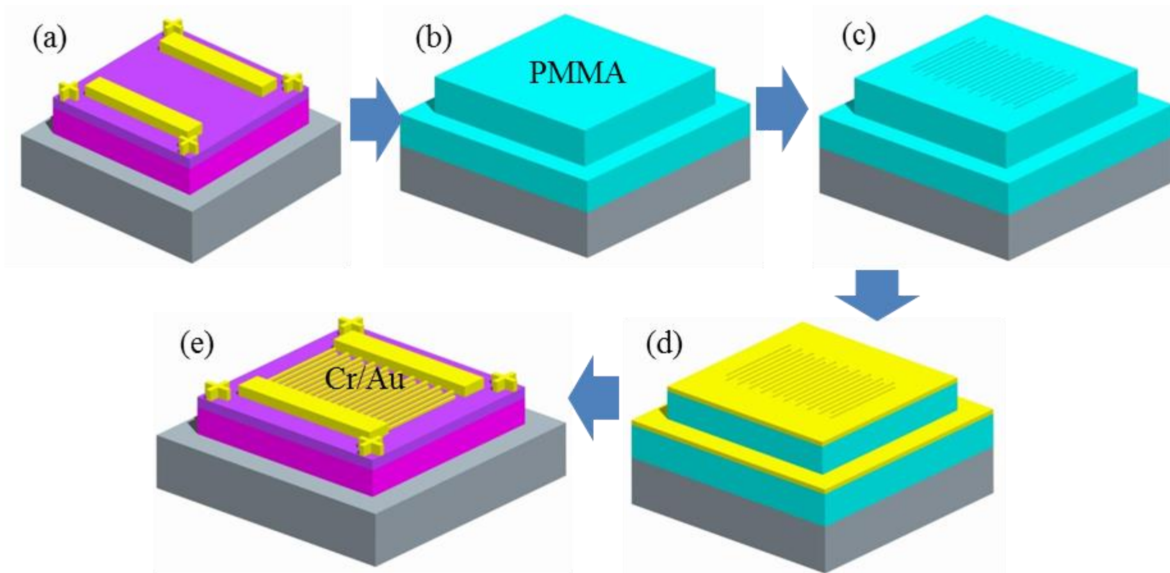

Fig. 4-17 This schematic processing flow demonstrates the metallic nanostructures integrated GeSn photodetector fabrication. The detailed process include: (a) Cleaning process of GeSn photodetector; (b) PMMA coating at 3000RPM and baking at 180 ℃; (c) Electron beam exposure with certain structure patterns; (d) metal deposition of 10 nm Cr and 50 nm Au; (i) lift-off process after metal deposition to removal PMMA.

4.4 Device Measurement Setup

In order to evaluate the electrical and optical properties of fabricated devices, different measurement techniques were utilized. The device current-voltage measurement setup was described in chapter 3. It was used to verify the contact type between GeSn and metals. The setup was based on a customized probe stage with temperature controlled at 25 ℃. A Keithley source measurement unit (SMU) 236 was connected to apply voltage and measure current from the device under test (DUT). The spectral response was characterized based on Fourier transform infrared (FTIR) spectrometer. The experiment setup was shown in Fig. 4-18. The spectrum was calibrated by using 1.55 μm InGaAs photodiode for responsivity. Pumped with certain values of injected current, the light from photodiode was passed through reflective mirrors and collected by a power meter. The corresponded photogenerated current was measured by pre-calibrated InGaAs photodetector. With the calculated photoresponsivity (A/W)

value at 1.55 μm, the absolute spectral response of fabricated GeSn photodetector was able to be measured.

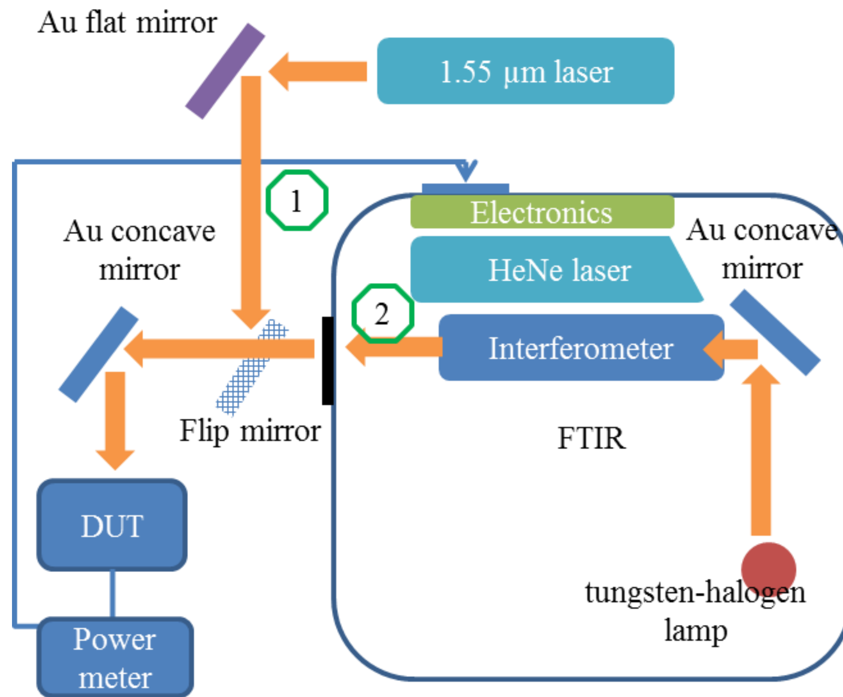

Fig. 4-18 This shows the schematic drawing of FTIR based IR photoresponse measurement setup. The absolute responsivity at 1.55 μm is measured with laser through optical pass 1. The real device measurement is based on FTIR through optical pass 2 without flip mirror.

4.5 Results and Discussion

The fabrication results of H shape nano antennas on ITO coated glass substrates have been presented in Chapter 3. The optical characterization results have been shown in Chapter 4.2. Beyond that, the fabricated H shape nano antennas integrated GeSn photodetectors are shown in Fig. 4-19. The Fig. 4-19 (a) shows the SEM top view of 500 μm × 500 μm size GeSn mesa of 7% Sn content GeSn photodetector with higher magnification SEM image of fabricated nano antennas shown in Fig. 4-19 (b). The geometry parameters of fabricated H shape nano antennas were identical to the structures used in optical characterization. The global contact was made of 10 nm Cr and 200 nm Au. The antennas were made by around 5 nm Cr and 30 nm Au.

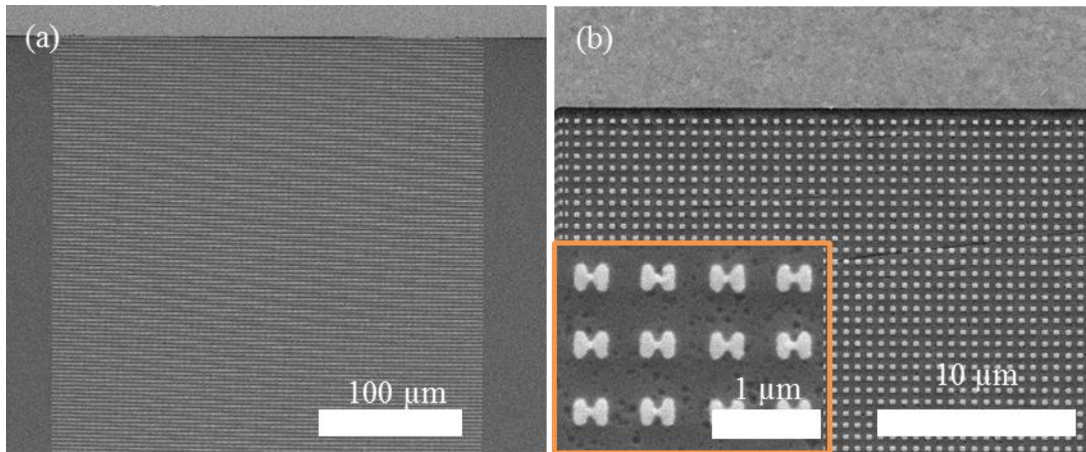

Fig. 4-19 The SEM images of fabricated H shape nano antennas integrated $Ge_{0.991}Sn_{0.009}$ photodetector. The figure (a) shows the overall image of detector on the mesa size of 500 μm × 500 μm. The figure (b) shows the magnified image of antennas. The bridge width shown in the inset is 50 nm and the spacing is 800 nm.

Through the photoresponse measurement, the electrical and optical effects of different metallic nano antennas were evaluated. As shown in Fig. 4-20, the photoresponse curves with different bridge widths were almost identical with less than 10% difference. Previously in the optical characterization of these antennas on ITO coated substrates, multiple absorption resonant peaks were observed with different geometry parameters. However, no obvious photoresponse differences were observed beyond that point. Considering this optical absorption improvement and negligible device performance improvement, the electrical improvement was considered in following device design.

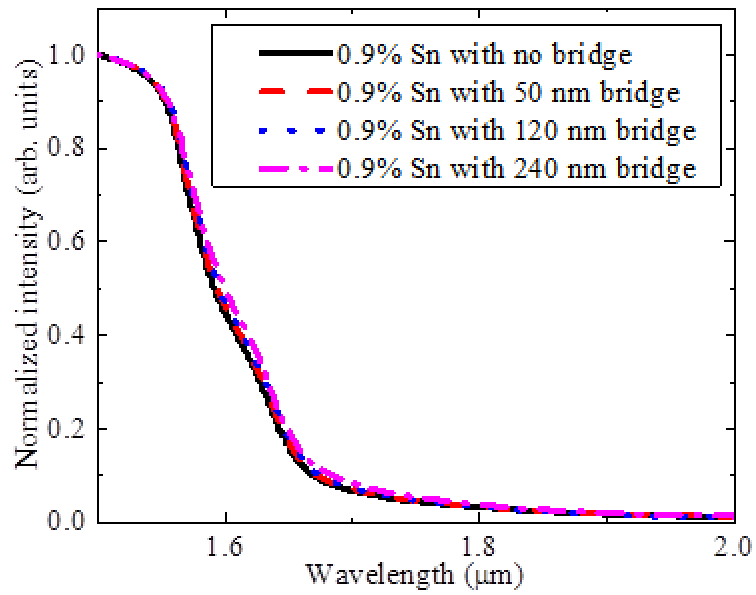

Fig. 4-20 The photoresponse curves of fabricated H shape nano antennas integrated GeSn photodetectors is shown here.

Chapter 5: Further Investigation

5.1 Introduction

Through the analysis of optical characterization results of H shape nano antennas on ITO coated glass substrates, multiple optical resonant peaks were observed in transmission and absorption measurements. This showed the optical improvement by those nano antennas. Meanwhile, the wavelength dependent photoresponse curves of integrating these nano antennas with GeSn photodetector showed negligible differences between various geometry parameters. Similar results were observed on the metallic fishnet integrated Schottky contact a-Si solar cell. Through optical simulation, an absorption improvement was obtained at 632 nm. However, no obvious improvement was found during photoresponse and QE measurement. Based on these two developed light detection devices, optical improvements with increased number of absorbed photons were achieved either through experiment or simulation. Nevertheless, through the photoresponse measurement, the photogenerated extra carriers could not be collected to form a higher current. In order to investigate the energy loss mechanisms, an metallic interdigitated electrodes integrated GeSn photodetectors were developed.

5.2 Device Fabrication Results

The device fabrication processing flow was shown in Fig. 4-17. The fabricated interdigitated electrodes integrated GeSn photodetectors were shown in Fig. 5-1. Fig. 5-1 (a) shows the SEM top view of 1 mm $\times$ 1 mm size GeSn mesa of 7% Sn content GeSn photodetector with zoom in SEM image of interdigitated fingers near global contact shown in Fig. 5-1 (b). The fabricated electrodes were 2 μm wide with 6 μm spacing between them. The global contacts were made of 10 nm Cr and 200 nm Au. Around 10 nm Cr and 50 nm Au were deposited as interdigitated electrodes.

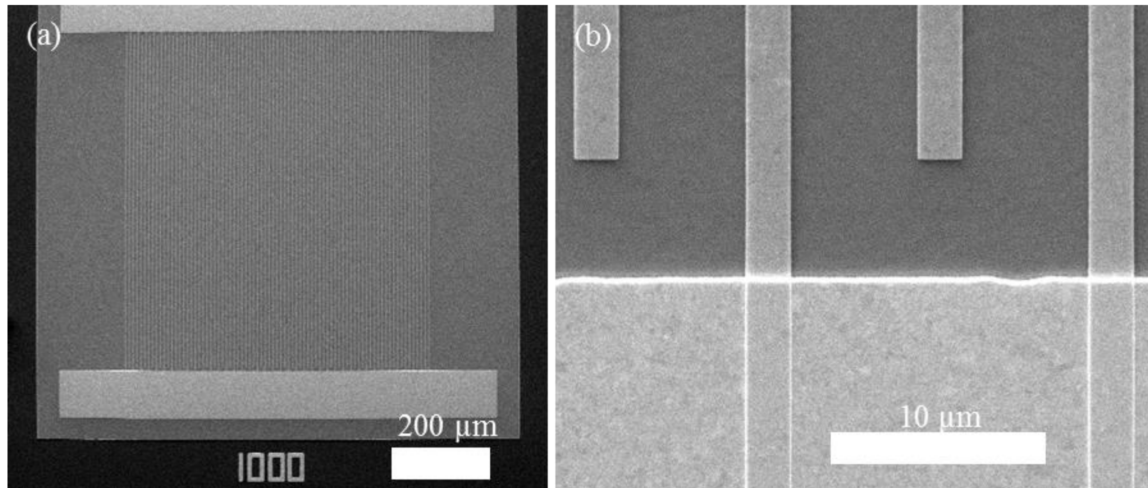

Fig. 5-1 It presents the SEM images of fabricated interdigitated electrodes integrated $Ge_{0.93}Sn_{0.07}$ photodetector. The figure (a) shows the overall image of detector on 1 mm × 1 mm mesa. The figure (b) shows the magnified image of electrodes. The width of electrode is 2 µm and the spacing between electrodes is 4 µm.

5.3 Characterization Results and Discussions

The electrical and optical characterization setups have been discussed in Chapter 3 and 4. Fig. 5-2 is the measured dark I-V curve that shows the ohmic contact between GeSn and Cr/Au layers. All the curves were taken using 500 µm × 500 µm mesas. The devices with interdigitated electrodes showed slightly lower resistance mainly due to the reduced distance between electrodes and increased metal resistance. The calculated resistance between electrodes on the same mesa was comparable with published data earlier [105]. With lower Sn content, the resistance was higher.

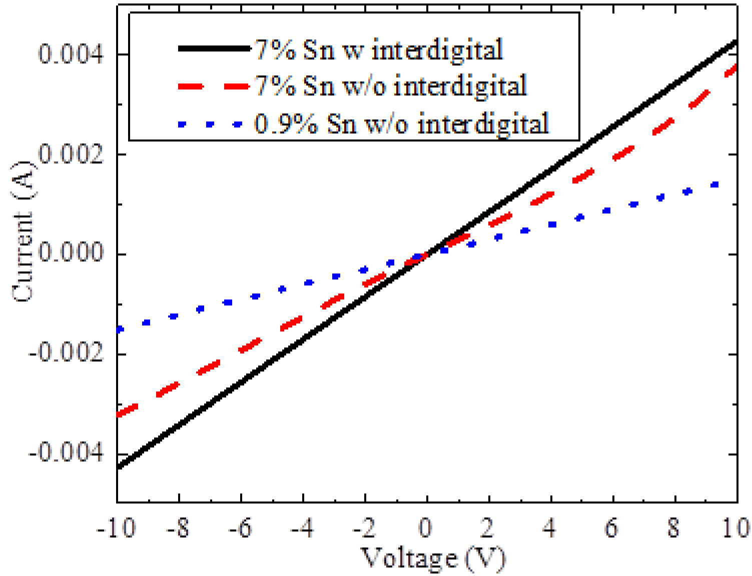

Fig. 5-2 The dark I-V measurement results show ohmic contact between metals and GeSn layer.

Based on the photoresponse measurement system, the IR photoresponse at room temperature of two Sn contents detectors (7% and 0.9%) were evaluated. As shown in Fig. 5-3, the photoresponse from 1.5 μm to 1.7 μm was observed from $Ge_{0.991}Sn_{0.009}$ detector. Following the same fabrication and measurement procedures, the $Ge_{0.93}Sn_{0.07}$ device showed a broader band response from 1.5 μm to 2.2 μm. The noisy spectral curve observed in the 7% Sn photodetector without interdigitated electrodes from 1.8 μm to 1.95 μm was due to atmospheric absorption. Nevertheless, the normalized photoresponse difference between the photodetectors with and without interdigitated fingers was negligible. Comparing to other developed metallic nanostructure integrated light detection devices, the increased photoresponse by metallic nanostructures was difficult to justify. However, the 7% Sn detector showed a broader response than the 0.9% Sn detector.

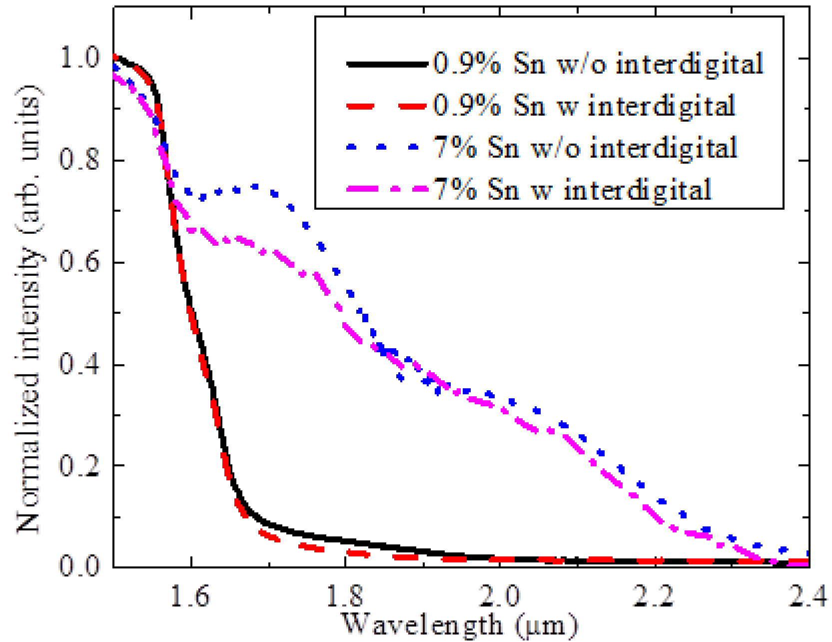

Fig. 5-3 The photoresponse comparison of fabricated $Ge_{1-x}Sn_x$ (x=0.009 and x=0.07) based photodetectors is shown here. The device performance with and without interdigitated electrodes is also presented.

Furthermore, compared to similar devices published before with 1.3 μm SiO_2 as a passivation layer on top [105], the fabricated photodetectors here showed broader response up to 2.2 μm (Fig. 5-4). Since SiO_2 absorbed light dramatically starting from 2 μm, the future passivation layers of GeSn photodetectors need to be optimized.

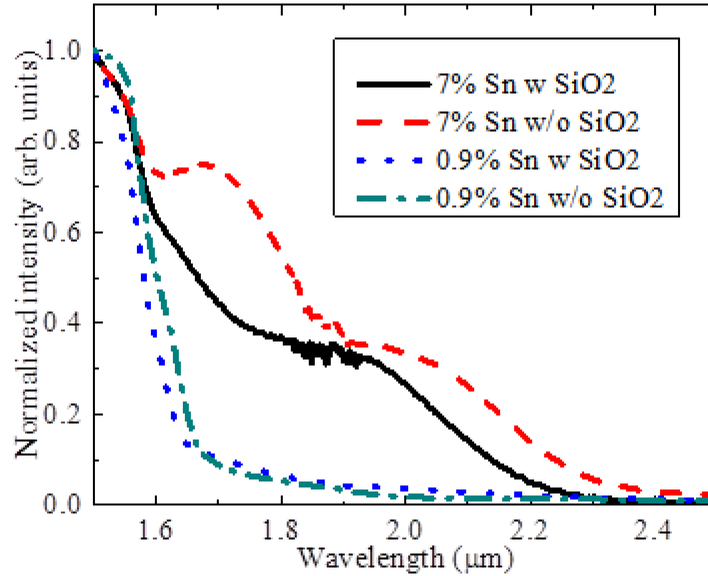

Fig. 5-4 The comparison shows a slightly broader response of the detector without SiO_2 as passivation layer.

In order to quantify the device performance, the AC responsivity values were measured at room temperature (RT) at 1.55 μm on 0.9% and 7% Sn content GeSn photodetectors with and without interdigitated electrodes, respectively. With the measured incident light power and the change of current, the absolute values of responsivity were calculated. As shown in Fig. 5-5, with integrated interdigitated electrodes both devices showed six times higher responsivity values at RT. With increased bias voltage up to 0.8 V, the responsivity values were higher up to 70 μA/W.

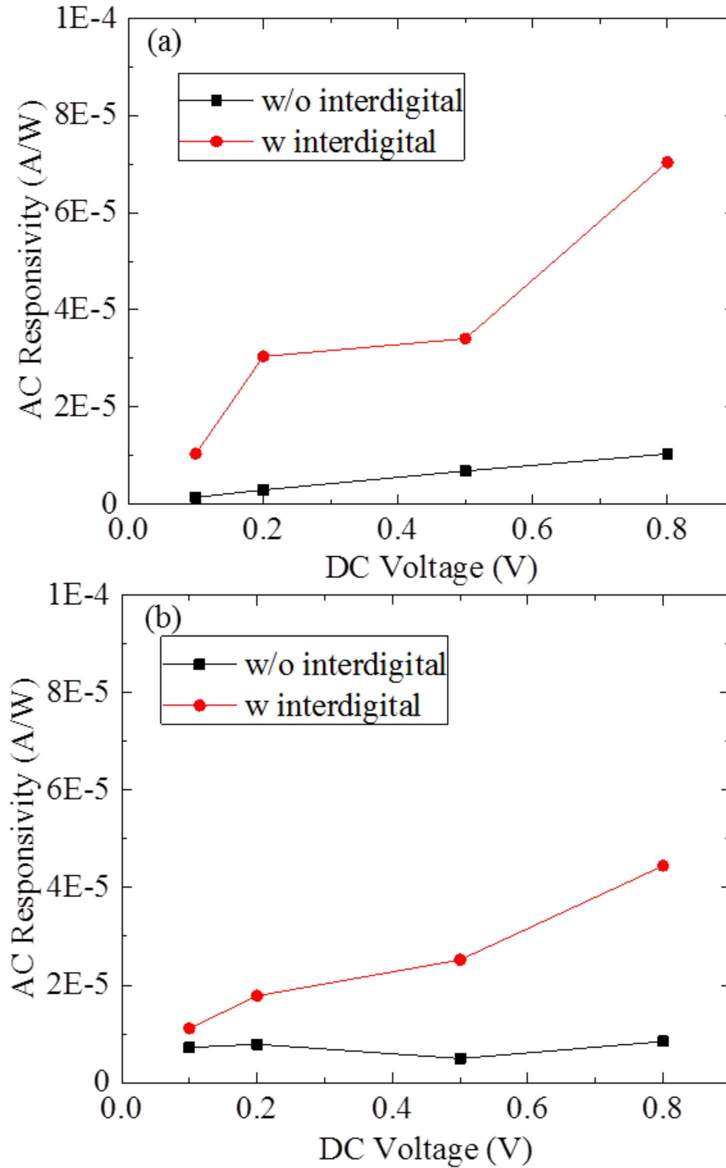

Fig. 5-5 The AC responsivity of $Ge_{0.991}Sn_{0.009}$ (a) and $Ge_{0.93}Sn_{0.07}$ (b) photodetectors with and without interdigitated electrodes are shown at 1.55 μm at room temperature.

Considering the shot noise, the specific detectivity (D^*) values were calculated at RT at 1.55 μm on 0.9% and 7% Sn content GeSn photodetectors shown in Fig. 5-6. Comparing the devices with and without interdigitated electrodes, the higher responsivity and detectivity values of interdigitated electrodes integrated devices were achieved by 6 μm between interdigitated electrodes. With this smaller gap between electrodes, the carrier transit time became shorter leading increased responsivity.

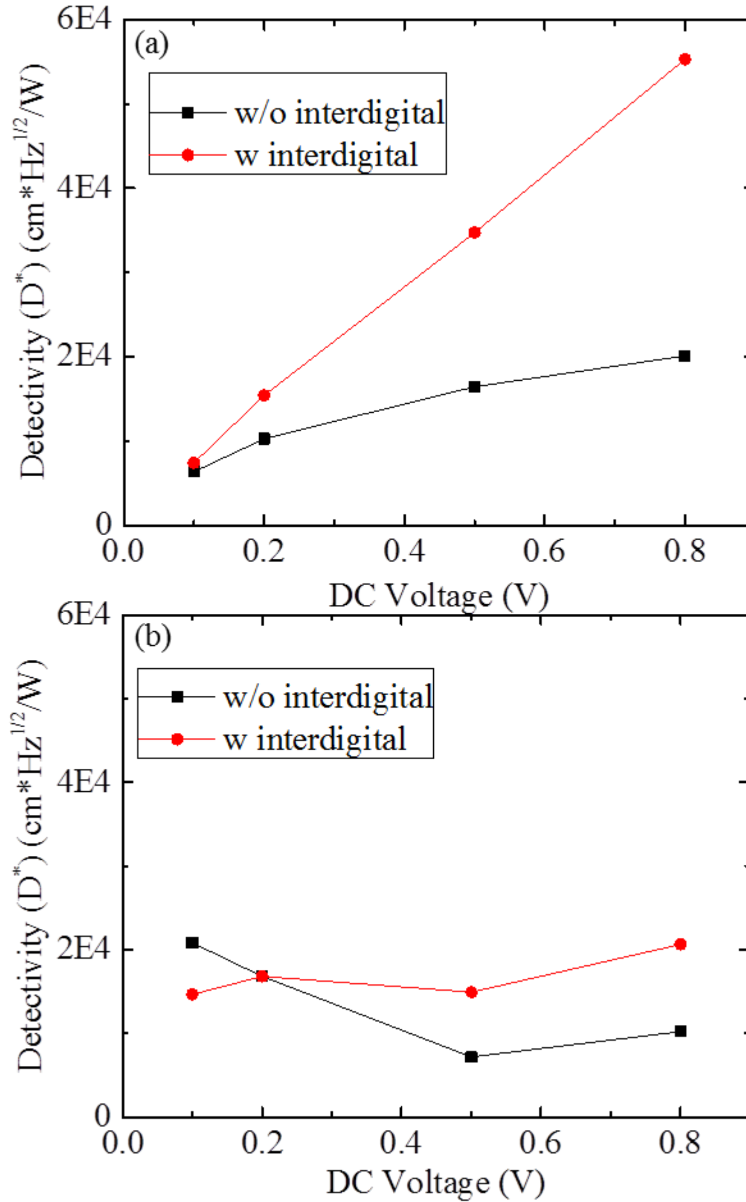

Fig. 5-6 The specific detectivity of $Ge_{0.991}Sn_{0.009}$ (a) and $Ge_{0.93}Sn_{0.07}$ (b) photodetectors with and without interdigitated electrodes are shown at 1.55 μm at room temperature.

On the other hand, with decreased temperature, the photon generated carrier lift time increased improving the device responsivity performance. As shown in Fig. 5-7, the wavelength dependent photoresponse measurement showed one thousand times improvement from 300K to 100K both for 0.9% and 7% Sn content GeSn photodetectors. Furthermore, the response wavelength extended to 2.2 μm on 7% Sn content device.

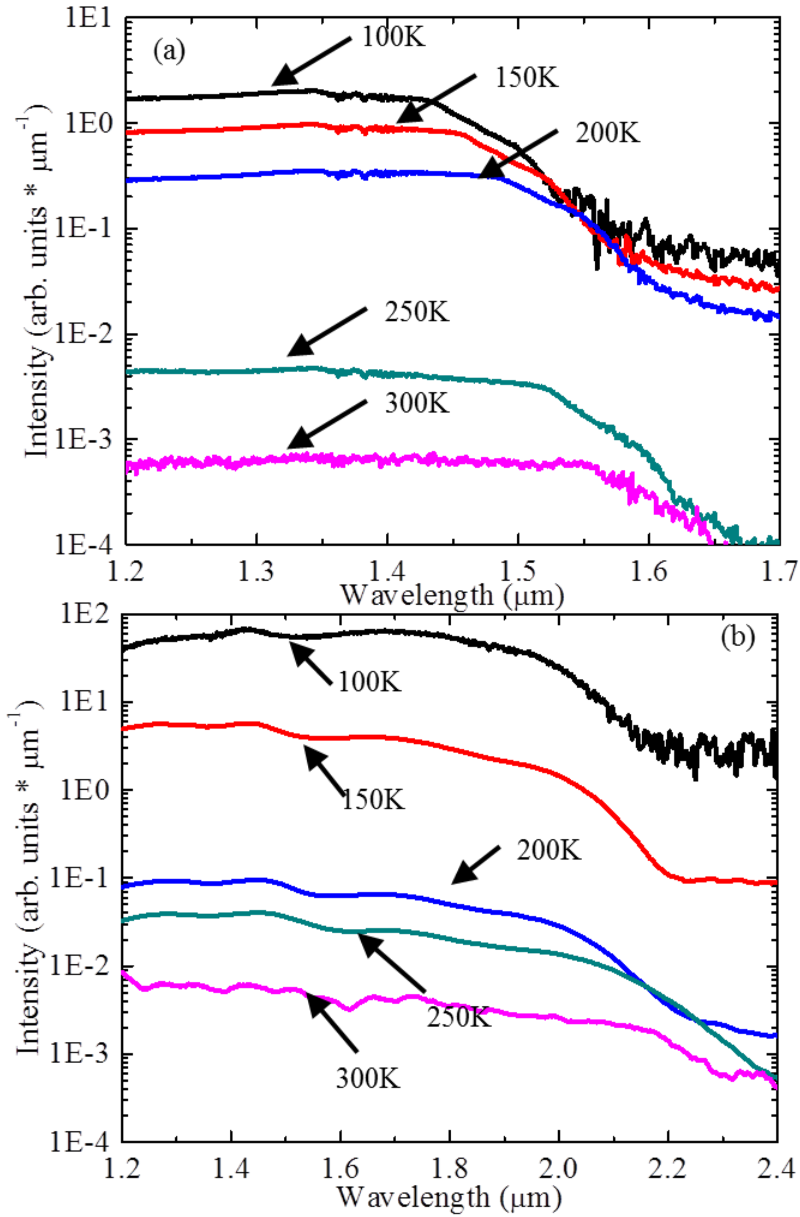

Fig. 5-7 The temperature dependent photoresponse of interdigitated electrodes integrated $Ge_{0.991}Sn_{0.009}$ (a) and $Ge_{0.93}Sn_{0.07}$ (b) photodetectors are shown.

Through the quantified responsivity (Fig. 5-8) and specific detectivity (Fig. 5-9) measurements, two hundred times higher values were achieved on the 7% Sn device from 300K to 100K. For the 0.9% Sn device, the maximum responsivity and specific detectivity were observed around 200K. The reason for this was the band gap increases with decreased temperature so that the corresponding absorption edge shifted to shorter wavelength. The

measured maximum value of photoresponsivity was around 0.0085 A/W for 7% Sn GeSn detector at 0.8V bias voltage at 100K.

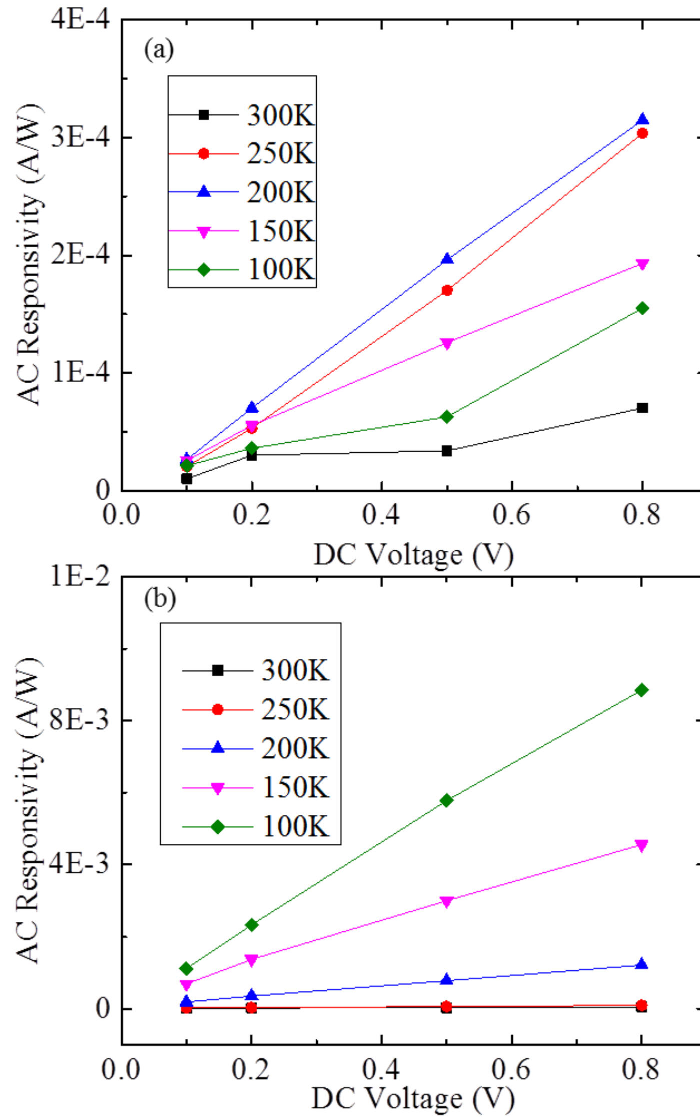

Fig. 5-8 The temperature dependent AC responsivity of interdigitated electrodes integrated $Ge_{0.991}Sn_{0.009}$ (a) and $Ge_{0.93}Sn_{0.07}$ (b) photodetectors are shown at 1.55 μm.

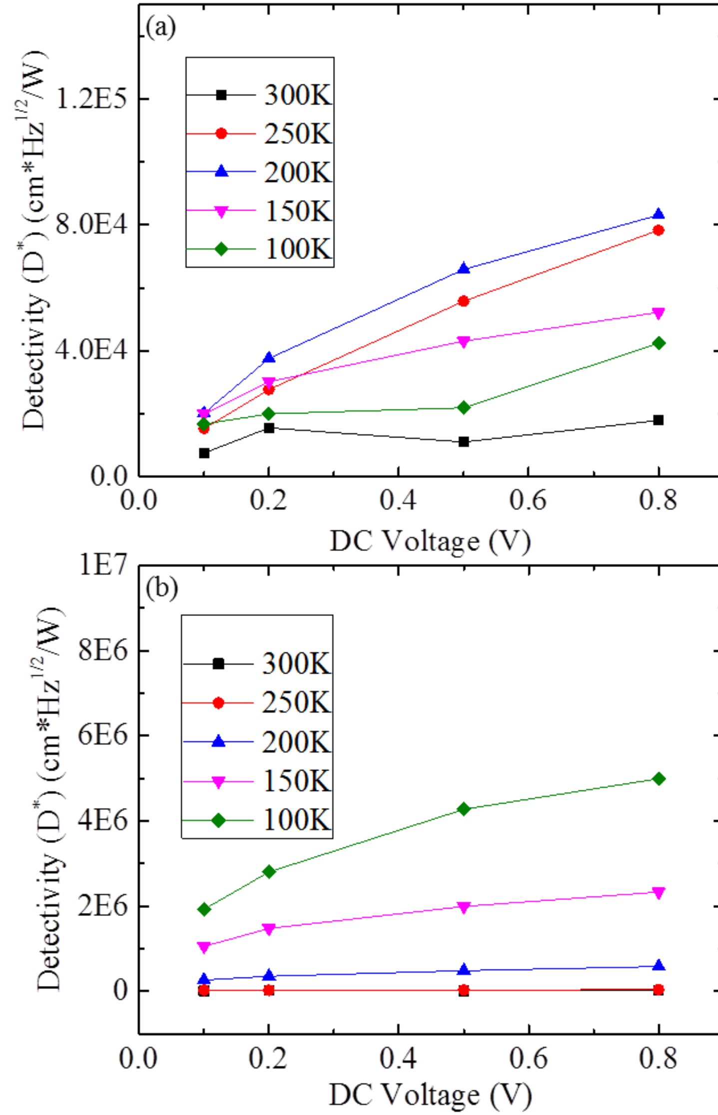

Fig. 5-9 The temperature dependent specific detectivity of interdigitated electrodes integrated $Ge_{0.991}Sn_{0.009}$ (a) and $Ge_{0.93}Sn_{0.07}$ (b) photodetectors are shown at 1.55 μm.

Through the temperature dependent optical characterization, the major energy loss mechanism in fabricated metallic nanostructures light detection devices is shown. With increased carrier life time by decreased temperature, the device responsivity increased. The large surface recombination led to the negligible photoresponse improvement in previous fabricated metallic fishnet integrated Schottky contact a-Si solar cell and metallic H shape nano antennas integrated GeSn photodetectors. In the first solar cell device, although absorption

improvements were observed through optical simulation, the device measurement results did not show clear evidence. The photogenerated carriers could not be collected even by a 2D fully connected metallic fishnet electrode due to the fairly large surface recombination rate. For the H shape nano antennas integrated detectors, multiple resonant peaks were observed through optical characterization of antennas. But the wavelength dependent photoresponse measurement did not reflect these peaks. However, with the metallic interdigitated electrodes integrated GeSn photodetector shown in this chapter, the photogenerated current dramatically increased both at RT and with temperature dependent measurements compared to regular detectors without interdigitated electrodes. At RT, with reduced carrier transit time and surface recombination by interdigitated electrodes, the responsivity was improved six times higher. With decreased temperature, the carrier life time increased further to reduce the surface recombination, improving the device responsivity values.

Chapter 6: Conclusions and Future Work

This dissertation presents the tasks of developing fabrication processes of metallic nanostructures, and integrating with innovative light detection devices. The integrated devices considered not only the better optical absorption but also the electrical perspective of photon generated carrier collection efficiency improvement.

To provide integration of metallic nanostructures with light detection devices, the fabrication processes on various substrates including c-Si, a-Si, ITO and glasses were first developed. High quality nanostructures were achieved with minimum feature sizes of 20 nm gap and 45 nm line width. The achieved alignment error was less than 10 nm. Beyond the fabrication processes development, a single horizontal Si nanowire device was developed as a device integration platform to characterize material and device properties. Beyond that, this platform could be easily transferred to other 2D devices such as Graphene, ZnO and carbon nanotube.

Further, considering the physics of light detection devices, both the optical absorption and electrical carrier transport were considered to evaluate the light detection device performance. It is the first time the metallic fishnet integrated Schottky contact a-Si solar cell was studied to investigate the improved device performance by reducing the surface recombination loss and decreasing the transit time of photon generated carriers. Meanwhile, the metallic fishnet nanostructure was utilized as a light trapping structure and interconnected top contact electrode simultaneously. Although the measurement results did not reach the expectation, possible improvements might be made through improved material quality of a-Si and device structures.

Third, the metallic H shape nano antennas integrated GeSn photodetectors were first developed. Through optical characterization of fabricated antennas on ITO coated glass substrates, several absorption resonant peaks in infrared range were observed with different H shape bridge widths. With larger bridge widths, the resonant peak shifted to shorter wavelengths. After integrating these antennas on GeSn photodetectors, the wavelength dependent photoresponse was conducted with negligible difference of various H shape bridge widths.

Furthermore, based on the results analysis of fabricated light detection devices, metallic interdigitated electrodes integrated GeSn photodetectors were developed with Sn composition of 0.9% and 7%, respectively. Compared to devices with and without interdigitated electrodes, six times higher responsivity value at room temperature with interdigitated electrodes have been achieved at 1.55 μm, both with $Ge_{0.93}Sn_{0.07}$ and $Ge_{0.991}Sn_{0.009}$. Through temperature dependent measurement, the photoresponse values of interdigitated electrodes integrated devices were one thousand times higher at 100K than at 300K for both Sn contents devices. The corresponded responsivity value rose to two hundred times higher at 100K for the same Sn content device.

In this dissertation, it was the first time to integrate and characterize metallic nanostructures integrated intrinsic a-Si and GeSn based light detection devices, respectively. Considering not only the absorption improvement, but the photon generated carriers transport provided the optimized interdigitated electrodes as the top contact in GeSn based photodetectors. The achieved photoresponsivity was six times higher at room temperature and twelve hundred times higher at 100K comparing to the detector without interdigitated electrodes.

In future, considering both the optical and electrical improvement, an appropriate device platform is required to integrate with metallic nanostructures maximizing both the light trapping

effect and carrier collection efficiency. The GeSn based light detection devices might be one promising candidate for next generation low cost, near and mid infrared photodetectors.

References

[1] D. M. Schaadt, B. Feng, and E. T. Yu, "Enhanced semiconductor optical absorption via surface plasmon excitation in metal nanoparticles," *Applied Physics Letters,* vol. 86, p. 063106, 2005.

[2] L. Tang, D. A. Miller, A. K. Okyay, J. A. Matteo, Y. Yuen, K. C. Saraswat, and L. Hesselink, "C-shaped nanoaperture-enhanced germanium photodetector," *Optics letters,* vol. 31, pp. 1519-1521, 2006.

[3] S. Pillai, K. R. Catchpole, T. Trupke, and M. A. Green, "Surface plasmon enhanced silicon solar cells," *Journal of Applied Physics,* vol. 101, p. 093105, 2007.

[4] K. R. Catchpole and A. Polman, "Design principles for particle plasmon enhanced solar cells," *Applied Physics Letters,* vol. 93, p. 191113, 2008.

[5] K. Nakayama, K. Tanabe, and H. A. Atwater, "Plasmonic nanoparticle enhanced light absorption in GaAs solar cells," *Applied Physics Letters,* vol. 93, pp. 121904-121904-3, 2008.

[6] F. J. Beck, A. Polman, and K. R. Catchpole, "Tunable light trapping for solar cells using localized surface plasmons," *Journal of Applied Physics,* vol. 105, p. 114310, 2009.

[7] V. E. Ferry, M. A. Verschuuren, H. B. T. Li, R. E. I. Schropp, H. A. Atwater, and A. Polman, "Improved red-response in thin film a-Si: H solar cells with soft-imprinted plasmonic back reflectors," *Applied Physics Letters,* vol. 95, pp. 183503-183503-3, 2009.

[8] V. E. Ferry, J. N. Munday, and H. A. Atwater, "Design considerations for plasmonic photovoltaics," *Advanced Materials,* vol. 22, pp. 4794-4808, 2010.

[9] G. Mie, "Beiträge zur Optik trüber Medien, speziell kolloidaler Metallösungen," *Annalen der physik,* vol. 330, pp. 377-445, 1908.

[10] S. R. J. Brueck, V. Diadiuk, T. Jones, and W. Lenth, "Enhanced quantum efficiency internal photoemission detectors by grating coupling to surface plasma waves," *Applied Physics Letters,* vol. 46, p. 915, 1985.

[11] K. Berthold, R. A. Hopfel, and E. Gornik, "Surface plasmon polariton enhanced photoconductivity of tunnel junctions in the visible," *Applied Physics Letters,* vol. 46, pp. 626-628, 1985.

[12] S. Hayashi, K. Kozaru, and K. Yamamoto, "Enhancement of photoelectric conversion efficiency by surface plasmon excitation: A test with an organic solar cell," *Solid state communications,* vol. 79, pp. 763-767, 1991.

[13] T. Kume, S. Hayashi, and K. Yamamoto, "Enhancement of photoelectric conversion efficiency in copper phthalocyanine solar cell by surface plasmon excitation," *Japanese journal of applied physics,* vol. 32, pp. 3486-3492, 1993.

[14] T. Kume, S. Hayashi, H. Ohkuma, and K. Yamamoto, "Enhancement of photoelectric conversion efficiency in copper phthalocyanine solar cell: white light excitation of surface plasmon polaritons," *Japanese journal of applied physics,* vol. 34, pp. 6448-6451, 1995.

[15] O. Stenzel, A. Stendal, K. Voigtsberger, and C. Von Borczyskowski, "Enhancement of the photovoltaic conversion efficiency of copper phthalocyanine thin film devices by incorporation of metal clusters," *Solar energy materials and solar cells,* vol. 37, pp. 337-348, 1995.

[16] T. Wakamatsu, K. Saito, Y. Sakakibara, and H. Yokoyama, "Enhanced photocurrent in organic photoelectric cells based on surface plasmon excitations," *Japanese journal of applied physics,* vol. 34, pp. L1467-L1469, 1995.

[17] S. C. Kitson, W. L. Barnes, and J. R. Sambles, "Full Photonic Band Gap for Surface Modes in the Visible," *Physical Review Letters,* vol. 77, p. 2670, 1996.

[18] H. R. Stuart and D. G. Hall, "Absorption enhancement in silicon‐on‐insulator waveguides using metal island films," *Applied Physics Letters,* vol. 69, pp. 2327-2329, 1996.

[19] M. Westphalen, U. Kreibig, J. Rostalski, H. Lüth, and D. Meissner, "Metal cluster enhanced organic solar cells," *Solar energy materials and solar cells,* vol. 61, pp. 97-105, 2000.

[20] S. A. Maier, M. L. Brongersma, P. G. Kik, S. Meltzer, A. A. G. Requicha, and H. A. Atwater, "Plasmonics—a route to nanoscale optical devices," *Advanced Materials,* vol. 13, pp. 1501-1505, 2001.

[21] C. Eisele, C. E. Nebel, and M. Stutzmann, "Periodic light coupler gratings in amorphous thin film solar cells," *Journal of Applied Physics,* vol. 89, pp. 7722-7726, 2001.

[22] M. Moskovits, "Surface-enhanced spectroscopy," *Reviews of Modern Physics,* vol. 57, p. 783, 1985.

[23] C. F. Bohren and D. R. Huffman, *Absorption and scattering of light by small particles*: John Wiley & Sons, 1983.

[24] K. Kneipp, Y. Wang, H. Kneipp, L. T. Perelman, I. Itzkan, R. R. Dasari, and M. S. Feld, "Single molecule detection using surface-enhanced Raman scattering (SERS)," *Physical review letters,* vol. 78, p. 1667, 1997.

[25] S. Schultz, D. R. Smith, J. J. Mock, and D. A. Schultz, "Single-target molecule detection with nonbleaching multicolor optical immunolabels," *Proceedings of the National Academy of Sciences,* vol. 97, pp. 996-1001, 2000.

[26] T. A. Taton, C. A. Mirkin, and R. L. Letsinger, "Scanometric DNA array detection with nanoparticle probes," *Science,* vol. 289, pp. 1757-1760, 2000.

[27] K. Li, M. I. Stockman, and D. J. Bergman, "Self-similar chain of metal nanospheres as an efficient nanolens," *Physical review letters,* vol. 91, p. 227402, 2003.

[28] X. Zhang and Z. Liu, "Superlenses to overcome the diffraction limit," *Nature materials,* vol. 7, pp. 435-441, 2008.

[29] H. Ditlbacher, J. R. Krenn, G. Schider, A. Leitner, and F. R. Aussenegg, "Two-dimensional optics with surface plasmon polaritons," *Applied Physics Letters,* vol. 81, pp. 1762-1764, 2002.

[30] W. L. Barnes, A. Dereux, and T. W. Ebbesen, "Surface plasmon subwavelength optics," *Nature,* vol. 424, pp. 824-830, 2003.

[31] N. Engheta, "Circuits with light at nanoscales: optical nanocircuits inspired by metamaterials," *Science,* vol. 317, pp. 1698-1702, 2007.

[32] D. Derkacs, S. H. Lim, P. Matheu, W. Mar, and E. T. Yu, "Improved performance of amorphous silicon solar cells via scattering from surface plasmon polaritons in nearby metallic nanoparticles," *Applied Physics Letters,* vol. 89, p. 093103, 2006.

[33] L. Tang, S. E. Kocabas, S. Latif, A. K. Okyay, D.-S. Ly-Gagnon, K. C. Saraswat, and D. A. B. Miller, "Nanometre-scale germanium photodetector enhanced by a near-infrared dipole antenna," *Nature Photonics,* vol. 2, pp. 226-229, 2008.

[34] L. Cao, J.-S. Park, P. Fan, B. Clemens, and M. L. Brongersma, "Resonant germanium nanoantenna photodetectors," *Nano letters,* vol. 10, pp. 1229-1233, 2010.

[35] F.-F. Ren, K.-W. Ang, J. Song, Q. Fang, M. Yu, G.-Q. Lo, and D.-L. Kwong, "Surface plasmon enhanced responsivity in a waveguided germanium metal-semiconductor-metal photodetector," *Applied physics letters,* vol. 97, pp. 091102-091102-3, 2010.

[36] F.-F. Ren, K.-W. Ang, J. Ye, M. Yu, G.-Q. Lo, and D.-L. Kwong, "Split bull's eye shaped aluminum antenna for plasmon-enhanced nanometer scale germanium photodetector," *Nano letters,* vol. 11, pp. 1289-1293, 2011.

[37] A. N. Broers, "Resolution limits for electron-beam lithography," *IBM Journal of Research and Development,* vol. 32, pp. 502-513, 1988.

[38] T. H. P. Chang, "Proximity effect in electron ‐ beam lithography," *Journal of Vacuum Science & Technology,* vol. 12, pp. 1271-1275, 1975.

[39] D. Drouin, A. R. Couture, D. Joly, X. Tastet, V. Aimez, and R. Gauvin, "CASINO V2. 42—A Fast and Easy ‐ to ‐ use Modeling Tool for Scanning Electron Microscopy and Microanalysis Users," *Scanning,* vol. 29, pp. 92-101, 2007.

[40] D. C. Joy, *Monte Carlo modeling for electron microscopy and microanalysis* vol. 25: Oxford University Press New York, 1995.

[41] J. Nabity, "Nanometer Pattern Generation System," http://www.jcnabity.com/.

[42] A. B.-N. M. C. Facility, "FEI XL-30 ESEM." vol. 2014, 2014.

[43] F. Yu, "Electron Beam Lithography (JEOL JBX-5500ZD)." vol. 2014, 2014.

[44] JEOL, *JEOL JBX 5500 Series Operation Guide*, 2013.

[45] I. Utke, P. Hoffmann, and J. Melngailis, "Gas-assisted focused electron beam and ion beam processing and fabrication," *Journal of Vacuum Science & Technology B: Microelectronics and Nanometer Structures,* vol. 26, p. 1197, 2008.

[46] "xT Nova NanoLab User's Manual," *FEI Company,* 2006.

[47] L. Ji and V. V. Varadan, "Fishnet metastructure for efficiency enhancement of a thin film solar cell," *Journal of Applied Physics,* vol. 110, p. 043114, 2011.

[48] "Deep Reactive Ion Etching," *High Density Electronics Center (HiDEC) at University of Arkansas,* 2013.

[49] D. L. Pulfrey and R. F. McOuat, "Schottky‐barrier solar‐cell calculations," *Applied Physics Letters,* vol. 24, p. 167, 1974.

[50] D. E. Carlson, C. R. Wronski, A. R. Triano, and R. E. Daniel, "Solar cells using Schottky barriers on amorphous silicon," in *12th Photovoltaic Specialists Conference*, 1976, pp. 893-895.

[51] J. A. Willemen, "Modelling of amorphous silicon single- and multi-junction solar cells." vol. Ph.D: Delft University of Technology, 1998.

[52] S. L. Chuang, *Physics of photonic devices*: John Wiley & Sons, 2009.

[53] D. Ding, S. R. Johnson, S. Q. Yu, S. N. Wu, and Y. H. Zhang, "A semi-analytical model for semiconductor solar cells," *Journal of Applied Physics,* vol. 110, pp. 123104-123104-17, 2011.

[54] H. D. L. Huang, T. Pham, M. Young, H. Naseem, H. Hamza Abu-Safe, X. Yang, S.-Q. Yu, "Amorphous Silicon Solar Cells Using Metallic Fishnet Nanostructures Simultaneously for Schottky Contact and Plasmonics Enhancement," in *Photovoltaic Specialist Conference (PVSC)*, Tampa, FL, 2013.

[55] M. S. Haque, H. A. Naseem, and W. D. Brown, "Interaction of aluminum with hydrogenated amorphous silicon at low temperatures," *Journal of Applied Physics,* vol. 75, p. 3928, 1994.

[56] C. R. Wronski, D. E. Carlson, and R. E. Daniel, "Schottky‐barrier characteristics of metal‐amorphous‐silicon diodes," *Applied Physics Letters,* vol. 29, p. 602, 1976.

[57] D. K. Schroder, *Semiconductor material and device characterization*: John Wiley & Sons, 2006.

[58] S. Gupta, "Germanium-Tin (GeSn) Technology." vol. PhD: STANFORD UNIVERSITY, 2013.

[59] H. Kawanami, "Heteroepitaxial technologies of III–V on Si," *Solar energy materials and solar cells,* vol. 66, pp. 479-486, 2001.

[60] D. Nam, D. Sukhdeo, S.-L. Cheng, A. Roy, K. C.-Y. Huang, M. Brongersma, Y. Nishi, and K. Saraswat, "Electroluminescence from strained germanium membranes and implications for an efficient Si-compatible laser," *Applied physics letters,* vol. 100, p. 131112, 2012.

[61] J. Liu, X. Sun, D. Pan, X. Wang, L. C. Kimerling, T. L. Koch, and J. Michel, "Tensile-strained, n-type Ge as a gain medium for monolithic laser integration on Si," *Optics express,* vol. 15, pp. 11272-11277, 2007.

[62] R. E. Camacho-Aguilera, Y. Cai, N. Patel, J. T. Bessette, M. Romagnoli, L. C. Kimerling, and J. Michel, "An electrically pumped germanium laser," *Optics express,* vol. 20, pp. 11316-11320, 2012.

[63] B. Dutt, D. S. Sukhdeo, D. Nam, B. M. Vulovic, Z. Yuan, and K. C. Saraswat, "Roadmap to an efficient germanium-on-silicon laser: strain vs. n-type doping," *Photonics Journal, IEEE,* vol. 4, pp. 2002-2009, 2012.

[64] R. W. Olesinski and G. J. Abbaschian, "The Ge− Sn (Germanium− Tin) system," *Bulletin of Alloy Phase Diagrams,* vol. 5, pp. 265-271, 1984.

[65] R. F. C. Farrow, D. S. Robertson, G. M. Williams, A. G. Cullis, G. R. Jones, I. M. Young, and P. N. J. Dennis, "The growth of metastable, heteroepitaxial films of α-Sn by metal beam epitaxy," *Journal of Crystal Growth,* vol. 54, pp. 507-518, 1981.

[66] J. Piao, R. Beresford, T. Licata, W. I. Wang, and H. Homma, "Molecular-beam epitaxial growth of metastable GeSn alloys," *Journal of Vacuum Science & Technology B: Microelectronics and Nanometer Structures,* vol. 8, p. 221, 1990.

[67] J. L. Reno and L. L. Stephenson, "Effect of growth conditions on the stability of α - Sn grown on CdTe by molecular beam epitaxy," *Applied physics letters,* vol. 54, pp. 2207-2209, 1989.

[68] S. Takeuchi, Y. Shimura, O. Nakatsuka, S. Zaima, M. Ogawa, and A. Sakai, "Growth of highly strain-relaxed GeSn/virtual Ge by a Sn precipitation controlled compositionally step-graded method," *Applied physics letters,* vol. 92, p. 231916, 2008.

[69] S. Su, W. Wang, B. Cheng, G. Zhang, W. Hu, C. Xue, Y. Zuo, and Q. Wang, "Epitaxial growth and thermal stability of Ge1− xSnx alloys on Ge-buffered Si (001) substrates," *Journal of Crystal Growth,* vol. 317, pp. 43-46, 2011.

[70] E. Kasper, J. Werner, M. Oehme, S. Escoubas, N. Burle, and J. Schulze, "Growth of silicon based germanium tin alloys," *Thin Solid Films,* vol. 520, pp. 3195-3200, 2012.

[71] H. Lin, R. Chen, Y. Huo, T. I. Kamins, and J. S. Harris, "Low-temperature growth of Ge 1− x Sn x thin films with strain control by molecular beam epitaxy," *Thin Solid Films,* vol. 520, pp. 3927-3930, 2012.

[72] R. R. Lieten, J. W. Seo, S. Decoster, A. Vantomme, S. Peters, K. C. Bustillo, E. E. Haller, M. Menghini, and J. P. Locquet, "Tensile strained GeSn on Si by solid phase epitaxy," *Applied physics letters,* vol. 102, p. 052106, 2013.

[73] M. Bauer, J. Taraci, J. Tolle, A. V. G. Chizmeshya, S. Zollner, D. J. Smith, J. Menendez, C. Hu, and J. Kouvetakis, "Ge–Sn semiconductors for band-gap and lattice engineering," *Applied physics letters,* vol. 81, p. 2992, 2002.

[74] G. Grzybowski, R. T. Beeler, L. Jiang, D. J. Smith, J. Kouvetakis, and J. Menéndez, "Next generation of Ge1− ySny (y= 0.01-0.09) alloys grown on Si (100) via Ge3H8 and SnD4: Reaction kinetics and tunable emission," *Applied physics letters,* vol. 101, p. 072105, 2012.

[75] R. F. Spohn and C. B. Richenberg, "Tin Deuteride (SnD4) Stabilization," *ECS Transactions,* vol. 50, pp. 921-927, 2013.

[76] B. Vincent, F. Gencarelli, H. Bender, C. Merckling, B. Douhard, D. H. Petersen, O. Hansen, H. H. Henrichsen, J. Meersschaut, and W. Vandervorst, "Undoped and in-situ B doped GeSn epitaxial growth on Ge by atmospheric pressure-chemical vapor deposition," *Applied physics letters,* vol. 99, p. 152103, 2011.

[77] F. Gencarelli, B. Vincent, L. Souriau, O. Richard, W. Vandervorst, R. Loo, M. Caymax, and M. Heyns, "Low-temperature Ge and GeSn Chemical Vapor Deposition using Ge2H6," *Thin Solid Films,* vol. 520, pp. 3211-3215, 2012.

[78] R. Soref, J. Kouvetakis, J. Tolle, and J. Menendez, "Advances in SiGeSn Technology," *Journal of Materials Research,* vol. 22, pp. 3281-3291, 2007.

[79] V. R. D'Costa, C. S. Cook, A. G. Birdwell, C. L. Littler, M. Canonico, S. Zollner, J. Kouvetakis, and J. Menéndez, "Optical critical points of thin-film Ge_ {1− y} Sn_ {y} alloys: A comparative Ge_ {1− y} Sn_ {y} / Ge_ {1− x} Si_ {x} study," *Physical Review B,* vol. 73, p. 125207, 2006.

[80] W.-J. Yin, X.-G. Gong, and S.-H. Wei, "Origin of the unusually large band-gap bowing and the breakdown of the band-edge distribution rule in the Sn_ {x} Ge_ {1− x} alloys," *Physical Review B,* vol. 78, p. 161203, 2008.

[81] V. R. D'Costa, Y. Fang, J. Mathews, R. Roucka, J. Tolle, J. Menéndez, and J. Kouvetakis, "Sn-alloying as a means of increasing the optical absorption of Ge at the C-and L-telecommunication bands," *Semiconductor Science and Technology,* vol. 24, p. 115006, 2009.

[82] R. Chen, H. Lin, Y. Huo, C. Hitzman, T. I. Kamins, and J. S. Harris, "Increased photoluminescence of strain-reduced, high-Sn composition Ge1− xSnx alloys grown by molecular beam epitaxy," *Applied physics letters,* vol. 99, pp. 181125-181125-3, 2011.

[83] R. Roucka, J. Mathews, R. T. Beeler, J. Tolle, J. Kouvetakis, and J. Menéndez, "Direct gap electroluminescence from Si/Ge1− ySny pin heterostructure diodes," *Applied physics letters,* vol. 98, p. 061109, 2011.

[84] R. Roucka, J. Xie, J. Kouvetakis, J. Mathews, V. D'Costa, J. Menéndez, J. Tolle, and S. Q. Yu, "GeSn photoconductor structures at 1.55 μm: From advanced materials to prototype devices," *Journal of Vacuum Science & Technology B: Microelectronics and Nanometer Structures,* vol. 26, p. 1952, 2008.

[85] J. Mathews, R. Roucka, J. Xie, S.-Q. Yu, J. Menéndez, and J. Kouvetakis, "Extended performance GeSn/Si (100) pin photodetectors for full spectral range telecommunication applications," *Applied physics letters,* vol. 95, p. 133506, 2009.

[86] L. Colace, M. Balbi, G. Masini, G. Assanto, H.-C. Luan, and L. C. Kimerling, "Si-based near infrared photodetectors operating at 10Gbit/s," *Journal of luminescence,* vol. 121, pp. 413-416, 2006.

[87] R. Roucka, J. Mathews, C. Weng, R. Beeler, J. Tolle, J. Menendez, and J. Kouvetakis, "High-performance near-IR photodiodes: a novel chemistry-based approach to Ge and Ge–Sn devices integrated on silicon," *Quantum Electronics, IEEE Journal of,* vol. 47, pp. 213-222, 2011.

[88] J. Werner, M. Oehme, M. Schmid, M. Kaschel, A. Schirmer, E. Kasper, and J. Schulze, "Germanium-tin pin photodetectors integrated on silicon grown by molecular beam epitaxy," *Applied physics letters,* vol. 98, p. 061108, 2011.

[89] S. Su, B. Cheng, C. Xue, W. Wang, Q. Cao, H. Xue, W. Hu, G. Zhang, Y. Zuo, and Q. Wang, "GeSn pin photodetector for all telecommunication bands detection," *Optics express,* vol. 19, pp. 6400-6405, 2011.

[90] D. Zhang, C. Xue, B. Cheng, S. Su, Z. Liu, X. Zhang, G. Zhang, C. Li, and Q. Wang, "High-responsivity GeSn short-wave infrared pin photodetectors," *Applied physics letters,* vol. 102, pp. 141111-141111-4, 2013.

[91] R. Roucka, R. Beeler, J. Mathews, M.-Y. Ryu, Y. Kee Yeo, J. Menéndez, and J. Kouvetakis, "Complementary metal-oxide semiconductor-compatible detector materials with enhanced 1550 nm responsivity via Sn-doping of Ge/Si (100)," *Journal of Applied Physics,* vol. 109, pp. 103115-103115-9, 2011.

[92] A. Gassenq, F. Gencarelli, J. Van Campenhout, Y. Shimura, R. Loo, G. Narcy, B. Vincent, and G. Roelkens, "GeSn/Ge heterostructure short-wave infrared photodetectors on silicon," *Optics express,* vol. 20, pp. 27297-27303, 2012.

[93] G. Sun, R. A. Soref, and H. H. Cheng, "Design of an electrically pumped SiGeSn/GeSn/SiGeSn double-heterostructure midinfrared laser," *Journal of Applied Physics,* vol. 108, p. 033107, 2010.

[94] G. Sun, R. A. Soref, and H. H. Cheng, "Design of a Si-based lattice-matched room-temperature GeSn/GeSiSn multi-quantum-well mid-infrared laser diode," *Optics express,* vol. 18, pp. 19957-19965, 2010.

[95] G.-E. Chang, S.-W. Chang, and S. L. Chuang, "Strain-Balanced GezSn1-z-SixGeySn1-xy Multiple-Quantum-Well Lasers," *IEEE journal of quantum electronics,* vol. 46, pp. 1813-1820, 2010.

[96] J. Mathews, R. T. Beeler, J. Tolle, C. Xu, R. Roucka, J. Kouvetakis, and J. Menéndez, "Direct-gap photoluminescence with tunable emission wavelength in GeSn alloys on silicon," *Applied physics letters,* vol. 97, p. 221912, 2010.

[97] M. Oehme, E. Kasper, and J. Schulze, "GeSn Heterojunction Diode: Detector and Emitter in One Device," *ECS Journal of Solid State Science and Technology,* vol. 2, pp. R76-R78, 2013.

[98] H. H. Tseng, K. Y. Wu, H. Li, V. Mashanov, H. H. Cheng, G. Sun, and R. A. Soref, "Mid-infrared electroluminescence from a Ge/Ge 0.922 Sn 0.078/Ge double heterostructure pin diode on a Si substrate," *Applied physics letters,* vol. 102, pp. 182106-182106-4, 2013.

[99] J. P. Gupta, N. Bhargava, S. Kim, T. Adam, and J. Kolodzey, "Infrared electroluminescence from GeSn heterojunction diodes grown by molecular beam epitaxy," *Applied physics letters,* vol. 102, pp. 251117-251117-4, 2013.

[100] M. Oehme, K. Kostecki, T. Arguirov, G. Mussler, K. Ye, M. Gollhofer, M. Schmid, M. Kaschel, R. Korner, and M. Kittler, "GeSn heterojunction LEDs on Si substrates," *Photonics Technology Letters, IEEE,* 2014.

[101] S. Cho, R. Chen, S. Koo, G. Shambat, H. Lin, N. Park, J. Vuckovic, T. I. Kamins, B.-G. Park, and J. S. Harris, "Fabrication and Analysis of Epitaxially Grown Ge< formula formulatype=," *Photonics Technology Letters, IEEE,* vol. 23, pp. 1535-1537, 2011.

[102] R. Chen, S. Gupta, Y.-C. Huang, Y. Huo, C. W. Rudy, E. Sanchez, Y. Kim, T. Kamins, K. C. Saraswat, and J. S. Harris, "Demonstration of a Ge/GeSn/Ge Quantum-Well Microdisk Resonator on Silicon: Enabling high-quality Ge (Sn) materials for micro and nanophotonics," *Nano letters,* 2013.

[103] I. J. A. Woollam Co., *Guide to using WVASE32* 2010.

[104] N. Berkovitch and M. Orenstein, "Thin wire shortening of plasmonic nanoparticle dimers: the reason for red shifts," *Nano letters,* vol. 11, pp. 2079-2082, 2011.

[105] B. R. Conley, L. Huang, S. A. Ghetmiri, A. Mosleh, W. Du, G. Sun, R. Soref, J. Tolle, H. A. Naseem, and S.-Q. Yu, "Extended Infrared Absorption to 2.2 μm with Ge1-xSnx Photodetectors Grown on Silicon," in *Conference on Lasers and Electro-Optics (CLEO)*, San Jose, CA, USA, 2014, p. Submitted.

Appendix A: Description of Research for Popular Publication

Growing millions of tiny sunflowers on your watch

Nanotechnology is an amazing area in recent years. The molecule level manipulation excites various possible applications in our daily life. The wearable electronics is a huge market in near future.

One big challenge for these innovative electronics is the power supply. Conventional lithium battery has been widely used. However, the battery life is always a concern since it is a chemical battery with limited time. With better battery life time, the size will be bigger. Solar is a clean and almost endless energy supply. The limited energy conversion efficiency is the major issue preventing its wide application. With 1 cm $\times$ 1 cm solar panel, the converted energy might not enough to drive more sophisticated and precise electronics.

"Now think about if you have thousands of conventional tiny solar cells on 1 cm $\times$ 1 cm area, the collected energy will be more than enough to drive those portable electronics such as iPad, iPhone, etc". Instead of standard cell, these cells are integrated with various metallic nanostructures. However, how to fabricate those structures on such small area is the big challenge.

Similar to the sunflowers, these nanostructures are light sensitive. Instead of consistent facing to the sunshine, these structures can guide and manipulate light to collect more energy. So think about your watch has one small area fully occupied by these intensive structures. Moreover, the utilized solar power can drive your electronics all the time without one second stop. That is the final purpose of this dissertation to develop such a processing technique putting millions of nanostructures on 1 mm $\times$ 1 mm area and integrating on light detection devices for future electronics.

Appendix B: Executive Summary of Newly Created Intellectual Property

The objectives of this research were: (1) developing the fabrication process of metallic nanostructures on various substrates; (2) developing a universal device integration platform for 2D materials and devices; (3) developing the integration process with light detection devices including fishnet integrated Schottky contact intrinsic a-Si solar cell; (4) developing the metallic nano antennas integrated GeSn photodetectors; (5) developing the interdigitated electrodes integrated GeSn photodetectors to further investigate the device performance considering both electrical and optical optimization.

The newly created intellectual property in the current research is:

1. The fabrication process of single horizontal Si nanowire device as a universal device platform can be applied for other semiconductor 2D devices.

2. The 2D connected metallic fishnet structures as Schottky contact in thin film intrinsic material solar cell development.

3. The integration process of metallic nanostructures with GeSn photodetectors considering both electrical and optical optimization.

Appendix C: Potential Patent and Commercialization Aspects of listed Intellectual Property Items

C.1 Patentability of Intellectual Property

The three items listed were considered first from the perspective of whether or not the item could be patented.

1. The fabrication integration technique of single horizontal Si nanowire device as university 2D materials and device characterization platform. Similar device has been patented.
2. The 2D connected metallic fishnet structure integrated Schottky contact a-Si solar cell. The device concept is innovative which could be patented.
3. The metallic interdigitated electrodes integrated GeSn photodetectors is new and can be patented.

C.2 Commercialization prospects

The three items listed were then considered from the perspective of whether or not the item should be patented.

1. The fabrication and integration techniques can be applied on a universal semiconductor device platform to characterize the material properties such as ZnO nanowires, Graphene, molybdenum diselenide, etc. The potential product market is limited and not clear.
2. The idea of Schottky contact a-Si solar cell is good but the commercial application is really limited in PV industry.
3. It is the first time to integrate metallic nanostructures on GeSn photodetector. It can be applied further on other GeSn optoelectronic devices depending on the future material

and device research. Since GeSn based optoelectronic devices is under initial investigation, the future research and commercialized directions are not clear.

C.3 Possible Prior Disclosure of IP

The following items were discussed in a public forum or have published information that could impact the patentability of the listed IP.

1. The 2D device fabrication process has been reported by different researchers. However, the detailed steps may vary based on the fabricated devices.

2. The Schottky contact a-Si solar cell has been investigated and reported long time ago. The revisit integrated with fishnet nanostructure in this dissertation is only meaningful from device development perspective not from a product.

3. The integration process of metallic nanostructures has been reported on different substrates. Nevertheless, the integration process on GeSn is first proposed in this dissertation.

Appendix D: Broader Impacts of Research

The metallic nanostructures integrated GeSn photodetectors can be used to improve near and mid infrared light detection devices performance from both optical and electrical improvement consideration. With further optimized geometry parameters, the covered response wavelength can be adjustable so that GeSn could be a potential candidate as low cost, CMOS compatible, broadband group IV direct band gap infrared material and device system. Meanwhile, the possible hybrid thermoelectric and optoelectronic devices could be possible as next generation energy conversion devices.

Appendix E: Microsoft Project for Ph.D MicroEP Degree Plan

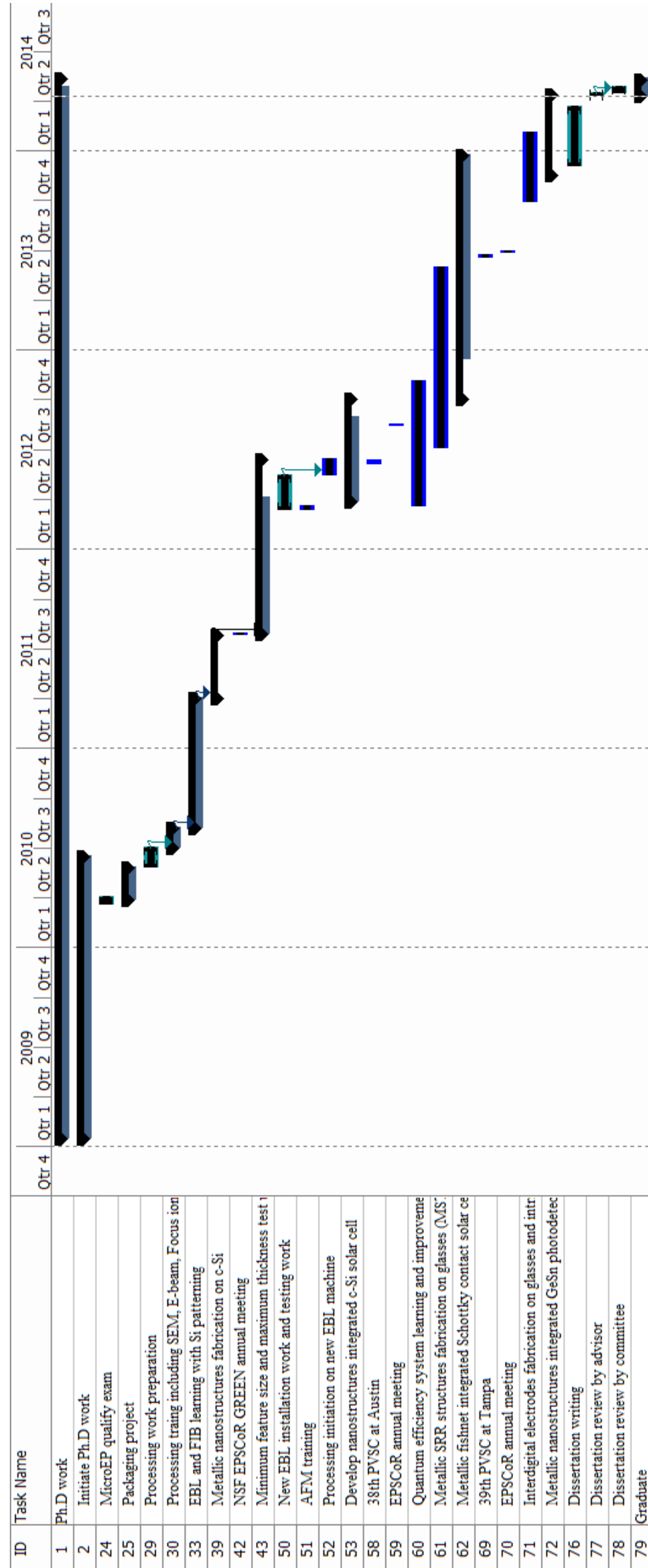

Appendix F: Identification of All Software Used in Research and Dissertation Generation

Computer 1

Model Number: Lenovo SL300

Serial Number: 2738A2U

Location: ENRC #2933

Owner: Dr. Shui-Qing (Fisher) Yu

Software 1: Windows XP, purchased by University of Arkansas with computer

Software 2: Microsoft Office, purchased by University of Arkansas site license

Computer 2

Model Number: Dell Insprion

Serial Number: N4110 6366622

Location: personal laptop

Owner: Liang Huang

Software 1: Windows 7, purchased by Liang Huang with computer

Software 2: Microsoft Office, purchased by Liang Huang

Software 3: Endnote X, purchased by Liang Huang

Software 4: Microsoft Project, purchased by MSDN Academy Alliance College of Engineering

Software 5: Origin 9.1, purchased by Liang Huang

Computer 3

Model Number: Gateway E-4200

Serial Number: 14137243

Location: ENRC #2933

Owner: Dr. Hameed Naseem

Software 1: Interactive Characterization Software, purchased by University of Arkansas

Software 2: Origin 7.0, purchased by University of Arkansas

Computer 4

Model Number: Gateway 2000

Serial Number: 8198929

Location: ENRC #2933

Owner: Dr. Hameed Naseem

Software 1: SpectraMax, purchased by University of Arkansas

Software 2: Origin 7.0, purchased by University of Arkansas

Appendix G: All Publications Published, Submitted and Planned

1. L. Huang, H. Deng, T. Pham, M. Young, H. Naseem, H. Hamza Abu-Safe, X. Yang, S.-Q. Yu, Amorphous Silicon Solar Cells Using Metallic Fishnet Nanostructures Simultaneously for Schottky Contact and Plasmonics Enhancement EBL, 2013 IEEE PVSC Conference (Tampa)

2. L. Huang, H.H. Abu-Safe, M. Young, S. Shumate, B. Newton, H. Naseem, S.-Q. Yu, Fabrication and Characterization of c-Si Solar Cells Integrated with Ordered Metallic Nanostructure Arrays, 2012 IEEE PVSC Conference (Austin)

3. B. Conley, L. Huang, S. Ghetmiri, A. Mosleh, W. Du, G. Sun, R. Soref, J. Tolle, H. Naseem, S.-Q Yu, Extended Infrared Absorption to 2.2 μm with Ge1-xSnx Photodetectors Grown on Silicon, 2014 CLEO

4. S. Ghetmiri, B. Conley, A. Mosleh, L. Huang, W. Du, A. Nazzal, G. Sun, R. Soref, J. Tolle, H. Naseem, S.-Q Yu, Photoluminescence from GeSn/Ge Heterostructure Microdisks with 6% Sn Grown on Si via CVD, 2014 CLEO

5. W. Du, S. Ghetmiri, A. Mosleh, B. Conley, L. Huang, A. Nazzal, R. Soref, G. Sun, J. Tolle, H. Naseem, S.-Q Yu, Investigation of Photoluminescence from Ge1-xSnx: A CMOS-Compatible Material Grown on Si via CVD

Appendix H: ANBP Group Fabrication Lot Number Definition

ANBP Group Fabrication Lot Number Definition

The lot number has following format: XXXXXXX

1. The first 'X' represents the device type.

Symbol	Definition	Symbol	Definition
V	VCSEL	**E**	Edge emitter Laser
R	RCLED	**L**	Edge emitter LED
T	Tunnel Junction	**M**	Mirror or simple EPI layer
C	Conventional surface emitting LED	**O**	Ohmic Contact Test device
X	Not specified, see the traveler	**N**	Nanowire device
S	Solar cell	**F**	Nano fabrication development
D	Detector	**P**	Photoconductor

2. The second 'X' represents the light emission direction. If the device is edge-emitting structure or non-light emitting test structure, then it represents device structure.

Symbol	Definition	Symbol	Definition
T	Top Emitting	**B**	Bottom Emitting
R	Ridge Defined Edge Emitter	**O**	Edge Emitter, Oxide Defined
P	P type layer	**N**	N type layer
X	Not specified, see the traveler	**S**	Simple Metal Deposition
I	Imprint Process	**K**	Schottky contact
V	For I-V measurement		

3. The third 'X' represents the key process

Symbol	Definition	Symbol	Definition
P	Plasma Etch	**R**	RIE Etch
W	Wet etch	**D**	Dielectric Layer Deposition
X	Not specified, see the traveler	**O**	Oxide confinement
L	Laser direct writing	**E**	E-beam lithography

4. The forth 'X' (number) distinguish major difference for same device Lot number.
For example, VTP1, VTP2 are both Lot number for VCSEL. But VTP1 is for quick VCSEL and VTP2 is for intra-cavity VCSEL.

5. The last three 'XXX' represent processing round number.

6. ANBP Lot number will be compatible with ASU and Lytek's number.

Appendix I: Processing Traveler of Metallic Nanostructures on Glass Substrates

Traveler, metallic nanostructures fabrication on glass substrate

FSE1001
LOT0001

NFORMATION IS CONFIDENTIAL AND PROPRIETARY TO UA ANBP GROUP AND S
NOT BE REPRODUCED OR OTHERWISE DISCLOSED
TO ANYONE OTHER THAN UA ANBP GROUP MEMBERS WITHOUT WRITTEN PERMISSION.

Fab Lot # FSE1001

Start Date: 09/03/2014
Due Date: 09/24/2012
Mask Set: No mask, electron beam direct writing
Purpose: Target on metallic nanostructures fabrication on glass substrate using PMMA by JEOL-5500ZD in HiDEC.
Lot#: Nano fabrication development, Simple metal deposition, E-beam lithography, 1(first attempt), 001(Round number)

Lot #	Wafer #	Growth #	Description
0001	NA		1 cm glass substrate

OP/LINK	DESCRIPTION	PARAMETER	ESTIMATED TIME
1	Sample Preparation		1 hour
2	E-beam lithography		4.0 hours
3	Metal deposition		2.0 hours
4	Lift-off		2 hour - overnight
			Total: 9 hour - overnight

Sample Preparation (Start)				
Date /Time	**1.1**	**Substrate size** ☐ _____cm X ______cm ☐ 2 inch wafer ☐ 4 inch wafer	Sample NO:_______________ Dicing saw or diamond scriber Type: ☐ glass	If ITO coated glass, ITO thickness: __________
	1.2	**Solvent Clean** ☐ Develop bench in photolithography room ☐ Solvent spray bottles ☐ Three waste bottles ☐ Three funnels	☐ Acetone, Methanol, IPA, DI water, N_2 Blow dry	

E-beam Lithography (Start)				
Date/ Time	**2.1**	☐ Hot plate ☐ Spinner check ☐ Spinner ☐ Nanospec	Set hot plate temperature @ 180°C wait for at least 10 minutes to stabilize ☐ Vacuum OK? ☐ Recipe OK? Recipe _____, _______rpm ☐ Change the bowl dedicated for EBL ☐ Clean the lid ☐ PMMA vial Concentration: ☐ 2% ☐ 4% ☐ 6% ☐ 8% ☐ 1.5 inch chuck ☐ Blue tape apply pressure w/ finger tweezers, 180 °C / 120 sec ☐ Double spin Si wafer Refractive index of PMMA: 1.485 (633 nm) Sample thickness______________(center)	

Date/ Time	2.2	**Metal Deposition (Edwards thermal 306T)** ☐ Pumping down ☐ Cr deposition	Pump down time:____________ min Base pressure:______________ mBar Reference value **Cr : 50 Å @ 0.2 Å /sec** Start current:_______________ Start pressure_______________mBar Start deposition rate:_________________ Å/sec End current:_______________ End pressure____________________mBar End deposition rate:_________________ Å/sec Thickness:____________________ Å	
	2.3	**Transportation**	☐ Non-transparent sample box	
	2.4	**E-beam exposure** ☐ System configuration ☐ Substrate ☐ Exposure preparation ☐ Exposure	☐ 50 KV ☐ Mode 2 (four lens) ☐ Piece cassette ☐ Aperture 2 Sample center position (cassette coordinate): X: __________mm; Y: __________mm Calibration file: _______________ Current: ________nA ☐ Calibration OK? Pattern file name: ________________________ ________________________ ________________________ ☐ Piece cassette exposure configuration Scheduled file name: ________________________ **The piece cassette center is at (0, -5000 µm) in exposure configuration coordinate!!** Base dose: ___________ $\mu C/cm^2$ ☐ Shot rank (check sample information page) Writing time: ___________min ☐ Writing OK?	

	2.5	**Cr Wet etching (Acid bench)**	Etchant: CEP-200 Estimate etching rate: 5 nm/sec Etching time: 30 sec Rinse with DI water ☐ Time: 30s ____________ ☐ Blow dry with nitrogen	
	2.6	**Develop (E-beam room)**	3:1 IPA:MIBK ☐ Time: __________ Rinse with IPA ☐ Time: __________	
	2.7	**Check with microscope**	OK?______	

Metal Deposition <u>(Start)</u>				
	3	**Metal Deposition (Edwards 306T)** ☐ Pumping down ☐ Cr deposition ☐ Au deposition	Pump down time:_____________ min Base pressure:_______________ mBar Reference value **<u>Cr : 20 Å @ 0.05 Å /sec</u>** Start current:_________________mA (in scale) Start pressure________________mBar Start deposition rate:__________________ Å/sec End pressure______________________mBar End deposition rate:__________________ Å/sec Thickness:______________________ Å Reference value **<u>Au : 150 Å @ 0.125 Å /sec</u>** Start current:_________________mA (in scale) Start pressure________________mBar Start deposition rate:__________________ Å/sec Start Temperature:________________ Start current:_________________mA (in scale) End pressure______________________mBar End deposition rate:__________________ Å/sec **End Temperature**:________________ Thickness:______________________ Å	

Lift-off (Start)				
Date/ Time	**4**	**Metal Liftoff** ☐ Solvent Hood ☐ Microscope	PMMA sample Remover PG (Place in ultrasonic bath if necessary) Temperature: Time: Acetone / Methanol / IPA / DI rinse Surface Cleanness ☐ Pass ☐ Fail Pattern OK? ☐ Pass ☐ Fail	

<table>
<tr><td colspan="6">Sample NO:</td></tr>
<tr><td colspan="6">Resist information</td></tr>
<tr><td>Type:</td><td colspan="2">Thickness:</td><td colspan="2">Spin speed:</td><td>Base dose:</td></tr>
<tr><td colspan="6">Pattern information</td></tr>
<tr><td colspan="2">Schedule file name:</td><td colspan="4">Total chip numbers (except marks):</td></tr>
<tr><td colspan="2">Scheduled writing pattern</td><td colspan="2">Chip NO</td><td colspan="2">Chip pattern name</td></tr>
<tr><td colspan="2" rowspan="8"></td><td colspan="2"></td><td colspan="2"></td></tr>
<tr><td colspan="2">Description</td><td colspan="2"></td></tr>
<tr><td colspan="2"></td><td colspan="2"></td></tr>
<tr><td colspan="2">Description</td><td colspan="2"></td></tr>
<tr><td colspan="2"></td><td colspan="2"></td></tr>
<tr><td colspan="2">Description</td><td colspan="2"></td></tr>
<tr><td colspan="2"></td><td colspan="2"></td></tr>
<tr><td colspan="2">Description</td><td colspan="2"></td></tr>
</table>

Chip number				
Scan step				
Shot rank				
Shot step				
Right dose after SEM				
Comments				
Chip number				
Scan step				
Shot rank				
Shot step				
Right dose after SEM				
Comments				

Job 1											
1	2	3	4	5	6	7	8	9	10	11	12
13	14	15	16	17	18	19	20	21	22	23	24
Job 2											
1	2	3	4	5	6	7	8	9	10	11	12
13	14	15	16	17	18	19	20	21	22	23	24
Job 3											
1	2	3	4	5	6	7	8	9	10	11	12
13	14	15	16	17	18	19	20	21	22	23	24
Job 4											
1	2	3	4	5	6	7	8	9	10	11	12
13	14	15	16	17	18	19	20	21	22	23	24
Job 5											
1	2	3	4	5	6	7	8	9	10	11	12
13	14	15	16	17	18	19	20	21	22	23	24
Job 6											
1	2	3	4	5	6	7	8	9	10	11	12
13	14	15	16	17	18	19	20	21	22	23	24
Job 7											
1	2	3	4	5	6	7	8	9	10	11	12
13	14	15	16	17	18	19	20	21	22	23	24
Job 8											
1	2	3	4	5	6	7	8	9	10	11	12
13	14	15	16	17	18	19	20	21	22	23	24

Appendix J: Processing Traveler of Single Horizontal Si Nanowire Device

Single horizontal Si nanowire device on SiO_2 (EBL)

NVE1001
LOT0001

<table>
<tr><td rowspan="2">NVE1001</td><td colspan="3">UA ANBP Group
ENRC 2933, Phone:479-575-5231</td></tr>
<tr><td>DOCUMENT NUMBER
00-0000-003</td><td>REVISION
A</td><td>PAGE
145 OF 194</td></tr>
<tr><td colspan="4">ORMATION IS CONFIDENTIAL AND PROPRIETARY TO UA ANBP GROUP AND SH
BE REPRODUCED OR OTHERWISE DISCLOSED
TO ANYONE OTHER THAN UA ANBP GROUP MEMBERS WITHOUT WRITTEN PERMISSION.</td></tr>
</table>

Fab Lot # NVE1001

Start Date: 02/14/12
Due Date: 02/17/12
Mask Set:
Purpose: Target for fabrication of single nanowire device using standard photolithography and electron beam lithography (EBL) processing flow.
Lot#:

Lot #	Wafer #	Growth #	Description
0001		N/A	Product lot

OP/LINK	DESCRIPTION	PARAMETER	ESTIMATED TIME
0	Wafer Pre-clean (RCA)		1.0 hour
2	Metal deposition	Ti/Au, Trapping device mask	3.0 hour
3	Lift-off		1.0 hour
4	Nanowire deposition		2.0 hour
5	SEM / microscope inspection	Define the NW location	4.0 hour
6	Metal deposition	Ti, E-beam lithography	4.0 hour
7	Lift-off		2.0 hour
			Total: 17 hour

Wafer Clean (Start)				
Date/ Time	**1**	**Solvent Clean** ☐ Solvent Hood	Acetone/Methanol/IPA rinse Nitrogen dry	

METAL DEPOSITION (Start)				
Date/ Time	**2.1**	**Photolithography** **Image reverse** ☐ Hot plate ☐ Spinner check ☐ Spinner ☐ Hot plate (Soft bake) ☐ MJB-3 ☐ Hot plate (PEB) ☐ MJB3 (Flooded exposure) ☐ Base hood ☐ Profilometer ☐ Inspection Microscope	Set hot plate temperature @ 95°C wait for at least 1 hour to stabilize (Si Substrate heatsink) Recipe 5 5000 rpm ☐ AZ5214(target ~ 2um) ☐ 2.5 inch chuck w/ skirt ☐ Blue tape apply pressure w/ finger tweezers, 95°C/60 sec wipes underneath **Trapping Mask 2 (Up left quarter)** ☐ 2 inch chuck ☐ Mask orientation ☐ Determine exposure time PR Thickness: ____________um (Profilometer) Energy: ____________mJ/cm2 (Tk*25.6) Intensity: ____________mW/cm2 (From log) Exposure Time: ___________s (Energy/Intensity) **105 °C / 2 min 30 sec** ☐ No Mask Needed !! ☐ Determine exposure time Energy: ____________mJ/cm2 (Tk*67.2) Exposure Time: ____________s (Energy/Intensity) Develop 300 MIF (around **1min**) **Develop is temperature sensitive!!!** Temperature:__________ °C Volume:______________mL Develop time / Comments 1: _____**60s**_____,________________ 2: ______________,________________ 3: ______________,________________ 4: ______________,________________ 5: ______________,________________ 6: ______________,________________ Test Sample:___________________________(µm) Center Smallest Feature O.K.?	

	2.2	**Metal Deposition (Edwards)** ☐ Pumping down ☐ Ti deposition ☐ Au deposition	Pump down time:_____________ min Base pressure:________________ Torr Reference value **Ti : 100 Å @ 0.5-1 Å /sec** Start current:__________________mA Midway Deposition rate: ______________________ Å/sec Pressure______________________Torr End current___________________mA Thickness:______________________ Å Reference value **Au : 1000 Å @ 3.0-5 Å /sec** Start current:__________________mA Midway Deposition rate: ______________________ Å/sec Pressure______________________Torr End current___________________mA Thickness:______________________ Å	

LIFT-OFF (Start)				
Date/ Time	**3**	**Metal Liftoff** ☐ Solvent Hood ☐ Profilometer ☐ Quality gate	Acetone (Place in ultrasonic bath if necessary) Acetone / Methanol / IPA / DI rinse Thk A. Center Test Sample:_________________________(Å) Surface Cleanness ☐ Pass ☐ Fail Å < metal thickness < Å ☐ Pass ☐ Fail Hold, contact Engineering. Sign off: ________(Engr) ________ (Fab))	

Nanowire deposition				
	4	**Nanowire solution preparation** ☐ Hood ☐ Wet bench ☐ NW quantity in defined area	Origin size of a-Si growth sample: ___in. × ___in. Dilution, 1st (1:10), deposited NW OK? ____________ 2nd (1:10), deposited NW OK? ____________ 3rd (1:10), deposited NW OK? ____________ Define deposition area: _______um x ________um Deposition 0 < numbers <3 ☐ Pass ☐ Fail	0.1uL pipet with holder
	5.1	**SEM/ Microscope inspection**	The relative position of NW to: Image 1: full size including align markers Image 2: high magnification	
	5.2	**Pattern design**		

E-BEAM LITHOGRAPHY (START)				
Date/ Time	**6**	**Coating** ☐ Hot plate ☐ Spinner check ☐ Spinner ☐ Hot plate (Soft bake) ☐ marker	Set hot plate temperature @ 110°C wait for at least 1 hour to stabilize (Si Substrate heatsink) Recipe 5 5000 rpm ☐ 6% PMMA(target ~ 550nm) ☐ 2.5 inch chuck w/ skirt ☐ Blue tape apply pressure w/ finger tweezers, 110 °C / 60 sec wipes underneath ☐ Scratch on top left corner	
	6.1	**EBL run file design** ☐ NPGS	DesignCAD file creation Runfile creation Simulation	
	6.2	**Transportation**	☐ Non-transparent sample box	
	6.3	**E-beam operation** Check state Pump down	☐ X:20000um,Y:20000um,Z:30um,R:0 ☐ 10kV ☐ Angle:0 Field size: ________um Magnification:______ Beam current______pA Pattern name______ Exposure Time______	
	6.4	**Develop**	3:1 IPA:MIBK ☐ Time: 15s	

	6.5	**Check with microscope**	OK?______	
	6.6	**Metal Deposition (Edwards)** ☐ Pumping down ☐ Ti deposition	Pump down time:_____________ min Base pressure:_______________ Torr Reference value **Ti : 100 Å @ 0.5-1 Å /sec** Start current:_________________mA Midway Deposition rate: _____________________ Å/sec Pressure_____________________Torr End current__________________mA Thickness:______________________ Å	

LIFT-OFF (Start)				
Date/ Time	**7**	**Metal Liftoff** ☐ Solvent Hood ☐ Profilometer ☐ Quality gate	Acetone (Place in ultrasonic bath if necessary) Acetone / Methanol / IPA / DI rinse Thk A. Center Test Sample:_________________________(Å) Surface Cleanness ☐ Pass ☐ Fail Pattern OK? ☐ Pass ☐ Fail Hold, contact Engineering. Sign off: ________(Engr) ________ (Fab))	

Appendix K: Processing Traveler of Metallic Fishnet Integrated a-Si Solar Cell

Traveler, Schottky contact a-Si solar cell with 10nm thin Au contact

SKR1010
LOT0001

<table>
<tr><td rowspan="2">SKR1010</td><td colspan="3">UA ANBP Group
ENRC 2920, Phone:479-575-5231</td></tr>
<tr><td>DOCUMENT
NUMBER
00-0000-001</td><td>REVISION
A</td><td>PAGE
151 OF 194</td></tr>
<tr><td colspan="4">NFORMATION IS CONFIDENTIAL AND PROPRIETARY TO ASU MBE GROUP AND S
NOT BE REPRODUCED OR OTHERWISE DISCLOSED
TO ANYONE OTHER THAN ASU MBE GROUP MEMBERS WITHOUT WRITTEN
PERMISSION.</td></tr>
</table>

Fab Lot # SKR1010

Start Date: 10/21/2013
Due Date: 10/31/2013
Mask Set: Schottky contact solar cell mask
Purpose: Solar cell process of Schottky contact a-Si with 10nm thin Au contact.
Lot#: Solar cell, Schottky contact, RIE etching, 1(first attempt), 010(Round number)

Lot #	Wafer #	Growth #	Description
LOT0001	NA		1 inch x 1 inch glass substrate

OP/LINK	DESCRIPTION	PARAMETER	ESTIMATED TIME
1	Wafer Pre-clean		0.5 hour
2	Aluminum deposition	200nm thick	4 hours
3	PECVD a-Si deposition		3 hours
4	Photolithography	Schottky contact solar cell mask	2 hours
5	DRIE		2 hours
6	Photolithography	Schottky contact solar cell mask	2 hours
7	Top contact deposition	10nm gold	4 hours
8	Photolithography	Schottky contact solar cell mask	2 hours
9	E-beam align marker deposition	100nm gold	4 hours
10	E-beam lithography of fishnet structure		4 hours
11	Fishnet deposition		4 hours
			Total: 31.5 hours

Sample Preparation (<u>Start</u>)				
Date/ Time	**1.1**	**Substrate size** ☐ 1 inch × 1 inch glass substrate ☐ Four-point prober	Sample NO: ________________ ☐ Resistivity check	
	1.2	**Solvent Clean** (**Develop bench**)	☐ Acetone, Methanol, IPA, DI water, N_2 Blow dry	

Aluminum Deposition (<u>Start</u>)				
Date/ Time	**2**	**Metal Deposition (HiDEC 306D)** ☐ Pumping down ☐ Al deposition	Pump down:_____________ min Base pressure:_______________ mBar Reference value **<u>Al : 2000 Å @ 5 Å /sec</u>** Start current:_________________mA Start pressure________________mBar Start deposition rate:__________________ Å/sec End pressure_____________________mBar End current__________________mA End deposition rate:__________________ Å/sec Thickness:_____________________ Å	

Amorphous Silicon Deposition (<u>Start</u>)				
	3	**PECVD (ENRC 350B PECVD)** ☐ Pumping down ☐ a-Si deposition	Base pressure:_______________ mTorr Rate: 15nm/min (see parameter table below) Target thickness: _300_nm	

Temperature (℃)	Gas flow (sccm)	Pres. (mTorr)
250	SiH4 20	500
Power (W)	Time (mm:ss)	
2		

Photolithography (Start)

Date/ Time	4	**Photolithography**		
		☐ Eaton Hot plate	Set hot plate 1 at 95°C and hot plate 2 at 110°C for at least 10 minutes to stabilize	
		☐ Spinner check	☐ Vacuum OK? ☐ Recipe OK?	
		☐ Spinner	Recipe 4, 4000 rpm ☐ AZ 5214(target ~ 2um) ☐ 1.5 inch chuck ☐ Blue tape apply pressure w/ finger tweezers,	
		☐ Soft bake	95°C/60 sec	
		☐ MJB-3	☐ Schottky contact solar cell mask (mesa) PR Thickness: ______um (Profilometer) Intensity: _________mW/cm^2 (From log) Energy: ___________mJ/cm^2 (Tk*67.2) Exposure Time: _______s (Energy/Intensity)	
		☐ Develop bench	☐ MF-CD-26 **Develop is temperature sensitive!!!** Temperature: __25___°C Volume: _____________mL Develop time / Comments 1: ____60 sec_____,_______________ 2: _____________,_______________ 3: _____________,_______________ ☐ O.K.? PR thickness: __________________	
		☐ Postexposure bake	☐ 110 °C / 2 min 30 sec	

Reactive Ion etching (Start)

	5.1	**Dry etching**		
		☐ Plasma Thermal RIE	Recipe: LHSIETCH Processing pressure: ___300___mtorr Reference parameters Process parameters	

	Gas flow (sccm)		
	SF_6	O_2	C_4F_8
Etch	45	5	0
	Power(W)	Time(s)	
Etch	100		

Etch rate of a-Si: _____325 nm/min______
Etch rate of AZ5214: _____70 nm/min______
Etching thickness before resist removal: ________ µm

	5.2	**Resist removal** ☐ Solvent bench ☐ Develop bench ☐ LFE asher ☐ Microscope ☐ Dektek	Removal PG ☐ 70 degree ☐ 1 hour immersion Acetone ☐ 1 hour (room temperature) IPA / DI rinse ☐ 200 sccm O_2 ☐ 99 Watt ☐ 10 minutes Surface Cleanness ☐ Pass Etch depth after resist removal: _____________ μm	

Photolithography (Start)				
Date/ Time	**6**	**Photolithography** ☐ Eaton Hot plate ☐ Spinner check ☐ Spinner ☐ Soft bake ☐ MJB-3 ☐ Reversal bake ☐ MJB-3 ☐ Develop bench	Set hot plate 1 at 95°C and hot plate 2 at 105°C wait for at least 10 minutes to stabilize ☐ Vacuum OK? ☐ Recipe OK? Recipe 4, 4000 rpm ☐ AZ 5214(target ~ 2um) ☐ 1.5 inch chuck ☐ Blue tape apply pressure w/ finger tweezers, 95°C/60 sec ☐ Schottky contact solar cell mask (top contact) PR Thickness: ______um (Profilometer) Intensity: __________mW/cm^2 (From log) Energy: ___________mJ/cm^2 (Tk*25.6) Exposure Time: ___________s (Energy/Intensity) 105°C/2min30sec ☐ No mask needed!! ☐ Determine exposure time Energy: ___________mJ/cm^2 (Tk*67.2) Exposure Time: __________s (Energy/Intensity) ☐ MF-CD-26 **Develop is temperature sensitive!!!** Temperature: _________°C Volume: _____________mL Develop time / Comments 1: ____60 sec_____,_______________ 2: _____________,_______________ 3: _____________,_______________ ☐ O.K.?	

Top Contact Deposition (Start)				
Date/ Time	**7.1**	**Metal Deposition (Edwards thermal 306T)** □ Pumping down □ Au deposition	Pump down time:______________ min Base pressure:________________ mBar Reference value **Au : 100 Å @ 0.4 Å /sec** Start current: __________________mA Start pressure_________________ mBar Start deposition rate:___________________ Å/sec End pressure______________________ mBar End current ___________________mA End deposition rate:___________________ Å/sec Thickness:______________________ Å	
	7.2	**Metal Liftoff** □ Solvent bench □ Microscope	Remover PG □ 70 degree □ 1 hour immersion □ 5 minutes ultrasonic bath (room temperature) □ 1 hour immersion (70 degree) □ 5 minutes ultrasonic bath (room temperature) IPA / DI rinse Pattern OK? □ Pass □ Fail	

Photolithography (Start)				
Date/ Time	**8**	**Photolithography** ☐ Eaton Hot plate ☐ Spinner check ☐ Spinner ☐ Soft bake ☐ MJB-3 ☐ Reversal bake ☐ MJB-3 ☐ Develop bench	Set hot plate 1 at 95°C and hot plate 2 at 105°C wait for at least 10 minutes to stabilize ☐ Vacuum OK? ☐ Recipe OK? Recipe 4, 4000 rpm ☐ AZ 5214(target ~ 2um) ☐ 1.5 inch chuck ☐ Blue tape apply pressure w/ finger tweezers, 95°C/60 sec ☐ Schottky contact solar cell mask (align marker) PR Thickness: ______um (Profilometer) Intensity: __________mW/cm^2 (From log) Energy: ___________mJ/cm^2 (Tk*25.6) Exposure Time: ____5.5__s (Energy/Intensity) 105°C/2min30sec ☐ No mask needed!! ☐ Determine exposure time Energy: ___________mJ/cm^2 (Tk*67.2) Exposure Time: ____15___s (Energy/Intensity) ☐ MF-CD-26 **Develop is temperature sensitive!!!** Temperature: _________°C Volume: _____________mL Develop time / Comments 1: ____60 sec_____,_______________ 2: _____________,_______________ 3: _____________,_______________ ☐ O.K.?	

Align Marker Deposition (Start)				
Date/ Time	9.1	**Metal Deposition (Edwards thermal 306T)** ☐ Pumping down ☐ Cr deposition ☐ Au deposition	Pump down time:_____________ min Base pressure:________________ mBar Reference value **Cr : 100 Å @ 0.4 Å /sec** Start current: __________________mA Start pressure_________________ mBar Start deposition rate:___________________ Å/sec End pressure______________________ mBar End current ___________________mA End deposition rate:___________________ Å/sec Thickness:______________________ Å Reference value **Au : 1000 Å @ 0.4 Å /sec** Start current: __________________mA Start pressure_________________ mBar Start deposition rate:___________________ Å/sec End pressure______________________ mBar End current ___________________mA End deposition rate:___________________ Å/sec Thickness:______________________ Å	
	9.2	**Metal Liftoff** ☐ Solvent bench ☐ Microscope	Remover PG ☐ 70 degree ☐ 1 hour immersion ☐ 1 minute ultrasonic bath (room temperature) IPA / DI rinse Pattern OK? ☐ Pass ☐ Fail	

E-beam Lithography (Start)				
Date/ Time	10.1	☐ Hot plate ☐ Spinner check ☐ Spinner	Set hot plate temperature @ 180°C wait for at least 10 minutes to stabilize ☐ Vacuum OK? ☐ Recipe OK? Recipe _____, ________rpm ☐ Change the bowl dedicated for EBL ☐ Clean the lid ☐ PMMA vial Concentration: ☐ 2% ☐ 4% ☐ 6% ☐ 8% ☐ 1.5 inch chuck ☐ Blue tape apply pressure w/ finger tweezers, 180 °C / 120 sec	
	10.2	**Transportation**	☐ Non-transparent sample box	

	10.3	**E-beam exposure** ☐ System configuration	☐ 50 KV ☐ Mode 2 (four lens) ☐ Piece cassette ☐ Aperture 2	
		☐ Substrate	Sample center position (cassette coordinate): X: __________mm; Y: __________mm	
		☐ Exposure preparation	Calibration file: ________________ Current: ________nA ☐ Calibration OK? ☐ Alignment OK? Relative PQ marker position on mask X: ___3000__µm; Y: __0__µm PQ marker position after alignment Offset X: __________µm; Y: ___________µm Offset X: __________µm; Y: ___________µm	
		☐ Exposure	Pattern file name: _________________________ _________________________ _________________________ ☐ Piece cassette exposure configuration Scheduled file name: _________________________ **The piece cassette center is at (0, -5000 µm) in exposure configuration coordinate!!** Base dose: ___________ µC/cm^2 ☐ Shot rank (check sample information page) Writing time: ___________min ☐ Writing OK?	
	10.4	**Develop (E-beam room)**	3:1 IPA:MIBK ☐ Time: __________ Rinse with IPA ☐ Time: __________	
	10.5	**Check with microscope**	OK?______	

Fishnet Deposition (Start)				
Date/ Time	**11.1**	**Metal Deposition (Edwards thermal 306T)** ☐ Pumping down ☐ Cr deposition ☐ Au deposition	Pump down time:____________ min Base pressure:______________ mBar Reference value **Cr : 100 Å @ 0.4 Å /sec** Start current: ________________mA Start pressure_______________ mBar Start deposition rate:_________________ Å/sec End pressure____________________ mBar End current _________________mA End deposition rate:_________________ Å/sec Thickness:____________________ Å Reference value **Au : 300 Å @ 0.4 Å /sec** Start current: ________________mA Start pressure_______________ mBar Start deposition rate:_________________ Å/sec End pressure____________________ mBar End current _________________mA End deposition rate:_________________ Å/sec Thickness:____________________ Å	
	11.2	**Metal Liftoff** ☐ Solvent bench ☐ Microscope	Remover PG ☐ 70 degree ☐ 1 hour immersion ☐ 1 minute ultrasonic bath (room temperature) ☐ Overnight? IPA / DI rinse Pattern OK? ☐ Pass ☐ Fail	

<table>
<tr><td colspan="4">Sample NO:</td></tr>
<tr><td colspan="4">Resist information</td></tr>
<tr><td>Type:</td><td>Thickness:</td><td>Spin speed:</td><td>Base dose:</td></tr>
<tr><td colspan="4">Pattern information</td></tr>
<tr><td>Schedule file name:</td><td colspan="3">Total chip numbers (except marks):</td></tr>
<tr><td>Scheduled writing pattern</td><td>Chip NO</td><td colspan="2">Chip pattern name</td></tr>
<tr><td rowspan="8"></td><td></td><td colspan="2"></td></tr>
<tr><td>Description</td><td colspan="2"></td></tr>
<tr><td></td><td colspan="2"></td></tr>
<tr><td>Description</td><td colspan="2"></td></tr>
<tr><td></td><td colspan="2"></td></tr>
<tr><td>Description</td><td colspan="2"></td></tr>
<tr><td></td><td colspan="2"></td></tr>
<tr><td>Description</td><td colspan="2"></td></tr>
</table>

Chip number				
Scan step				
Shot rank				
Shot step				
Right dose after SEM				
Comments				
Chip number				
Scan step				
Shot rank				
Shot step				
Right dose after SEM				
Comments				

Job 1											
1	2	3	4	5	6	7	8	9	10	11	12
13	14	15	16	17	18	19	20	21	22	23	24
Job 2											
1	2	3	4	5	6	7	8	9	10	11	12
13	14	15	16	17	18	19	20	21	22	23	24
Job 3											
1	2	3	4	5	6	7	8	9	10	11	12
13	14	15	16	17	18	19	20	21	22	23	24
Job 4											
1	2	3	4	5	6	7	8	9	10	11	12
13	14	15	16	17	18	19	20	21	22	23	24
Job 5											
1	2	3	4	5	6	7	8	9	10	11	12
13	14	15	16	17	18	19	20	21	22	23	24
Job 6											
1	2	3	4	5	6	7	8	9	10	11	12
13	14	15	16	17	18	19	20	21	22	23	24
Job 7											
1	2	3	4	5	6	7	8	9	10	11	12
13	14	15	16	17	18	19	20	21	22	23	24
Job 8											
1	2	3	4	5	6	7	8	9	10	11	12
13	14	15	16	17	18	19	20	21	22	23	24

Appendix L: Processing Traveler of Metallic Nanostructures Integrated GeSn Photodetector

Traveler, Metallic nanostructure integrated GeSn photodetector

DVE1001
LOT0003

<table>
<tr><td rowspan="2">DVE1001</td><td colspan="3">UA ANBP Group
ENRC 2933, Phone:479-575-5231</td></tr>
<tr><td>DOCUMENT NUMBER
00-0000-000</td><td>REVISION
A</td><td>PAGE
163 OF
194</td></tr>
<tr><td colspan="4">FORMATION IS CONFIDENTIAL AND PROPRIETARY TO UARK SILICON PHOTONICS AND SHALL NOT BE REPRODUCED OR OTHERWISE DISCLOSED TO ANYONE OTHER THAN ASU MBE GROUP MEMBERS WITHOUT WRITTEN PERMISSION.</td></tr>
</table>

Fab Lot # DVE1001

Start Date: 11/12/2013
Due Date: 11/22/2013
Mask Set: 4in Mask PCPD0826_2
Purpose: Metallic nanostructures integrated GeSn/Ge photodetector
Lot#: Detector, For I-V measurement, E-beam lithography, 1(first attempt), 001(Round number)

Lot #	Wafer #	Growth #	Description
0002	0003-A51	ASM Epsilon Reactor, ASM Corp.	7 % Sn, 240 nm, Ge1-xSnx on Ge buffer, Si substrate

OP/LINK	DESCRIPTION	PARAMETER	ESTIMATED TIME
1	Sample Clean		1 hour
2	Mesa Etching		2.0 hours
3	Top Ohmic Contact Patterning		2.0 hours
4	Lift-off		2.0 hours
5	E-beam lithography		4.0 hours
6	Lift-off		2.0 hours - overnight
			Total: 13 hour - overnight

<table>
<tr><th colspan="5">Sample Pre-clean <u>(Start)</u></th></tr>
<tr><td>Date/
Time</td><td>1.1</td><td>Solvent Clean
☐ Sonicator</td><td>☐ Methanol sonication for 5 minutes
☐ Rinse with clean Methanol
☐ IPA sonication for 5 minutes
☐ Rinse with clean IPA
☐ N2 Dry /Dehydration bake, 95 ℃ for 5 minutes</td><td></td></tr>
</table>

<table>
<tr><th colspan="5">Mesa Etching <u>(Start)</u></th></tr>
<tr><td>Date/
Time</td><td>2.1</td><td>Photolithography
☐ Spinner check
☐ Spinner

☐ Hot plate (Soft bake)

☐ MJB-3

☐ Base hood

☐ Hot plate (Hard bake)

☐ Inspection Microscope
☐ Profilometer</td><td>Recipe 3; 3000 rpm
☐ AZ4110 (target ~ 1.75 um) ☐ Blue tape
☐ 2.5 inch chuck w/ skirt
☐ 95°C/60 sec
Check accuracy with thermocouple
PCPD0826_2 mask (Upper left quarter)
☐ Mask orientation
☐ Use middle corner on wafer stage!
☐ Determine exposure time
PR Thickness: ___________um (Profilometer)
Energy: ___________mJ/cm2 (Tk*45)
Intensity: ___________mW/cm2 (From log)
Exposure Time: _____10_____s (Energy/Intensity)
☐ Develop using 2.5% TMAH (around 60 sec)
☐ Rinse in DI water
☐ N2 Blow dry
Develop time / Comments
1: _____<u>60s</u>_____,________________

120 ℃/10 sec
Check accuracy with thermocouple
☐ Smallest Feature O.K.?

Resist Thickness: _______________ _____(μm)
Corners
Resist thickness: ________________ _____(μm)
Center</td><td></td></tr>
<tr><td></td><td>2.2</td><td>RIE

☐ Load Sample</td><td>Etch recipe name used: GeSn_ET
Expected etch rate: <u>50 nm/min</u>
<u>Etch Step:</u>
Gas Flow Rates (sccm)
Ar: <u>30</u> CF_4: <u>30</u>
O_2: <u>0</u> SF_6: <u>0</u></td><td></td></tr>
</table>

		☐ Run Etch Process	Pressure: 200 mtorr Power: 100 watts Time: 25:00 minutes	
	2.3	**Resist Removal** ☐ EBL hood ☐ Matrix Asher ☐ Inspection microscope ☐ Profilometer	☐ PG remover, 20 minutes at 80 ℃ **10 minute** run time Power: 150 Watts O_2 Gas Flow: 200 sccm ☐ OK Feature Height: ________________(µm) Corners Feature Height: ________________(µm) Center **Width** Expected:_________ Actual Width: ______ Expected:_________ Actual Width: ______	

Top Ohmic Contact Patterning (Start)				
Date/ Time	**3.1**	**Clean and prepare sample**	☐ 5 min sonication in IPA ☐ 5 min dehydration on hotplate at 95 °C	
	3.2	**Photolithography Image reverse** ☐ Spinner check ☐ Spinner ☐ Hot plate (Soft bake) ☐ MJB-3 ☐ Hot plate (PEB) ☐ MJB3 (Flooded exposure) ☐ Base hood ☐ Inspection Microscope	Recipe 4, 4000 rpm for 50 seconds ☐ AZ5214(target ~ 1.9 um) ☐ 2.5 inch chuck w/ skirt ☐ Blue tape 95°C/60 sec *Check accuracy with thermocouple* **PCPD0826_2 mask (Lower left quarter)** ☐ Mask orientation ☐ Use middle corner on wafer stage! ☐ Determine exposure time PR Thickness: ___________um (Profilometer) Energy: ___________mJ/cm2 (Tk*25.6) Intensity: ___________mW/cm2 (From log) Exposure Time: _____**6**_____s (Energy/Intensity) **105 °C / 2 min 30 sec** *Check accuracy with thermocouple* ☐ No Mask Needed ☐ Determine exposure time Energy: ___________mJ/cm2 (Tk*67.2) Exposure Time: _____**30**___s (Energy/Intensity) ☐ Develop 2.5 % TMAH (around **60 seconds**) ☐ Rinse in DI water ☐ N2 Blow dry Develop time / Comments 1: _____**60s**_____,_______________ 2: ______________,_______________ ☐ Smallest Feature O.K.?	

		☐ Profilometer	Resist Thickness: ______________________(µm) Corners Resist thickness: ______________________(µm) Center	
	3.3	**Metal Deposition (Edwards 306T)** ☐ Pumping down ☐ Cr deposition ☐ Au deposition	Pump down time:_____________ min Base pressure:_______________ Torr Reference value <u>Cr **: 100 Å @ 0.5-1 Å /sec**</u> Start current:_________________mA Midway Deposition rate: _____________________ Å/sec Pressure_____________________Torr End current__________________mA Thickness:_____________________ Å Reference value **<u>Au : 2000 Å @ 3.0-5 Å /sec</u>** Start current:_________________mA Midway Deposition rate: _____________________ Å/sec Pressure_____________________Torr End current__________________mA Thickness:_____________________ Å	
	3.4	**Inspect** ☐ Profilometer ☐ Inspection Microscope	Feature Height: ________________(µm) Corners Feature Height: ________________(µm) Center ☐ O.K.	

Lift-off <u>(Start)</u>				
Date/ Time	**4**	**Metal Lift-off** ☐ Solvent Hood ☐ Profilometer	Acetone (Place in ultrasonic bath if necessary) Acetone / Methanol / IPA / DI rinse Thk A. Center Feature height:_________________________(um) Surface Cleanness ☐ Pass ☐ Fail	

E-beam Lithography **(Start)**				
Date/ Time	**5.1**	☐ Hot plate ☐ Spinner check ☐ Spinner	Set hot plate temperature @ 180°C wait for at least 10 minutes to stabilize ☐ Vacuum OK? ☐ Recipe OK? Recipe _____, _______rpm ☐ Change the bowl dedicated for EBL ☐ Clean the lid ☐ PMMA vial Concentration: ☐ 2% ☐ 4% ☐ 6% ☐ 8% ☐ 1.5 inch chuck ☐ Blue tape apply pressure w/ finger tweezers, 180 °C / 120 sec	
	5.2	**Transportation**	☐ Non-transparent sample box	

	5.3	**E-beam exposure** ☐ System configuration ☐ Substrate ☐ Exposure preparation ☐ Exposure	☐ 50 KV ☐ Mode 2 (four lens) ☐ Piece cassette ☐ Aperture 2 Sample center position (cassette coordinate): X: __________mm; Y: __________mm Calibration file: ________________ Current: ________nA ☐ Calibration OK? ☐ Alignment OK? Relative PQ marker position on mask X: ___4400__μm; Y: __0__μm PQ marker position under microscope X: ____________μm; Y: _____________μm X: ____________μm; Y: _____________μm PQ marker position after alignment Offset X: __________μm; Y: ___________μm Offset X: __________μm; Y: ___________μm Pattern file name: _________________________ _________________________ _________________________ ☐ Piece cassette exposure configuration Scheduled file name: _________________________ **The piece cassette center is at (0, -5000 μm) in exposure configuration coordinate!!** Base dose: ___________ $\mu C/cm^2$ ☐ Shot rank (check sample information page) Writing time: ___________min ☐ Writing OK?	
	5.4	**Develop (E-beam room)**	3:1 IPA:MIBK ☐ Time: __________ Rinse with IPA ☐ Time: __________	
	5.5	**Check with microscope**	OK?______	

	5.6	**Metal Deposition (Edwards 306D)** ☐ Pumping down ☐ Cr deposition ☐ Au deposition	☐ Pre-evaporation of 30 nm Cr Pump down time:_____________ min Base pressure:_______________ mBar Reference value **<u>Cr : 100 Å @ 0.2 Å /sec</u>** Start current:_________________mA (in scale) Start pressure________________mBar Start deposition rate:__________________ Å/sec End pressure_____________________mBar End deposition rate:__________________ Å/sec Thickness:_____________________ Å Reference value **<u>Au : 600 Å @ 1 Å /sec</u>** Start current:_________________mA (in scale) Start pressure________________mBar Start deposition rate:__________________ Å/sec Start Temperature:________________ End current:_________________mA (in scale) End pressure_____________________mBar End deposition rate:__________________ Å/sec **End Temperature**:________________ Thickness:_____________________ Å	

Lift-off <u>(Start)</u>				
Date/ Time	**6**	**Metal Liftoff** ☐ Solvent Hood ☐ Microscope	PMMA sample Remover PG (Place in ultrasonic bath if necessary) Temperature: Time: Acetone / Methanol / IPA / DI rinse Surface Cleanness ☐ Pass ☐ Fail Pattern OK? ☐ Pass ☐ Fail	

<table>
<tr><td colspan="4">Sample NO:</td></tr>
<tr><td colspan="4">Resist information</td></tr>
<tr><td>Type:</td><td>Thickness:</td><td>Spin speed:</td><td>Base dose:</td></tr>
<tr><td colspan="4">Pattern information</td></tr>
<tr><td>Schedule file name:</td><td colspan="3">Total chip numbers (except marks):</td></tr>
<tr><td>Scheduled writing pattern</td><td>Chip NO</td><td colspan="2">Chip pattern name</td></tr>
<tr><td rowspan="8"></td><td></td><td colspan="2"></td></tr>
<tr><td>Description</td><td colspan="2"></td></tr>
<tr><td></td><td colspan="2"></td></tr>
<tr><td>Description</td><td colspan="2"></td></tr>
<tr><td></td><td colspan="2"></td></tr>
<tr><td>Description</td><td colspan="2"></td></tr>
<tr><td></td><td colspan="2"></td></tr>
<tr><td>Description</td><td colspan="2"></td></tr>
</table>

Chip number				
Scan step				
Shot rank				
Shot step				
Right dose after SEM				
Comments				
Chip number				
Scan step				
Shot rank				
Shot step				
Right dose after SEM				
Comments				

Job 1											
1	2	3	4	5	6	7	8	9	10	11	12
13	14	15	16	17	18	19	20	21	22	23	24
Job 2											
1	2	3	4	5	6	7	8	9	10	11	12
13	14	15	16	17	18	19	20	21	22	23	24
Job 3											
1	2	3	4	5	6	7	8	9	10	11	12
13	14	15	16	17	18	19	20	21	22	23	24
Job 4											
1	2	3	4	5	6	7	8	9	10	11	12
13	14	15	16	17	18	19	20	21	22	23	24
Job 5											
1	2	3	4	5	6	7	8	9	10	11	12
13	14	15	16	17	18	19	20	21	22	23	24
Job 6											
1	2	3	4	5	6	7	8	9	10	11	12
13	14	15	16	17	18	19	20	21	22	23	24
Job 7											
1	2	3	4	5	6	7	8	9	10	11	12
13	14	15	16	17	18	19	20	21	22	23	24
Job 8											
1	2	3	4	5	6	7	8	9	10	11	12
13	14	15	16	17	18	19	20	21	22	23	24

Appendix M: Permission to Reuse Copyrighted Materials

RightsLink®

Home | Create Account | Help

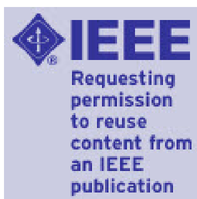

Title: Amorphous silicon solar cells using metallic fishnet nanostructures simultaneously for Schottky contact and plasmonics enhancement

Conference Proceedings: Photovoltaic Specialists Conference (PVSC), 2013 IEEE 39th

Author: Liang Huang; Huixu Deng; Thach Pham; Young, M.; Naseem, H.; Abu-Safe, H.H.; Xiaodong Yang; Shui-Qing Yu

Publisher: IEEE

Date: 16-21 June 2013

Copyright © 2013, IEEE

User ID

Password

Enable Auto Login

LOGIN

Forgot Password/User ID?

If you're a copyright.com user, you can login to RightsLink using your copyright.com credentials. Already a **RightsLink user** or want to learn more?

Thesis / Dissertation Reuse

The IEEE does not require individuals working on a thesis to obtain a formal reuse license, however, you may print out this statement to be used as a permission grant:

Requirements to be followed when using any portion (e.g., figure, graph, table, or textual material) of an IEEE copyrighted paper in a thesis:

1) In the case of textual material (e.g., using short quotes or referring to the work within these papers) users must give full credit to the original source (author, paper, publication) followed by the IEEE copyright line © 2011 IEEE.
2) In the case of illustrations or tabular material, we require that the copyright line © [Year of original publication] IEEE appear prominently with each reprinted figure and/or table.
3) If a substantial portion of the original paper is to be used, and if you are not the senior author, also obtain the senior author's approval.

Requirements to be followed when using an entire IEEE copyrighted paper in a thesis:

1) The following IEEE copyright/ credit notice should be placed prominently in the references: © [year of original publication] IEEE. Reprinted, with permission, from [author names, paper title, IEEE publication title, and month/year of publication]
2) Only the accepted version of an IEEE copyrighted paper can be used when posting the paper or your thesis on-line.
3) In placing the thesis on the author's university website, please display the following message in a prominent place on the website: In reference to IEEE copyrighted material which is used with permission in this thesis, the IEEE does not endorse any of [university/educational entity's name goes here]'s products or services. Internal or personal use of this material is permitted. If interested in reprinting/republishing IEEE copyrighted material for advertising or promotional purposes or for creating new collective works for resale or redistribution, please go to http://www.ieee.org/publications_standards/publications/rights/rights_link.html to learn how to obtain a License from RightsLink.

If applicable, University Microfilms and/or ProQuest Library, or the Archives of Canada may supply single copies of the dissertation.

BACK | CLOSE WINDOW

Copyright © 2014 Copyright Clearance Center, Inc. All Rights Reserved. Privacy statement.
Comments? We would like to hear from you. E-mail us at customercare@copyright.com